PRODUCTION AND CHARACTERIZATION OF ALUMINUM-RARE EARTH BASED BULK AMORPHOUS/NANOCRYSTALLINE COMPOSITE

A THESIS SUBMITTED TO
THE GRADUATE SCHOOL OF NATURAL AND APPLIED SCIENCES
OF
MIDDLE EAST TECHNICAL UNIVERSITY

BY

MUSTAFACAN KUTSAL

IN PARTIAL FULFILLMENT OF THE REQUIREMENTS
FOR
THE DEGREE OF MASTER OF SCIENCE
IN
METALLURGICAL AND MATERIALS ENGINEERING

JUNE 2016

Approval of the thesis:

PRODUCTION AND CHARACTERIZATION OF ALUMINUM-RARE EARTH BASED BULK AMORPHOUS/NANOCRYSTALLINE COMPOSITE

submitted by **MUSTAFACAN KUTSAL** in partial fulfillment of the requirements for the degree of **Master of Science in Metallurgical and Materials Engineering Department, Middle East Technical University** by,

Prof. Dr. Gülbin Dural Ünver _____
Dean, Graduate School of **Natural and Applied Sciences**

Prof. Dr. C. Hakan Gür _____
Head of Department, **Metallurgical and Materials Engineering**

Assoc. Prof. Dr. Y. Eren Kalay _____
Supervisor, **Metallurgical and Materials Eng. Dept., METU**

Examining Committee Members:

Prof. Dr. Hamdullah Mekhrabov _____
Metallurgical and Materials Engineering Dept., METU

Assoc. Prof. Dr. Y. Eren Kalay _____
Metallurgical and Materials Engineering Dept., METU

Assist. Prof. Dr. Caner Şimşir _____
Manufacturing Engineering Dept., Atılım University

Assist. Prof. Dr. Batur Ercan _____
Metallurgical and Materials Engineering Dept., METU

Assist. Prof. Dr. Sezer Özerinç _____
Mechanical Eng. Dept., METU

Date: 27.06.2016

I hereby declare that all information in this document has been obtained and presented in accordance with academic rules and ethical conduct. I also declare that, as required by these rules and conduct, I have fully cited and referenced all material and results that are not original to this work.

Name, Last name: Mustafacan Kutsal

Signature :

ABSTRACT

PRODUCTION AND CHARACTERIZATION OF ALUMINUM-RARE EARTH BASED BULK AMORPHOUS/NANOCRYSTALLINE COMPOSITE

Kutsal, Mustafacan

M.S., Department of Metallurgical and Materials Engineering

Supervisor: Assoc. Prof. Dr. Y. Eren Kalay

June 2016, 148 pages

The structure, production and consolidation of binary Al-RE (RE=Sm, Tb) and multicomponent Al-RE-TM (TM= Fe, Ni, Cu) metallic glasses were studied mainly in two parts. In the first part, solid-state amorphous structures of melt-spun and magnetron sputtered thin films of $Al_{90}Tb_{10}$ were investigated with high energy X-ray diffraction (HEXRD) constrained reverse Monte Carlo (RMC) simulations. The experimental findings and calculated models had shown that amorphous alloys having the same composition comprises the same atomic arrangement in short-range order (SRO) scale, yet have distinctly differing structures in medium-range (MRO) scale. In the second part of the study, amorphization of Al-RE and Al-RE-TM based alloys with mechanical milling and alloying were studied. It was found that binary and quaternary

compositions of Al-RE systems had strong resistance against vitrification through mechanical milling. However, partial amorphization in Al-RE-TM and Al-RE-TM1-TM2 systems were achieved with mechanical alloying. Characterization of mechanically alloyed $Al_{85}Sm_7Fe_5Ni_3$ powders had revealed the structure is not fully disordered but comprise an amorphous/nanocrystalline structure, consisting of amorphous phase, fcc-Al nanocrystals and unknown intermetallic phase with spherical morphology. Consolidation of mechanically alloyed $Al_{85}Sm_7Fe_5Ni_3$ powders were studied with pressing and sintering, and warm pressing. The effect of ex-situ composite formation with the mechanically alloyed powders mixed with pure Al powders on mechanical properties of the bulk structures were also investigated. Mechanical characterization of the bulk amorphous/nanocrystalline and ex-situ composite consolidates were performed, together with their post-mortem failure analyses.

Keywords: Medium-range order, short-range order, reverse Monte Carlo modelling, marginal metallic glasses, mechanical milling and alloying, consolidation

ÖZ

ALÜMİNYUM-NADİR TOPRAK ELEMENTİ AMORF/NANOKRİSTAL HACİMLİ KOMPOZİTLERİN ÜRETİMİ VE KARAKTERİZASYONU

Kutsal, Mustafacan

Yüksel Lisans, Metalurji ve Malzeme Mühendisliği Bölümü

Tez Yöneticisi: Doç. Dr. Y. Eren Kalay

Haziran 2016, 148 sayfa

İkili Al-NTE (NTE =Sm, Tb) ve çok bileşenli Al-NTE- GM (Geçiş Metali= Fe, Ni, Cu) metalik camlarının yapısı, üretimi ve sıkılaştırılması iki ayrı bölümde incelenmiştir. Birinci kısımda eriyik savurma ve manyeton saçılma ile üretilen $Al_{90}Tb_{10}$ metalik cam alaşımlarının yapısı yüksek enerjili X-ışını kırınımı (HEXRD) ile sınırlandırılmış tersine Monte Carlo hesaplamaları ile incelenmiştir. Deneysel bulgular ve yapılan hesaplamalar aynı kompozisyona sahip iki alaşımdaki atomik düzenlemelerin kısa erim düzeninde (SRO) aynı olduğu; fakat orta erim düzeninde farklı olduğunu göstermiştir. Çalışmanın ikinci bölümünde Al-NTE ve Al-NTE-GM alaşımlarının mekanik öğütme ve alaşımlama ile amorf halde eldesi çalışılmıştır. Yapılan çalışmalarda ikili Al-NTE ve dörtlü Al-NTE-GM alaşım sistemlerinin mekanik öğütme ile amorf eldesine karşı yüksek direnç sahibi olduğu gözlenmiştir. Fakat mekanik alaşımlama ile üretilen Al-NTE-GM ve Al- NTE-GM1-GM2 alaşımlarında kısmi miktarda amorf faz elde edilmiştir. Üretimden sonra karakterize

edilen mekanik alaşımlanmış $Al_{85}Sm_7Fe_5Ni_3$ alaşımının amorf/nanokristal yapıda olduğu ve içinde amorf faz, nanokristal fcc-Al ve küresel halde bilinmeyen intermetalik fazı belirlenmiştir. Mekanik alaşımlanmış $Al_{85}Sm_7Fe_5Ni_3$ amorf/nanokristal alaşımının sıkılaştırılarak hacimli yapıların oluşturulması basma ve sinterleme, ve sıcak basma ile gerçekleştirilmiştir. Ayrıca belirtilen alaşıma saf Al tozu eklenerek ex-situ kompozit oluşumunun hacimli yapılar oluşturulmuş ve amorf/nanokristal alaşımın mekanik özelliklerine etkisi incelenmiştir. Üretilen hacimli yapıların mekanik özellikleri, post-mortem kırılma yüzeyi incelemeleri ile birlikte verilmiştir.

Anahtar Kelimeler: Orta erim düzeni, kısa erim düzeni, tersine Monte Carlo modellemesi, marjinal metalik camlar, mekanik öğütme ve alaşımlama, sıkılaştırma

To My Late Grandparents,

Hacer & Mustafa Kutsal…

ACKNOWLEDGEMENTS

The work at METU was financially supported by the Scientific and Technological Research Council of Turkey (TUBITAK) under Grant No. 113M346. The total scattering and high-energy *in situ* X-ray experiments were performed at the BL04 - MSPD beamline of the ALBA Synchrotron Facility, and financially supported by CALIPSO program. Inmaculada Peral and Oriol Vallcorba are acknowledged for their valuable help in the experiments in ALBA. Dr. Matthew Kramer is also acknowledged for specimen preparation.

Firstly, I would like to express my gratitude to my advisor Assoc. Prof. Dr. Y. Eren Kalay for his guidance and sincere support throughout the study. I feel lucky for being the first undergraduate student to knock his door. Stepping through his office door had changed my life in lots of different aspects, both as a scientist and humane-wise.

Secondly, I would like to thank my former and current lab-mates Can Yıldırım, Mertcan Başkan, Ayşe Merve Ünalan, Serkan Yılmaz, Tuba Demirtaş, Mert Övün, Anıl Kantarcıoğlu, Özgün Acar, Fatih Sıkan, Bengisu Yaşar, Burcu Çam, Tolga Han Ulucan, Baran Tunç, Eyüp Can Demir and Ayşe Duman. They all will be remembered for their intimate companionship and countless liters of coffee drinking. Also, special thanks to Güher Tan for her kindheartedness and utmost support to help me keep up with the ups and downs of my life.

I would like to thank my good friends, the "nightcrew" of the department, Mehmet Hazar Şeren, Lütfi Ağartan, Şafak Doğu and Ekim Saraç for the hours of funny chatter and also for solidarity in the cold dark –yet joyful nights. Those endless nights will be remembered as the high-times of my life. Sena Okay, Zeynep Öztürk, Gülten Kılıç, Mehmet Dinçer and Bıdık the Cat are also acknowledged for taking me as their extra lab-mate.

I would also want to express my gratitude for my-lifelong friends: Barış Pekçağlıyan, Sinan Cem Kızıl, Anıl Üner, Çağatay Karakan, Faruk Sevgili, Onur Koşar, Gökhan İpekkan, Rasim Hüseyin Baloğlu, Sonat Özcivanoğlu, Erkan Uslu. These people have the greatest share in provoking me to think out of the box, for each and every aspect of the universe and the life itself. For that reason, I am and always will be in debt to show my deepest gratitude. Last but not least, I am also thankful for Ekin Demirci and Gülce Kale for their sincere and deep conversations, Dicle Kumaraslan, Caner Arıkboğa, Ömer Sarı and Chipotle the Cat for their kind and thought-provoking love and friendship. I would also thank Rebecca and Bill Goldsmith of Radio Paradise for keeping me company throughout the experiments (and times in front of the computer) with their fantastic choice of music.

I would like to appreciate all the efforts, support and willing of my dear mother and father, whom have suffered the same stress and fatigue that I have suffered through the whole of my life. For that reason, I probably would not be able to pay my emotional and material debt for the rest of my life.

All at last, I would like to dedicate this work to the people who raised me as a child, and whom had the biggest share in the way that I become who I am, to Hacer and Mustafa Kutsal. If I had not been raised without their emotional and mental education, I wouldn't probably have the tools to deal with all the tsunamis of the life, yet hadn't enjoy the sunshine. Because of this, I would like to dedicate this work in their memory. May their souls rest in peace, in the way it should be.

TABLE OF CONTENTS

ABSTRACT ..... **V**

ÖZ ..... **VII**

ACKNOWLEDGEMENTS ..... **X**

TABLE OF CONTENTS ..... **XII**

LIST OF TABLES ..... **XV**

LIST OF FIGURES ..... **XVI**

NOMENCLATURE ..... **XXII**

CHAPTERS

1. INTRODUCTION **1**

1.1. A Brief History of Metallic Glass Research **2**

1.2. Glass Formation and Production Routes of Metallic Glasses **5**

1.2.1 Glass Production 6

1.2.2 Glass Forming Ability 9

1.2.3 Rapid Solidification Techniques 12

1.2.3.1. Melt-Spinning Technique 13

1.2.3.2. Magnetron Sputtering 13

1.2.4 Glass Formation Through Mechanical Milling and Alloying 15

1.2.4.1. Mechanical Milling 16

1.2.4.2. Mechanical Alloying 18

1.3. Structural and Dynamical Characterization of Metallic Glasses 20

1.3.1 Differential Scanning Calorimetry 20

1.3.2 Transmission Electron Microscopy 22

1.3.3 Fluctuation Microscopy 25

1.3.4 Synchrotron Light Source 27

1.3.4.1. Total Structure Factor 31

1.3.4.2. Pair Distribution Function 32

1.3.4.3. Effect of Experimental Parameters on Pair Distribution Function Calculation 35

1.3.5 Reverse Monte Carlo Method 37

1.3.6 Conclusion and Thesis Organization 41

2. SHORT-TO-MEDIUM-RANGE CORRELATIONS IN 43

AL-RE METALLIC GLASSES 43

2.1 Abstract 43

2.2 Introduction 43

2.3 Experimental Procedure 47

2.4 Results and Discussion 49

2.5 Conclusion 63

2.6 Acknowledgement 63

3. AL-RE-BASED AMORPHOUS/NANOCRYSTALLINE COMPOSITE POWDER PRODUCTION AND CONSOLIDATION 65

3.1 Abstract 65

3.2 Introduction 66

3.3 Experimental Procedure 68

3.4 Results and Discussion 73

3.4.1 Amorphous/Nanocrystal Powder Synthesis 73

3.4.1.1 Mechanical Milling 73
3.4.1.2 Mechanical Alloying 79
3.4.2 Consolidation with How Pressing and Sintering 93
3.4.3 Consolidation with Warm Pressing 101
3.5 Conclusion 115
3.6 Acknowledgments 116

4. CONCLUSION AND FUTURE RECOMMENDATIONS 117
4.1 Conclusion 117
4.2 Future Recommendations 118

REFERENCES 125

LIST OF TABLES

Table 2.1: Comparison of average bond orientation angles of as-spun and as-sputtered $Al_{90}Tb_{10}$ from simulated RMC models 53
Table 2.2: Comparison of local average coordination numbers of as-spun and as-sputtered $Al_{90}Tb_{10}$ from simulated RMC models and ECP model 57

Table 3.1: Literature review of mechanically alloyed Al-based metallic glasses 67
Table 3.2: Calculated activation energies for $Al_{88}Sm_7Fe_5Ni_3$ amorphous/nanocrystal composite with Kissinger and Ozawa approaches. 85
Table 3.3: Activation energies of Al-RE and Al-RE-TM alloys determined using Kissinger and Ozawa methods. 86
Table 3.4: Measured hardness values of warm pressed consolidates. 111

LIST OF FIGURES

Figure 1.1: Viscosity vs. temperature plot for crystal and glass formation. Adopted from [36]. 7

Figure 1.2: Variation of **(a)** specific volume and **(b)** specific heat [36] with temperature. 8

Figure 1.3: Schematic phase diagram of a hypothetical alloy under **(a)** equilibrium and **(b)** non-equilibrium processing conditions. The conditions of the intersecting and non-intersecting T_0 lines are given in **(c)** and **(d)**, respectively. Retrieved from [39]. 10

Figure 1.4: (a) A sketch of TTT diagram for a metallic glass. **(b)** Measured TTT diagram of Vitreloy 1®[42]. **(c)** Calculated TTT diagrams of pure Ni, and AuGeSi, PdSi and PdCuSi alloys[36]. 11

Figure 1.5: (a) Cu-block melt spinning device used in this study [Retrieved from 46]. **(b)** Schematic representation of a melt spinner [Retrieved from 36]. **(c)** Close-up schematic of solidification process on Cu-block [Retrieved from 47]. 13

Figure 1.6: (a) Schematic representation of magnetron sputtering and **(b)** magnetron sputtering device [Retrieved from **52** and **53**, respectively]. 14

Figure 1.7: Schematic representation of a collision in mechanical milling and alloying [Retrieved from **54**]. 16

Figure 1.8: Analogical phase diagram of temperature or exerted mechanical energy versus composition [Retrieved from 57]. 17

Figure 1.9: Phase evolution of mechanically alloyed $Al_{65}Cu_{20}Ti_{15}$ alloy through XRD patterns[**59**]. 19

Figure 1.10: Typical DSC thermogram of a metallic glass alloy [Adapted from **60**].21

Figure 1.11: Bright field image and selected area diffraction pattern of an as-spun $Al_{90}Tb_{10}$ metallic glass alloy [Courtesy of T. Demirtaş]. 23

Figure 1.12: (a) HRTEM images of phase separated $Al_{90}Sm_{10}$ metallic glass. Inset shows the SAED pattern of the same region. (b) HAADF imaging of the phase separated regions of the same alloy [Courtesy of M.J. Kramer and R.T. Ott]..... 23
Figure 1.13: HRTEM micrograph of as-spun $Al_{90}Y_{10}$ metallic glass (a), and FFT patterns of selected regions in (b) and (c), respectively..... 25
Figure 1.14: (a) Sketch of speckle pattern formation through random and coherent domains of a sample. **(b)** Representation of FEM techniques; microdiffraction and hollow-cone dark field [Retrieved from [68]]..... 26
Figure 1.15: Schematic representation of European Synchrotron Radiation Facility in Grenoble, France [Image retrieved from [74]]..... 27
Figure 1.16: (a) Photograph of a bending magnet. The colored guides show the trajectories of the electron bunch (in blue) and the radiated light (in red)[76]. **(b)** A canted undulator that is being used in Advance Photon Source, USA[78]..... 29
Figure 1.17: Brilliance comparison of some of the modern X-ray generators[79]..... 30
Figure 1.18: (a) Raw total scattering experiment data and **(b)** corresponding calculated structure factor of melt-spun $Al_{90}Y_{10}$ metallic glass..... 32
Figure 1.19: Pair distribution functions derived from total scattering experiments of **(a)** pure crystalline metallic Platinum[[88]] and **(b)** melt-spun amorphous $Al_{90}Y_{10}$ metallic glass..... 34
Figure 1.20: (a) Total X-ray structure factors and **(b)** correspondingly derived PDFs of melt-spun $Al_{90}Tb_{10}$ metallic glass with data collected with Alba and Elettra synchrotron lightsources, and a conventional diffractometer..... 36
Figure 1.21: Schematic representation of discretization of space for partial PDF calculation[101]..... 39
Figure 1.22: Schematic representation regular and distorted icosahedral clusters and their respective Voronoi indices that are present in CuZr metallic glasses[67]..... 40
Figure 1.23: Elastic limit versus elastic modulus assessment plot for metals and alloys. Black and grey contours show the yield strain and resilience, respectively[102]..... 41

Figure 2.1: Experimentally measured (open circles) and RMC fitted (solid line) total structure factors of melt-spun ribbons and magnetron sputtered thin films of $Al_{90}Tb_{10}$. 50
Figure 2.2: (a) Experimental pair distribution functions (PDF) derived from HEXRD for as-spun and as-sputtered $Al_{90}Tb_{10}$. **(b-d)** Partial PDFs of Al-Al, Al-Tb and Tb-Tb of as-spun and as-sputtered $Al_{90}Tb_{10}$ calculated from simulated RMC models. 51
Figure 2.3: The distribution of bond-orientation angles for as-quenched and as-sputtered $Al_{90}Tb_{10}$ alloys calculated from simulated RMC models. 52
Figure 2.4: Comparison of frequent Voronoi Polyhedra, calculated for both melt-spun ribbon and sputtered thin film with respect to (a) Al-centered and (b) Tb-centered clusters. 54
Figure 2.5: Coordination numbers calculated for (a) Al and (b) Tb centered from Voronoi Tessellation of as-quenched and as-sputtered $Al_{90}Tb_{10}$. 56
Figure 2.6: Fluctuation Electron Microscopy patterns obtained for as-spun and as-sputtered $Al_{90}Tb_{10}$ metallic glasses [Courtesy of P.M. Voyles]. 59

Figure 3.1: (a) Hardened ball and vial set and **(b)** SPEX 8000M high energy shaker mill used for mechanical milling and alloying experiments. 69
Figure 3.2: (a) A 15mm diameter die used for pressing experiments. **(b)-(c)** The hydraulic presses used for the experiments having 30 and 300 tons of maximum loads, respectively. 71
Figure 3.3: XRD patterns of as-atomized $Al_{90}Sm_{10}$ powders with mean particle sizes of 45 and 75 micrometers. 73
Figure 3.4: Backscatter electron images of as-atomized $Al_{90}Sm_{10}$ powders with mean particle sizes of **(a)** 45 and **(b)** 75 micrometers. 74
Figure 3.5: Phase evolution during mechanical milling of 45 μm-sized gas atomized $Al_{90}Sm_{10}$ powders. 74
Figure 3.6: EDS spectrum of 45 μm-sized gas atomized $Al_{90}Sm_{10}$ powders, mechanically milled for 140 hours. 75

Figure 3.7: XRD patterns of gas atomized 75 μm-sized $Al_{90}Sm_{10}$ powders after mechanical milling for 10 (black line) and 90 hours (red line)..... 76
Figure 3.8: SEM image of gas atomized 75 μm-sized $Al_{90}Sm_{10}$ powders after mechanical milling for 90 hours. 76
Figure 3.9: Backscattered electron micrographs of as-suction casted $Al_{85}Sm_7Fe_5Cu_3$ alloy. 78
Figure 3.10: XRD pattern of suction casted $Al_{85}Sm_7Fe_5Cu_3$ alloy, after 150 hours of milling. 78
Figure 3.11: Microstructure of mechanically alloyed $Al_{88}Sm_7Ni_5$ alloy milled for 55 hours, revealed via XRD pattern. 80
Figure 3.12: Microstructure of mechanically alloyed $Al_{88}Sm_7Fe_5Ni_3$ alloy milled for 60 hours, revealed via XRD pattern. 81
Figure 3.13: BF images and SADP of mechanically alloyed $Al_{88}Sm_7Fe_5Ni_3$ alloy milled for 60 hours. 81
Figure 3.14: DSC traces of **(a)** mechanically alloyed $Al_{88}Sm_7Fe_5Ni_3$ alloy milled for 60 hours, and **(b)** $Al_{90}Y_{10}$ melt-spun ribbon, under isochronal constant heating rate conditions. 83
Figure 3.15: DSC traces of mechanically alloyed $Al_{88}Sm_7Fe_5Ni_3$ alloy milled for 60 hours under isochronal constant heating with varying rates. 84
Figure 3.16: (a) Kissinger and **(b)** Ozawa plots for activation energy determination. 86
Figure 3. 17: 2D surface plot of *in situ* heating HEXRD results of 60 hours mechanically milled $Al_{88}Sm_7Fe_5Ni_3$ amorphous/nanocrystalline powder. 88
Figure 3.18: (a) Particle size distribution obtained from the particle size analyzer. **(b)** A close-up SEM image from a large as-milled $Al_{88}Sm_7Fe_5Ni_3$ amorphous/ nanocrystalline powder. 89
Figure 3.19: SEM images of **(a)** agglomerated and **(b)** small sized as-milled $Al_{88}Sm_7Fe_5Ni_3$ amorphous/nanocrystalline powders. 91

Figure 3.20: (a) Cross sectional and **(b)** close up view of as-milled $Al_{88}Sm_7Fe_5Ni_3$ amorphous/nanocrystalline powders. 92
Figure 3.21: SEM images of green compacts produced with applied loads of **(a)** 22 tons and **(b)** 50 tons. 93
Figure 3.22: Isochronal DSC scans of $Al_{88}Sm_7Fe_5Ni_3$ amorphous/nanocrystalline alloy in as-milled and as-pressed conditions. 95
Figure 3.23: Isothermal DSC holds of produced green compacts under applied loads of 22 and 50 tons. 96
Figure 3.24: Surface images of $Al_{88}Sm_7Fe_5Ni_3$ amorphous/nanocrystalline samples produced with 50 tons of applied load, sintered at 573 K for **(a-b)** 60 minutes and **(c-d)** 90 minutes. Arrows indicate porosities. 98
Figure 3.25: Surface images of $Al_{88}Sm_7Fe_5Ni_3$ amorphous/nanocrystalline compacts in the **(a)** as-pressed and **(b)** as-sintered state. 97
Figure 3.26: Compression test result of $Al_{88}Sm_7Fe_5Ni_3$ amorphous/nanocrystalline sintered compact, prepared according to ASTM E-9 standard. 99
Figure 3.27: (a) Lateral view and **(b)** fracture surface of $Al_{88}Sm_7Fe_5Ni_3$ amorphous/nanocrystalline sintered compact, prepared according to ASTM E-9 standard. 100
Figure 3.28: Comparative compression test result of $Al_{88}Sm_7Fe_5Ni_3$ amorphous/nanocrystalline of cut and large samples. 101
Figure 3.29: An ex-situ composite sample, produced with warm pressing. 102
Figure 3.30: XRD pattern of the warm press consolidated $Al_{88}Sm_7Fe_5Ni_3$ amorphous/nanocrystalline alloy 103
Figure 3.31: Isochronal DSC trace of the warm press consolidated $Al_{88}Sm_7Fe_5Ni_3$ amorphous/nanocrystalline alloy 104
Figure 3.32: Compression test result of the warm press consolidated $Al_{88}Sm_7Fe_5Ni_3$ amorphous/nanocrystalline alloy 105
Figure 3.33: SEM images of **(a)** crack propagation and **(b)** shear bands on the grains in the compression test sample of the warm press consolidated $Al_{88}Sm_7Fe_5Ni_3$

amorphous/nanocrystalline alloy. Arrows in Figure **(b)** indicates the shear bands on a grain..... 106
Figure 3.34: XRD pattern of warm pressed $Al_{88}Sm_7Fe_5Ni_3$ amorphous/nanocrystalline with 30% pure Al added consolidate. 107
Figure 3.35: Compression test result of the warm pressed $Al_{88}Sm_7Fe_5Ni_3$ amorphous/nanocrystalline with 30% pure Al added consolidate. 108
Figure 3.36: SEM images taken from the surface of the warm pressed $Al_{88}Sm_7Fe_5Ni_3$ amorphous/nanocrystalline with 30% pure Al added consolidate, after compression test. 109
Figure 3.37: (a) Schematic representation of the layered ex-situ composite structure. **(b)** SEM image and elemental maps obtained from the interface region of the warm pressed $Al_{88}Sm_7Fe_5Ni_3$ amorphous/nanocrystalline and pure Al powders'..... 110
Figure 3.38: Density vs. added pure Al amount plot for warm pressed ex-situ composite consolidates..... 111
Figure 3.39: XRD patterns of warm pressed ex-situ composite consolidates with varying pure Al amounts. 112
Figure 3.40: SEM images taken from the surface of warm pressed ex-situ composite consolidates with pure Al amounts of **(a)** 0, **(b)** 1%, **(c)** 10%, **(d)** 20%, **(e)** 30% and **(f)** 40%. 113
Figure 3.41: Hardness results measured from the surface of warm pressed ex-situ composite consolidates with varying pure Al amounts..... 114
Figure 3.42: Compression test results of warm pressed ex-situ composite consolidates with varying pure Al amounts. 115

Figure 4.1: 2D surface plot of in-situ heating HEXRD results of melt-spun **(a)** $Al_{90}Y_5Tb_5$ and **(b)** $Al_{90}Sm_5Tb_5$ metallic glasses. 119
Figure 4.2: 3DAP reconstructions of **(a)** $Al_{90}Y_5Tb_5$ and **(b)** $Al_{90}Sm_5Tb_5$. Green isosurface corresponds to 95% Al concentration. 20% Tb (red) and Sm (green) isosurfaces are also rendered in **(b)**..... 120

NOMENCLATURE

APT/3DAP: Atom Probe Tomography

ASFN: $Al_{85}Sm_7Fe_5Ni_3$ Alloy

BF: Bright Field

BMG: Bulk Metallic Glass

BSE: Back Scattered Electron

DF: Dark Field

DSC: Differential Scanning Calorimetry

ECP: Efficient Cluster Packing

EDS: Energy Dispersive X-ray Spectroscopy

FWHM: Full Width at Half Maximum

EXAFS: Extended X-ray Absorption Fine Structure

FCC: Face Centered Cubic

FEG: Field Emission Gun

FEM: Fluctuation Electron Microscopy

FFT: Fast Fourier Transform

g(r): Pair Distribution Function/Pair Correlation Function

GFA: Glass Forming Ability

HAADF: High Angle Annular Dark Field

HEXRD: High Energy X-ray Diffraction

IM: Intermetallic Phase

LRO: Long-Range Order

MD: Molecular Dynamics

MRO: Medium-Range Order

Q: Wavevector

RE: Rare Earth Metal

RMC: Reverse Monte Carlo

S(Q): Total Structure Factor/Total Scattering Function

SAED/SAD: Selected Area Electron Diffraction

SAXS: Small Angle X-ray Scattering

SEM: Scanning Electron Microscopy

SRO: Short-Range Order

SSAR: Solid State Amorphization Reaction

STEM: Scanning Transmission Electron Microscopy

TEM: Transmission Electron Microscopy

TM: Transition Metal

TTT: Time-Temperature-Transformation Diagram

VFT: Vogel-Fulcher-Tammann Relation

WAXS: Wide Angle X-ray Scattering

XRD: Conventional X-ray Diffraction

XANES: X-ray Absorption Near Edge Structure

CHAPTER 1

INTRODUCTION

The topics of modern metallurgy and materials science are mostly account of crystalline materials; their atomic to micro to macro scale structures, their behaviour under certain external forces, namely thermal, mechanical, etc., and their performance parameters under these forces. The motivation of putting the crystalline materials on the spotlight is apparent, as most of the engineering materials used in technological applications are crystals. However, among a diverse classes of engineering materials, many types of amorphous materials are also readily being used, ranging from traditional ceramics and oxide glasses, engineering polymers, semiconductors to metallic glasses. For this reason, investigation of amorphous materials possesses critical importance to first understand the atomic scale structure and their behaviour under external forces for their optimization for usage as engineering materials.

As mentioned, the understanding of the atomic structure of amorphous materials is a key concept to understand this class of materials. Unlike crystalline materials which possess long-range ordering over very long distances, i.e. from several nanometres to even reaching millimetres, accompanied with a high order of rotational and translational symmetry, amorphous materials lack this highly ordered structure and can be described to be as a “random” structure, as far as the long-range ordering in crystals are concerned. Though amorphous structure is random relative to its crystalline counterpart, the structure of an amorphous material also possesses short-range ordering, which originates mainly from topological constraints in the three

dimensional space and the pair-pair interactions of constituents (if there is more than one constituent in the material). In the first part of this chapter, metallic glasses and their production methods will be introduced with respect to their historical, thermodynamical and kinetical aspects. In the second part, characterization techniques that are mostly employed in metallic glass research will be given in detail.

1.1. A Brief History of Metallic Glass Research

In the mid-20th century, production of metallic materials with a non-crystalline structure, i.e. metallic amorphous phase, was a heated controversy that it was thought to be non-achievable as such materials cannot be produced via the conventional techniques such as quenching into oil or water. The reason behind this belief is the insufficient cooling rate attained by quenching into liquid media due to the fact that during quenching, the material becomes covered with a blanket of quenchant vapour, which acts as a heat insulation layer, thus causing a decrease in cooling rate, hindering the production of metastable phases like amorphous phase.

The controversy on the production of metallic amorphous phase was solved by Duwez who synthesized the first metallic glass alloy in Au-Si system in 1960[1] with a rapid solidification technique that they called "splat-quenching". In this technique, rather than quenching into a liquid medium, the molten metal was dropped onto a cooled metal sheet, in order to obtain a complete metal-to-metal contact for enhanced heat extraction, which increases the cooling rate drastically, passing values of 10^6 K/s. Hence, they have successfully produced $Au_{75}Si_{25}$ metallic glass foils of several micrometres, which did not show any sharp crystalline peaks in the corresponding X-ray diffraction pattern.

As the production of non-crystalline alloys was proven to be plausible, a great deal of research was initiated on metallic glasses, and within the following years several different alloys with increased amorphous phase stability were developed. In 1969, Chen and Turnbull[2] have developed binary Pd-Si and ternary Pd-Si-X, where X=Cu, Ag & Au, metallic glasses, which require lower cooling rates, around 100 K/s. In 1974, Chen developed $Pd_{40}Ni_{40}P_{20}$ ternary metallic glass alloy that can be casted into rods of

1-3 mm in diameter with water quenching, which was assessed as the first bulk metallic glass (BMG) forming alloy[3]. Few years later, Turnbull et al., have casted the same metallic glass alloy into rods of 1 cm using B_2O_3 fluxing[4], further enlarging the casting diameters of BMGs.

Along with the progress in development of metallic glasses with higher glass forming abilities (i.e. metallic glass alloys that could be cast into a non-crystalline structure with larger sizes), novel alloys with intriguing properties was synthesized, as well. In the late 1960s, Duwez and Lin showed that Fe-P-C metallic glass that was produced by "pistol-and-anvil technique" showed ferromagnetic behavior[5]. In the following years, many iron based compositions were developed that are showing ferromagnetic behaviour. Among them $Fe_{100-X}B_X$ binary metallic glass[6] and Fe-B based metallic glass systems (and their crystalline counterparts) have been studied extensively due showing highly ferromagnetic properties. These alloys even became commercially available under brand names Metglas®, Finemet®, Nanoperm® and Hitperm®. The discovery of iron based metallic glasses did not only open a window for a new class of magnetic materials, but also showed that the need for noble metals, such as Au, Pd, Pt and Ag, are not essential in order to obtain amorphous metallic phase.

One other historic example of production of binary metalloid-free (Si, Ge …), metal-metal non-crystalline alloy is the Zr-Cu system. The binary Zr-Cu metallic glass alloys were first synthesized by Ray et al. in 1968[7] via splat-quenching. The discovery of Zr-Cu system has both scientific and practical significance. Due to their higher glass forming ability[8], these alloys can be cast into 1-3 millimetres with relatively low cooling rate, ~250 K/s, depending on the composition[9]. Thus, due its ease of production, and its simplicity in term of number of constituents, Zr-Cu system has being highly studied as it is a convenient system to study the structure of metallic glass alloys[10–13]. Besides the structure studies, further increment of GFA was being studied with varying the composition in binary[8,14] and also addition of solute elements has also being studied[15–18] for both Zr-rich and Cu-rich alloy systems. In 1993, Johnson and Peker[19] had synthesized $Zr_{41.2}Ti_{13.8}Cu_{12.5}Ni_{10.0}Be_{22.5}$ metallic glass with conventional water quenching, which corresponds to a cooling rate around 1 K/s, with sizes as large

as 14 mm. Later this alloy was become commercialized under the brand name Vitreloy 1®[20], and many derivatives of Vitreloy 1® with slightly different compositions and/or with different alloying elements, namely Vitreloy 4® with slightly higher Be content, Vitreloy 105® which replaces Be with Al, etc. Hence, the example of Vitreloy® family solidly proves that metallic glasses not only serve for scientific curiosity, it is a novel materials class that actually could be readily used as structural materials.

After the discovery of the amorphous metallic alloys, within two decades, many advances had been made in development of metallic glasses with different bases, namely Ni, Co, Cu, Ti, W, Rare-Earth metals, Mg, and Ca. However, aluminium based metallic glasses had not yet developed until early 1980s. Though several attempts had been made to produce Al-based metallic glass by synthesis of binary Al-X, X=Si, Ge, Cu, Ni, Cr, and Pd, production of single phase amorphous structure without any crystallinity was not achieved with high cooling rate rapid solidification methods[21]. In 1981, Inoue et al. first synthesized Al-based metallic glass alloys in Al-Fe-B and Al-Co-B systems with Al contents higher than 50 at%[22]. However, due to the brittle nature of these alloys, they did not gather much attention. Several years later, production of the first Al-based metallic glass with decent bending ductility was achieved again by Inoue et al. in Al-Si-X and Al-Ge-X systems, X= Cr, Mn, Fe, Co, Ni, with high Al content (~80 at%) via melt spinning technique[23]. The achievement of Al-based glasses with good mechanical properties had instigated the development of Al-based metallic glass alloys. In the following years, several ternary amorphous alloys with compositions having high Al content, having at least 70 at%, alloyed with two different transition metals (TM) had been produced to obtain alloys with better glass forming abilities and better material properties. However, the breakthrough that paved the way for Al-based metallic glasses to be attributed as the candidate for new class of structural materials had occurred at the end of the decade. In 1989, the Inoue Group in Tohoku University, Japan and the Shiflet Group in University of Virginia, US announced their discovery of Al-Rare Earth (RE, lanthanide metals)[24–26] and Al-RE-TM[27–32] metallic glasses comprising high Al content with superior mechanical properties as compared to both previous Al-based metallic glasses and conventional Al alloys. These alloys have typical constitutions of 85-95 at% Al and 15-5 at% RE in

binary form and 80-90 at% Al and rest being equiatomic or non-equiatomic mixtures of RE and one or more TM atoms, and produced via rapid solidification techniques. In the following years, Al-RE binary system has become the basis of the developed Al-based bulk metallic glasses (BMGs). By optimizing the alloying, i.e. by adjusting the number of TM species added and amounts of TM added, as well as the synthesis technique, both glass forming ability and materials properties have been tailored. A recent example is the production of bulk fully dense structure of 10 mm from an exotic $Al_{86}Ni_6Y_{4.5}Co_2La_{1.5}$ amorphous alloy powder[33], having a fracture strength of 1250 MPa.

If the historical evolution of metallic glasses is followed from its start in 1960s till the current times, one can see the emergence of a novel material class from a mere scientific curiosity. The studies on the production of solid metallic amorphous structure that was shrouded in mystery is now enabled scientists and engineers to develop new non-crystalline metallic materials having superior properties which their crystalline counterparts may never can reach. However, to effectively produce and use a material, one should have the knowledge about physical phenomena that has been taking place during the production and the service lifetime; i.e. without the scientific background, one can never have optimized the performance of a material. Though it has been 50 years since Duwez et al. synthesized, the metallic glasses had begun to commercialize around 2000s, as the enigma of structure of amorphous metallic phases, the alloy design, and also the performance parameters is being clarified. The aforementioned Al-based BMG having 1250 MPa strength nearly quadruples the conventional, commercially available Al alloys[34], making itself a privileged candidate to the market. Hence, the research on the behaviour under various forces and the alloy design on metallic glasses have a crucial importance to further increase the commercialization of these alloys to replace crystalline materials.

1.2. Glass Formation and Production Routes of Metallic Glasses

In a general sense, the glass production is thought to be done through cooling of a molten material. As in the very well-known cases such as production of window glasses and amorphous polymers this understanding holds. However, it is not

mandatory to use solidification processes to obtain non-crystalline structures. For many engineering materials, as advanced ceramics, amorphous semiconductor materials, and metallic glasses, different production routes could also be employed. These production routes can be classified into three main categories, namely by rapid solidification, by mechanical methods, and chemical derivation.

Metallic glasses are mostly produced by rapid solidification, and with mechanical methods, namely mechanical alloying and milling; thus the emphasis will be on this two routes. For the ease of understanding, in the initial part of this section the glass formation upon cooling of a liquid phase will be explained in detail, by taking thermodynamic and kinetic aspects into account, then its implementation on the production routes will be given in the latter parts.

1.2.1 Glass Production

As apparently known, the liquid has a "structural randomness" as compared to crystals; meaning that the liquid structure lacks longer range correlations that crystals have. Thus upon cooling of a liquid, for the formation of a crystalline nuclei diffusive replacements of atoms are needed. However, for the formation of a crystal, a certain energy has to be supplied to the system in order to create the interface between the ordered and the disordered configurated regions. The liquid compensates this energy requirement by supercooling; i.e. cooling beneath the equilibrium melting temperature whilst preserving the liquid state, becoming a supercooled liquid. During the supercooling, the viscosity of the supercooled liquid also decreases as a function of temperature with Vogel–Fulcher–Tammann (VFT) relation:

$$\eta = \eta_0 \, exp\left[D^* * \frac{T_0}{T - T_0}\right] \qquad \text{Equation 1.1}$$

where η is the viscosity, η_0 is the viscosity at infinite temperature, D^* is the kinetic fragility parameter and T_0 is the VTF temperature[35]. As the liquid is cooled down, at some certain temperature the viscosity of the supercooled liquid rose up to fifteen orders of magnitude where the material becomes rigid[36]. This particular temperature is called as the glass transition temperature, T_g. At glass transition temperature, the

viscosity becomes so high that the atomic diffusion is retarded drastically, as compared to the liquid state, thus the formation of crystalline nucleus, which is a diffusion dominated process, is inhibited.

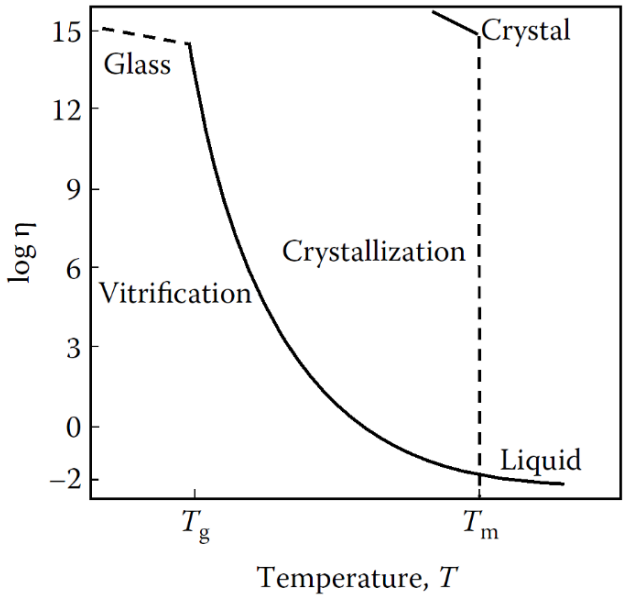

Figure 1.1: Viscosity vs. temperature plot for crystal and glass formation. Adopted from [36].

Glass formation can be also detectable with thermodynamic state functions' perspectives; as variation of specific volume (volume per unit mass) and specific heat, C_p, with respect to temperature. As seen in **Figure 1.2**.(a), for equilibrium cooling conditions, upon cooling a sudden drop in specific volume of liquid is observed at melting temperature, an indicative of crystalline solid formation. In the case of glass formation, the liquid by-passes the abrupt volumetric shrinkage and continues to undercool up to T_g. As stated earlier, the viscosity is continuously increasing while the volumetric shrinkage is taking place during the undercooling, and it reaches quite a high value where the undercooled liquid becomes "frozen" at the glass transition temperature; leading to the glass formation. For the specific heat capacity point of view, for equilibrium cooling conditions, the C_p of the liquid shows a similar rapid drop at melting point, manifesting the crystalline solid transformation (**Figure 1.2**.(b)).

As for the glass formation, the C_p of the liquid increases in an exponential manner during the undercooling and a sudden drop occurs on glass transition.

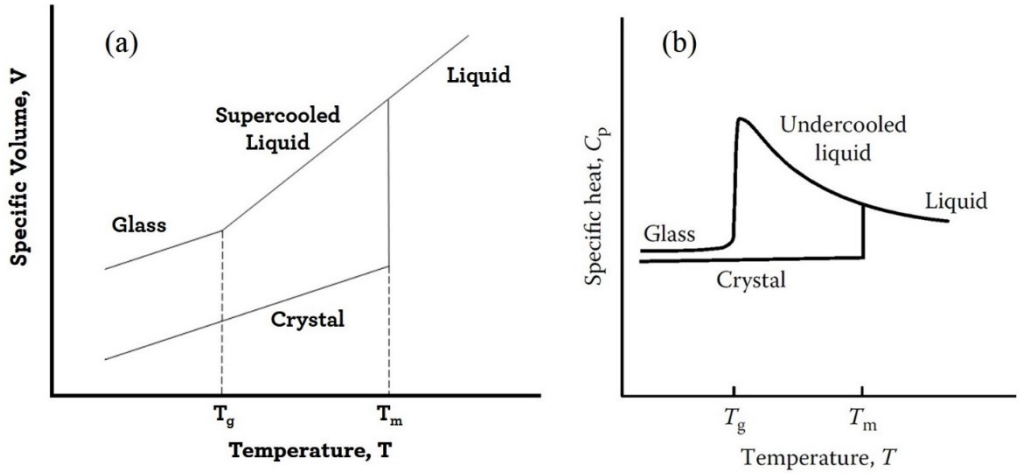

Figure 1.2: Variation of **(a)** specific volume and **(b)** specific heat [36] with temperature.

An important point should be accounted for the liquid to glass transformation is that the glass transition temperature, T_g, is not a thermodynamical constant for a glass forming material; rather it is a kinetic parameter[37]. Consider one quenched two liquids without crystallizing, one with a fast cooling rate and other with a rather slower cooling rate. For the slower cooling rate quench, the liquid will hold its metastable equilibrium to much lower temperatures than the higher cooling rate quench. Thus, the glass transition temperature of the slowly cooled one will be lower as compared to the higher one. This phenomenon also its structural and thermodynamic consequences: as compared with its higher cooling rate counterpart, the glass with lower cooling rate will have lower density and higher viscosity. Hence, a paradox arises: If a glass is cooled with a very low cooling rate without forming any crystals, at some finite temperature, the density of the glass would become equal to the crystal of the same composition, implying that the glass and crystal would be isentropic. This finite temperature is defined as the "ideal glass transition temperature". Then, with decreasing temperature, the glass would have lower density than that of the crystal, hence, its entropy would also be lower. Though there is no thermodynamic constraint

for glass to have lower entropy than its crystal, it is a structurally unlikely situation. This paradox was proposed was Kauzmann[38] in 1948, and Kauzmann himself provided a solution to this problem by stating that during supercooling, no matter how slow the cooling rate is, a phase transformation (glass transition, a sudden crystallization event, etc.) should take place before reaching the ideal glass transition temperature.

From the thermodynamics perspective, the glass formation capability of an alloy system can be assessed by its equilibrium phase diagram. As cooling from the liquid, in two phase regions of solid and liquid, there exists a hypothetical line called T_0 line, in which the free energy of liquid and solid phases are equal[39]. When the local liquid-solid interface equilibrium is altered via non-equilibrium processing (such as rapid solidification), and by extending the T_0 line below the metastable eutectic line, two different microstructures can be obtained: If the equilibrium low solute content solid solutions have the similar crystal structures, the T_0 line shows a continuous behaviour, thus complete solid solubility of both alloying constituents is obtained, as seen in **Figure 1.3**.(c). However, if the equilibrium low solute content solid solutions have dissimilar crystal structures with low solid solubility in both sides of the phase diagram, T_0 lines that are extrapolated from both sides of the phase diagram does not intersect and reveal a glass-forming region.

1.2.2 Glass Forming Ability

As stated earlier, glass forming ability of an alloy can be explained as its capability of forming an amorphous structure through various amorphization techniques. Furthermore, the definition of glass forming ability also comprise the measure of thermal stability; i.e. higher the glass forming ability, lower the required cooling rate to obtain amorphous structure, and further, higher the resistance to crystallization.

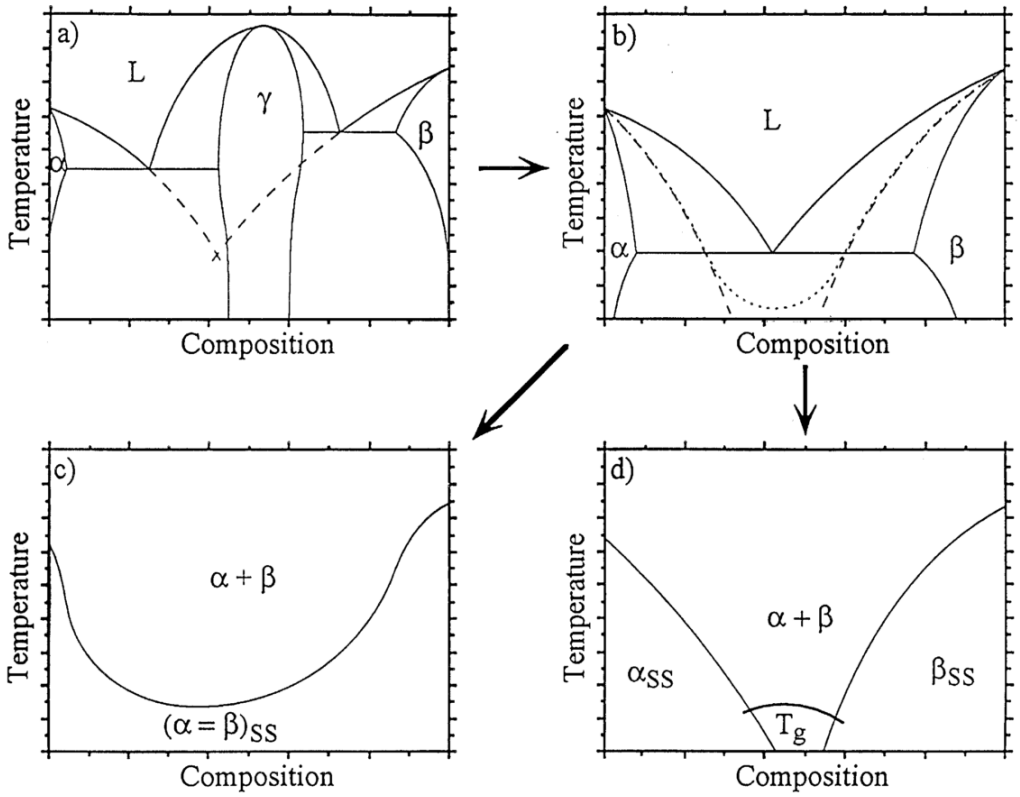

Figure 1.3: Schematic phase diagram of a hypothetical alloy under **(a)** equilibrium and **(b)** non-equilibrium processing conditions. The conditions of the intersecting and non-intersecting T_0 lines are given in **(c)** and **(d)**, respectively. Retrieved from [39].

Although, glass forming ability of an alloy can vary on the production route that is used[40] due to differences in thermodynamics and kinetics associated with each technique, there still exists a few empirical rules that lighthouse the alloy design of metallic glasses[36,41]. These rules can be listed as:

i. Having at least three alloying constituents,
ii. Choice of elements having negative enthalpies of mixing,
iii. Choice of elements such that atomic size difference between them exceed 12%.

As stated earlier, though these rules are empirical, the idea can be explained through "the confusion principle"[42]. The confusion concept states that due to increment in the complexity of the system, a struggle is faced during the formation of crystalline species from a high number of choices. Hence, the system chooses the formation of an amorphous structure as it is easier to form with respect to the candidate crystalline

structures. The ease of amorphous structure can be further supported kinetically with the depression in the long range diffusion of alloying constituents within a complex system.

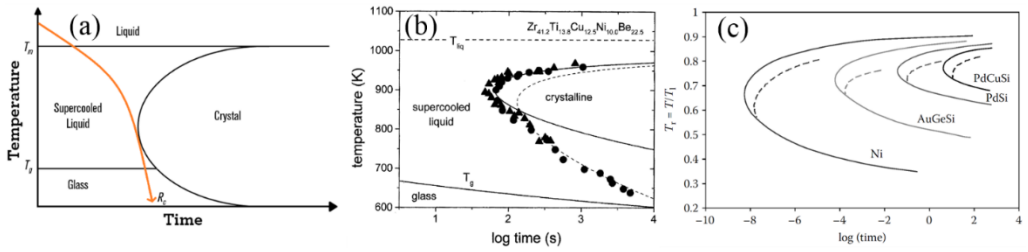

Figure 1.4: (a) A sketch of TTT diagram for a metallic glass. **(b)** Measured TTT diagram of Vitreloy 1®[43]. **(c)** Calculated TTT diagrams of pure Ni, and AuGeSi, PdSi and PdCuSi alloys[36].

The glass forming ability of an alloy could also be expressed by measuring the well-known time-temperature-transformation (TTT) diagram of an alloy. As one can observe in **Figure 1.4**.(c), the nose of the c-shaped curve, the curve representing the crystallization reaction, shifts to longer time periods with an increment in the glass forming ability. As it can be seen in the mentioned figure c-curve of the pure nickel is placed on the leftmost side of the TTT diagram, whereas as the glass forming ability increases (with composition in this particular case), the crystallization curves of the alloys shifts to rightward positions, indicating an increment for the time needed for amorphous (or supercooled liquid) to crystal transformation. Further, one can also observe the effect of the confusion principle in **Figure 1.4**.(c): when PdSi alloy is microalloyed with copper, PdCuSi, its glass forming ability increases, as its c-curve shifts rightward direction in the TTT diagram.

The confusion principle also proposes an answer to the low glass forming ability of pure metals, as well. Since diffusivity of atomic species is quite high in an unary system[44], coupled with relatively low viscosity of metallic melts (with respect to ionic glass forming systems, e.g. SiO_2…), rate of nucleation of crystalline nuclei is quite rapid, which hinder the glass formation. Very recently, Zhong et al.[45] had reported formation of amorphous tantalum of several tens of nanometres, produced with a

novel, ultrafast quenching technique under *in situ* transmission electron microscope (TEM), with a cooling rate of ~10^{14} K/s. Together with the given explanation and experimental findings, one can comprehend the reason behind the extremely low glass forming ability of monoatomic metallic glasses.

Metallic glass alloys are classified into two groups, with respect to their solidification rate requirements, as

i. Marginal glass forming alloys, requiring very high cooling rates of ~10^5-10^6 K/s,
ii. Bulk metallic glasses, requiring lower cooling rates, mainly less than ~10^3-10^2 K/s.

As it can be inferred from the explanations given above, the glass forming ability of metals and metallic alloys is considered from a liquid-amorphization-precursor point of view. However, as it will be introduced in the upcoming sections, glass forming ability of alloys can be altered via changing the amorphization precursor or production technique.

1.2.3 Rapid Solidification Techniques

As one can deduce from the previous history section, rapid solidification is the technique that enabled production of amorphous alloys, and ever since it has been the most popular method for metallic glass synthesis. During the years, several rapid solidification techniques were evolved. As stated earlier, first metallic glasses were produced splat-quenching and piston-and-anvil methods. Today, high cooling rate methods, as melt spinning, splat quenching and gas atomization systems commercially available and readily being used. For glasses requiring lower cooling rates, casting methods such as suction, chill, injection and die casting are commonly used. Though the amorphization precursor is gas phase instead of liquid phase, vapour deposition methods such as DC magnetron sputtering technique are also considered as a rapid solidification technique and are being used both for scientific and commercial purposes. In the following section, the techniques used in this study, melt spinning and magnetron sputtering, will be emphasized with its commentary on the glass forming ability.

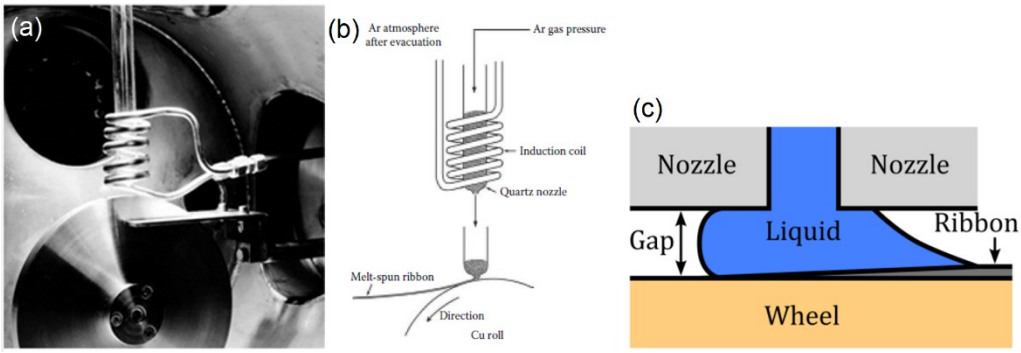

Figure 1.5: (a) Cu-block melt spinning device used in this study [Retrieved from [46]]. **(b)** Schematic representation of a melt spinner [Retrieved from [36]]. **(c)** Close-up schematic of solidification process on Cu-block [Retrieved from [47]].

1.2.3.1. Melt-Spinning Technique

One of the most revolutionary development in metallic glass history is development of the melt-spinning technique. It was first developed by Pond[48] in 1958 to produce metallic strips of different thicknesses with high cooling rates. The method consists of melting the material with induction heating, and ejection of the liquid onto a rotating metal wheel, having a tangential speed of several meters per second. Melt-spinning is generally done under controlled atmosphere for prevention from oxidation reactions. By adjusting the process parameters, such as liquid's ejection temperature, melt ejection pressure, nozzle geometry, nozzle-wheel gap distance, tangential speed of the wheel, various undercooling values and high cooling rates can be easily obtained. Generally, cooling rates of ~10^5-10^6 K/s are essential for melt-spinning. In the previous section of the chapter, the thermodynamics and kinetics of glass formation was introduced from melt spinning's perspective, thus it won't be recapped here.

1.2.3.2. Magnetron Sputtering

Magnetron sputtering is a well-established rapid cooling technique for obtaining amorphous and/or nanocrystalline metallic thin films. A metallic thin film is obtained by magnetron sputtering with the following steps: (i) A plasma of a noble gas, generally Argon, is generated in a vacuum chamber. (ii) The highly energized

positively charged noble gas ions hit either a target of with the desired nominal composition or targets of the constituent elements, and evaporate the material desired to be deposited. (iii) With the help of an applied electric field, the evaporated material(s) is deposited on the cryogenically cooled substrate, forming a metallic thin film. Generally, cooling rate of magnetron sputtered thin films are estimated as ~10^9 K/s.

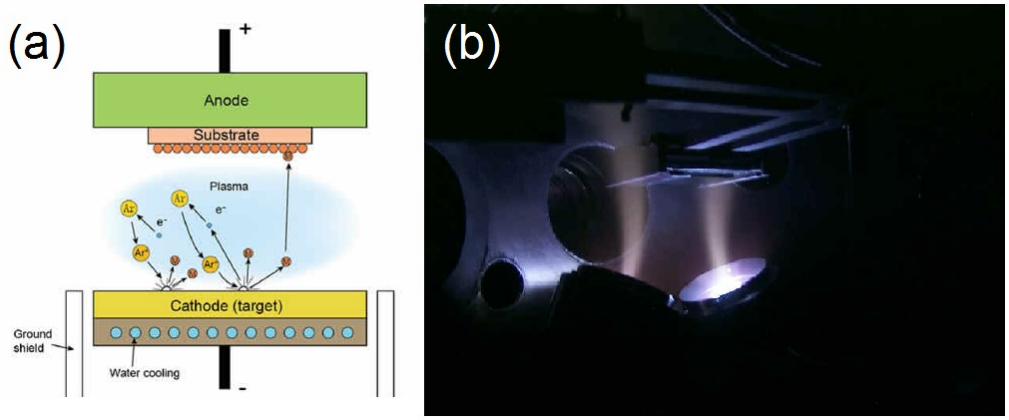

Figure 1.6: (a) Schematic representation of magnetron sputtering and **(b)** magnetron sputtering device [Retrieved from [49] and [50], respectively].

As it can be inferred from the latter explanation, differing than quenching from a melt, in magnetron sputtering, the material solidifies directly from a vapour phase. However, the previous thermodynamical explanation of glass formation from liquid quenching is still applicable for the glass formation in the magnetron sputtering, but with a different kinetic process to hinder the diffusion of atoms. As stated, the thermodynamics of the glass formation for liquid quenching still holds for sputtering case, as the glass forming ranges for both methods are highly matching[36,40]. Nonetheless, the kinetic aspect of viscosity increment upon glass transition temperature is not valid for sputtering, due to the fact that in sputtering, the amorphous phase formation occurs as the vapour phase condenses directly to the solid non-crystalline phase. Whereas, in sputtering, the substrate temperature is the key kinetic parameter for amorphization: as stated earlier, during the film deposition, the substrate is cooled down to cryogenic temperatures, decreasing the surface mobility of the deposited atoms drastically, thus hindering the crystal phase formation which is known

to be a highly diffusion-driven process[21,36,39,51–53]. Hence, the key factor for glass formation (in the glass forming composition range) for magnetron sputtering is the substrate temperature, especially for marginal glass forming alloys.

There are some pronounced disadvantages of magnetron sputtering of metallic thin films, which are the size limitations (films can be deposited for several microns at most), extremely slow deposition rate, and difficulty of composition and microstructure control. To deposit thin films with desired composition and microstructure (in our case it is a single amorphous phase), deposition is performed with a quite slow rate, which inhibits its usage as structural materials. The reason behind most of these issues could be attributed to the stochastic nature of the sputtering process[36].

1.2.4 Glass Formation Through Mechanical Milling and Alloying

In the course of metallic glass research, it was shown by several different studies that an amorphous metallic phase could be obtained with processes in solid-state, without involvement of any liquid or vapour phase. These processes are generally called as "solid-state amorphization reactions (SSAR)"[36,40,53,54].

The concept of amorphization through mechanical means has started in the early 1980's. In 1981, Yermakov et al.[55] had shown that amorphous phase can be obtained via mechanical milling of pre-alloyed Y-Co intermetallic powders. A year after Yermakov's study, Koch et al.[56] had observed mechanical alloying of pure Ni-Nb powders could end up having metallic amorphous phase. Through the discovery of SSAR with mechanical milling and alloying, various methods for producing amorphous metals at solid-state has been developed. Most widely studied methods can be listed as irradiation methods, pressure-induced amorphization, severe plastic deformation, multilayer amorphization[36,53,54]. As stated in the introduction part of this section, only mechanical alloying and milling were used in this study, hence, solely their thermodynamic and kinetic aspects will be given.

1.2.4.1. Mechanical Milling

Mechanical milling process is one of the most widely used method to produce amorphous materials in large quantities. Mechanical milling process is generally performed with two different kinds of mills: planetary ball mills and shaker mills, which are also known as low energy and high energy ball mills, respectively. The milling process is done by feeding pre-alloyed powders or intermetallic compound powders to a ball mill with certain number of balls. One thing that should be considered for the milling process is that the hardness of the vial that powders and balls are fed and hardness of the balls should match, and should have a higher value than that of the fed powder. If hardness equality requirement of the vial and the balls is not satisfied, the vial will be deformed by the balls as the milling continues, thus end up introducing impurities to the milled powder.

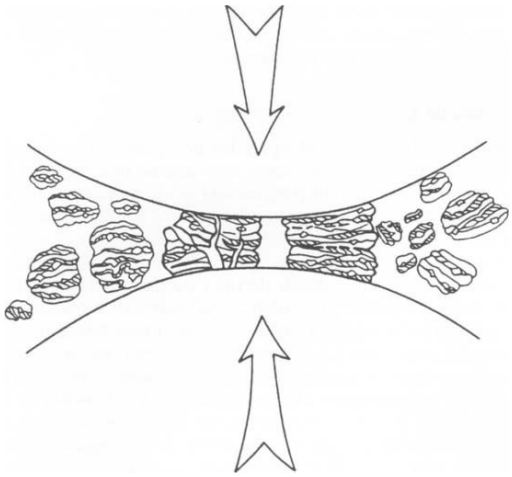

Figure 1.7: Schematic representation of a collision in mechanical milling and alloying [Retrieved from [54]].

Although SSA reactions, as mechanical milling, occur in solid-state, their thermodynamics are generally explained as "energize and quench" techniques[36,54], meaning that an energetic external force is applied to materials, pushing them to transform into metastable phases. The phenomenon that "energizes" the milled powders is the entrapment of powders between the colliding balls during the milling. The ball collisions exert quite large amount of energy via plastic deformation to the

powders entrapped between the balls. Two phenomena that powders encounter during the milling is called as “cold welding” and “fracture”. Cold welding is explained as the fusion of the particles (without melting) during a collision event and fracture is the breaking of the previously “cold welded” particles in a collision event. As the powders are milled, they plastically deform with the mentioned phenomena, by which crystal defects such as dislocations, vacancies, stacking faults, anti-phase boundaries etc., happen to accumulate in the powders, together with continuous decrease in grain size with extended deformation, increasing crystalline phase’s overall free energy. After milling to some extent, the crystal defects build up in the powders increases the total free energy of each particle to a level, for which the total free energy of the crystalline state surpasses the free energy of the amorphous state. Hence, the crystalline lattice breaks down to the amorphous structure to decrease its total free energy.

Mechanical milling method is used for amorphization of metallic alloys, as well as the amorphization of intermetallic compounds. As it can be seen from Figure 1.8, mechanical energy that is applied to the material causes a break down on long-range ordering, analogous to heating of an alloy or an intermetallic compound of a certain composition up to melting.

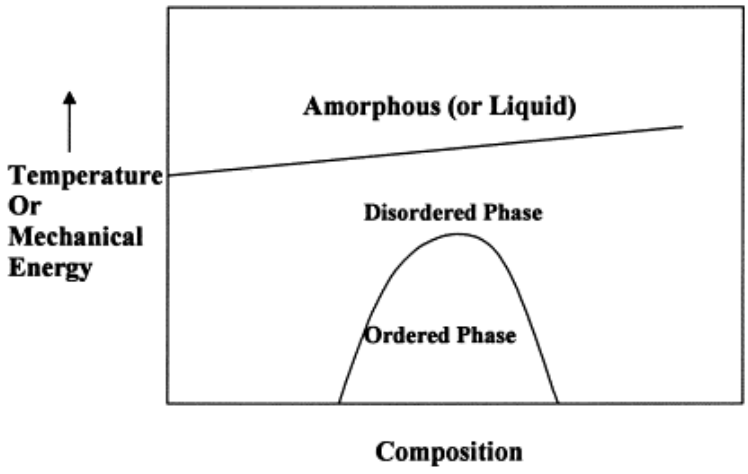

Figure 1.8: Analogical phase diagram of temperature or exerted mechanical energy versus composition [Retrieved from [57]].

Kinetics of amorphous phase transformation from crystalline phase(s) is governed by the milling parameters, namely, energy input per unit time (i.e. usage of either low energy planetary ball mill or high energy shaker mill), the ratio of the weight of the balls that are put inside the vial to the weight of the fed powder (shortly "ball-to-weight ratio"), and temperature. As their name implies, the time required for amorphization with high energy milling with shaker mills, are less than its low energy mill counterpart. Hence, for a certain glass forming alloy, amorphous metallic phase formation takes longer times in planetary ball milling with respect to milling with a shaker mill. Furthermore, it was observed that for a certain glass forming alloy composition, the ball-to-weight ratio is inversely proportional with the time required for amorphization[58]. Likewise, due to the apparent reason that amorphous phases' stability is inversely proportional with the temperature, milling at lower temperatures favour the amorphization more with respect to milling at higher temperatures[54].

1.2.4.2. Mechanical Alloying

Like as milling, mechanical alloying is also a widely used method for production of amorphous alloys. Mechanical alloying can also be employed with planetary and shaker mills. The mechanisms of cold welding and fracture that are explained in the mechanical milling section are applicable for this method, as well. The main difference of mechanical alloying over milling is that in the former pure elemental powders of the nominal composition for the desired alloy is fed directly to the vial. Meaning that unlike mechanical milling, the intermixing of elements into each other also takes place during the mechanical alloying[36,53,54].

The amorphization reaction in mechanical alloying can occur with one of the following reaction paths[54]:

$$mA + nB \rightarrow (A_mB_n)_{amorphous}$$

$$mA + nB \rightarrow (A_mB_n)_{crystalline} \rightarrow (A_mB_n)_{amorphous}$$

The reaction routes given above can be explained as whilst the mechanical alloying of pure elemental powders is taking place, amorphous phase could form either from

directly from the pure elemental powders or formation of a transient crystalline phase, such as (supersaturated, i.e. non-equilibrium) solid solution and/or an intermetallic phase. An example for the phase evolution during mechanically alloying of Al-Ti-Cu alloy with X-ray diffraction (XRD) patterns can be seen in **Figure 1.9**. As seen in the figure, at first (~1 hours) the peaks of elemental phases are observed. After milling for several hours, the formation of transient crystalline phases is detected, which thereafter decompose to form an amorphous phase.

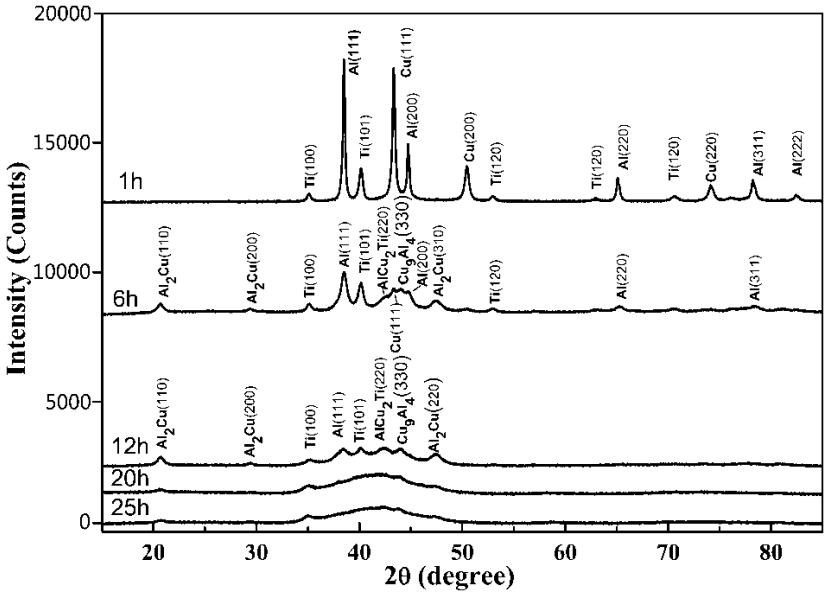

Figure 1.9: Phase evolution of mechanically alloyed $Al_{65}Cu_{20}Ti_{15}$ alloy through XRD patterns[**59**].

The thermodynamical aspect of amorphization through mechanical alloying is similar to the explained hypotheses in the mechanical milling section. Likewise, as mechanical milling, in mechanical alloying, elemental powders are "energized" via entrapment of powders during the stochastic ball-collision events. However, unlike mechanical milling, in mechanical alloying, the energy gained by the powders are used for different processes throughout the process. At the initial stage of the mechanical alloying, the exerted energy is used for the alloying process; i.e. the energy that is supplied is used by powders to distribute the alloying elements homogeneously. After

the alloying of elements is completed, the powders are continued plastically deform, accumulating aforementioned crystalline defects, hence, after the total free energy of the crystalline alloy exceeds the free energy of the amorphous phase, crystalline to amorphous phase transition occurs.

The kinetic aspects of mechanical milling are completely applicable to the mechanical alloying, as well. Thus they will not be mentioned in this section to avoid repetition.

An intriguing aspect that should be mentioned that mechanical alloying is capable of producing amorphous metallic alloys that are impossible to produce via rapid solidification techniques; meaning that alloys that are not in the glass forming range of their system could be produced by mechanical alloying[36].

1.3. Structural and Dynamical Characterization of Metallic Glasses

Complete understanding the atomic structure of metallic glasses is an important goal to achieve, since one can dominate the properties and the performance of a material if and only if one knows the true atomistic mechanisms that govern the materials behaviour. Thus to unveil the mysterious and enigmatic structure of metallic glasses both simple conventional laboratory techniques, such as differential scanning calorimetry, and cutting edge, state-of-art characterization techniques, like synchrotron radiation are complimentarily used. In this section, the characterization techniques that were employed during the course of this study will be introduced briefly. The reader should be aware that, even though the following techniques have diverse applications on materials research, only their application to characterization of metallic glasses will be given.

1.3.1 Differential Scanning Calorimetry

Differential Scanning Calorimetry (DSC) is a simple yet powerful technique to track the thermally activated physical changes taking place in a matter. In metallic glasses, several phase transformation events (**Figure 1.10**), such as glass transition, crystallization reaction(s), melting, etc. can be tracked and the corresponding changes

taking place during these transformations, like heat capacity changes, enthalpy changes during transformations (i.e. either heat dissipated or absorbed during reactions), and critical temperatures, such as crystallization, glass transition, melting temperatures, can be monitored with ease solely by DSC.

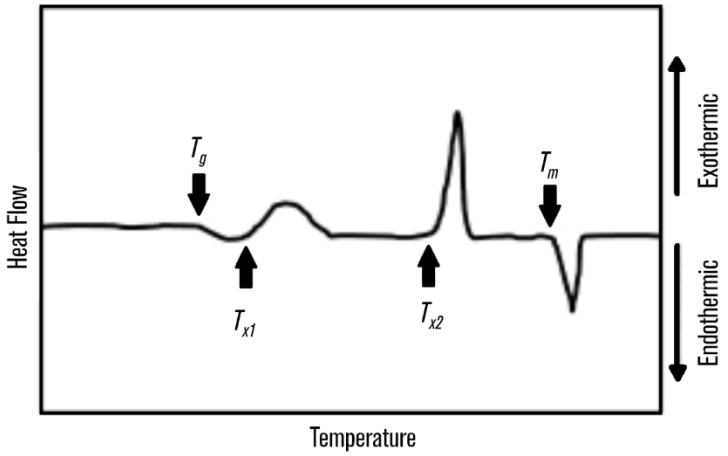

Figure 1.10: Typical DSC thermogram of a metallic glass alloy [Adapted from [60]].

The device consists of two individual heating units; one for the empty reference holder, the other for the holder that is filled with the material to be studied. The holders made out of aluminium or copper, depending on the reactivity of the sample, together with the maximum target temperature to be reached. The calorimetric measurements are done with two different testing routes. If the reference and the specimen holders are continuously heated with a constant heating rate within a certain temperature range, the procedure is called as isochronal heating. Conversely, if the reference and the specimen holders are rapidly heated up to a predetermined temperature and hold for a certain amount of time, the procedure is called as isothermal heating.

As its name implies, DSC is a calorimetric technique. Thus, DSC detects the phase transformations via the heat flow difference between the empty holder and the sample holder through the application of a constant heating rate on both holders; as no reaction is taking place in the empty holder, the differences in the heat flow of both holders give out the enthalpy change in the material. It is a well-known fact that, when a fully amorphous metallic glass sample is heated up (assuming that the material exhibits a

distinct supercooled liquid region), the material first goes through glass transition near the glass transition temperature, a second-order-like reaction[61,62], then possible crystallization reactions take place up to melting, which are known to be first order reactions. Furthermore, it is well known that glass transition is a pseudo-endothermic event and there happens to be a heat capacity change associated with it; conversely, crystallization reactions are exothermic events and there exists a subtle heat capacity change due to introduction of crystallization products into amorphous matrix.

As it was explained that DSC is sensitive to thermophysical changes occurring in the materials through the commencing reactions, critical reactions and their temperatures can be detected. However, one cannot detect any chemistry changes that are taking place; i.e. phase transformations could be tracked with DSC thermograms with respect to either time or temperature, yet, no chemical information about the chemistry of the reaction product(s) could be obtained solely through DSC experiments. Hence, it should be used complimentarily with scattering and microscopic examinations to obtain a more complete picture of the transformations that are taking place.

1.3.2 Transmission Electron Microscopy

Among vast variety of optical characterization techniques, transmission electron microscopy (TEM) is considered as one of the most powerful methods for investigation of materials. The power of TEM mainly comes from its versatility; with different TEM techniques one can conduct experiments ranging from various scattering experiments to crystallographic analysis to spectroscopy on nanometre scale to imaging of individual atoms, etc. Combined with its angstrom to sub angstrom resolution capabilities, the diverse experimental opportunities that TEM provides are extensively used in metallic glass research.

Albeit its usage as atomic level structural analysis tool, one of the most basic and essential employment of TEM analysis is its usage for confirmation of the fully amorphous phase of as-produced states of metallic glasses with both imaging and electron diffraction. **Figure 1.11** shows a typical bright field image (BF) and selected area diffraction pattern (SAED) of a melt-spun $Al_{90}Tb_{10}$ metallic glass alloy. As it can

be seen from the figure, BF image is nearly featureless, without any definitive contrast, an indication of the fully amorphous structure. The accompanied diffraction pattern (**Figure 1.11**.(b)) acquired from the same area of the sample also confirms the amorphous structure, as only diffuse amorphous halos are observed without any crystalline diffraction spots or any ring pattern.

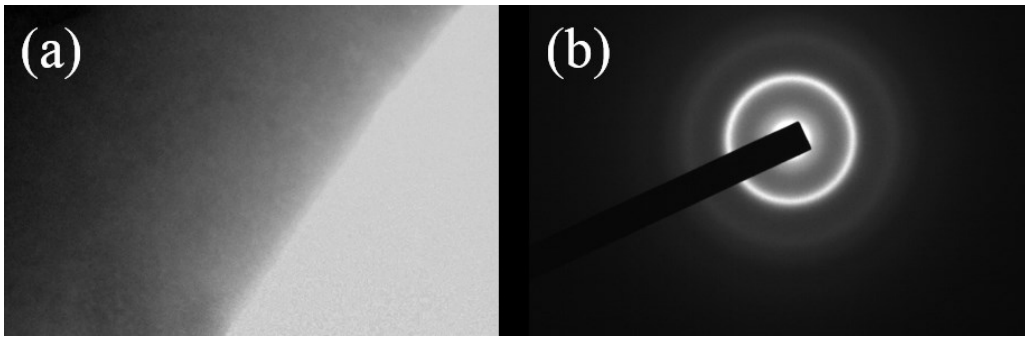

Figure 1.11: Bright field image and selected area diffraction pattern of an as-spun $Al_{90}Tb_{10}$ metallic glass alloy [Courtesy of T. Demirtaş].

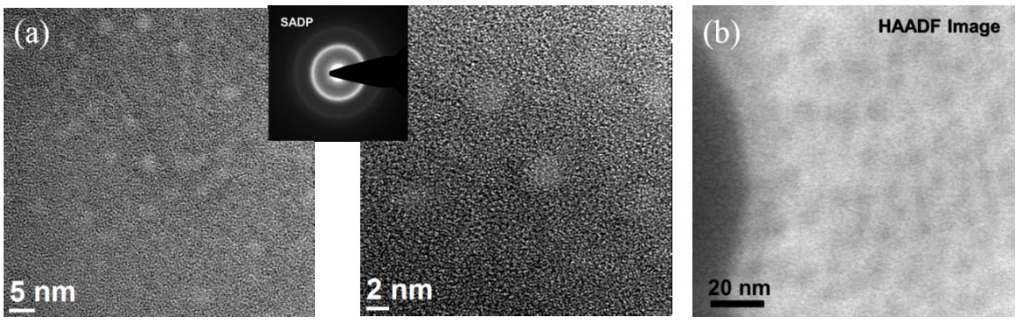

Figure 1.12: (a) HRTEM images of phase separated $Al_{90}Sm_{10}$ metallic glass. Inset shows the SAED pattern of the same region. (b) HAADF imaging of the phase separated regions of the same alloy [Courtesy of M.J. Kramer and R.T. Ott].

Novel TEM techniques enable users to study the nanometre-to-atomic scale features, such as morphology of these features (e.g. shapes of precipitates, interfaces…), structural defects (e.g. dislocations, shear bands…) as well as their chemistry of these features. One of the major advantages of using TEM in an amorphous/nanocrystalline sample is the diffraction contrast. An example for these explained techniques are given in **Figure 1.12**: an as-sputtered $Al_{90}Sm_{10}$ metallic glass alloy was *in situ* heated till

the amorphous structure is separated into Al-rich and Al-deficient islands, and they were characterized with high resolution transmission electron microscopy (HRTEM), coupled with and high angle annular dark field (HAADF) imaging. **Figure 1.12**.(a) shows two HRTEM images of phase separated regions with the inset, SAED pattern of the same area; as the composition (and probably the structure) of these regions differ, Al-rich regions of 2-5 nm (lightly coloured regions) can be identified easily. Furthermore, to analyse the structure more chemically, HAADF imaging was used and given in **Figure 1.12**.(b). This time, contrast mechanisms related to chemical difference reveal nanometre scale regions with ease. However, due to the differences in the contrast mechanisms with respect to HRTEM, nanometre scale Al-rich regions reveal themselves as dark coloured regions. Furthermore, chemistry of these nano-regions were also analysed with energy dispersive X-ray spectroscopy (EDS) which is not given here.

HRTEM is widely used to reveal intriguing properties of metallic glasses. In their study, using HRTEM with certain image analysis techniques, Jiang and Atzmon had observed the nanocrystallization occurring in the shear bands,[63,64] a controversy that has been speculated through the years. Likewise, using C_s (i.e. spherical aberration) corrected HRTEM coupled with HRTEM simulation analysis, Hirata et al. had imaged the pseudo-crystalline, medium-range ordered structures in Pd-Ni-P bulk metallic glass via adjusting to a proper defocus value[65].

One of the crucial benfit of HRTEM is the "hidden" information inside the image that is the diffraction data.[66] A regular HRTEM image holds the direct space information, showing nothing but a "maze pattern"[67] with no distinct feature in metallic glasses. Further, it's well-known that diffraction data represents the atomic structure through reciprocal space, which relates to real space with Fourier transformation. Thus, with image analysis programs (such as Digital Micrograph™ or ImageJ), simply by making a Fast Fourier Transform (FFT) of a selected area from a HRTEM image, diffraction data could be obtained. An example is given in **Figure 1.13**: HRTEM image of an as-spun $Al_{90}Y_{10}$ metallic glass is given together with FFTs taken from two different regions of the micrograph. HRTEM image of the alloy is quite featureless, showing

the maze pattern. Also, FFT pattern of Region 1 is given in **Figure 1.13**.(b), which is quite similar to a diffraction pattern of a metallic glass. However, FFT pattern of Region 2 (**Figure 1.13**.(c)) reveals crystalline reflections of fcc-Al, which is not apparent in the HRTEM image. Hence, FFT analysis of a HRTEM micrograph is quite useful for diffraction studies as area of investigation for FFT is few nanometre squares, which cannot be attained with SAED.

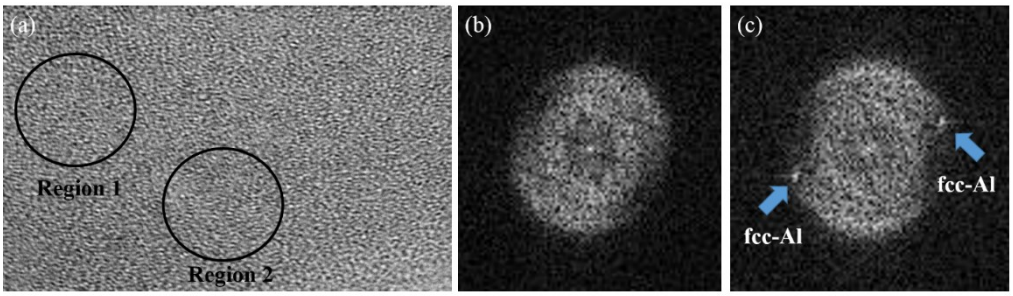

Figure 1.13: HRTEM micrograph of as-spun $Al_{90}Y_{10}$ metallic glass (a), and FFT patterns of selected regions in (b) and (c), respectively.

1.3.3 Fluctuation Microscopy

Fluctuation microscopy is a joint imaging and diffraction technique that detects higher order atomic correlations, i.e. medium-range order (MRO), in disordered systems via probing the variance in intensity of the scattered radiation.[66,68] Generally, from diffraction-based techniques (X-ray, neutron, electron), only pair correlations, i.e. two-body interactions in first coordination shell, can be extracted from total scattering factor function[69], which will be explained in detail in the forthcoming sections (Section 1.3.4.2). Conversely, fluctuation microscopy accounts for the scattering of higher order correlations, reaching three-body to four-body correlations.[70,71] Higher order correlations could also be explained as the higher order correlation between the short-range ordered (SRO) clusters, which is specifically called as MRO, and its known that the size of these quasi-ordered structures is known to be in the range of 0.5-3 nm.[67] A schematic explaining fluctuation microscopy is given in **Figure 1.14**.(a). The scattering from structurally incoherent sample (i.e. disordered) will be nearly the same, resulting in a constant variance. Whereas, if there exist structurally coherent domains

in the structure, scattering on both close and far proximity of the Bragg angle will cause a deviation from the scattering of structurally incoherent matrix, resulting in a detectable variance in the collected image and/or diffraction pattern. Hence, through a statistical analysis of the collected data over structurally coherent and incoherent domains will result in formation "the speckle pattern".

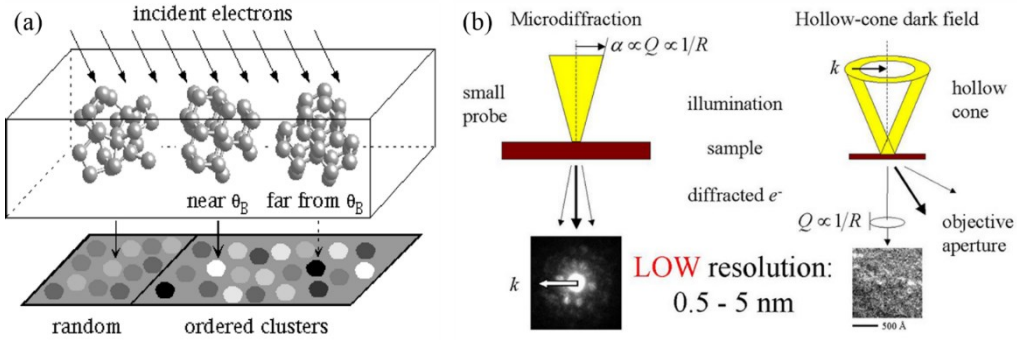

Figure 1.14: (a) Sketch of speckle pattern formation through random and coherent domains of a sample. **(b)** Representation of FEM techniques; microdiffraction and hollow-cone dark field [Retrieved from [68]].

Fluctuation microscopy technique was first devised by Treacy and Gibson in 1996 using TEM due to versatility of condensing the beam with various sizes, together with its ease of collecting image and/or diffraction data from nanometric volumes. Fluctuation electron microscopy (FEM) can be applied with two different, yet equivalent ways (**Figure 1.14**.(b)): it can be performed through collection of either hollow-cone dark field (DF) images, or microdiffraction patterns with using scanning transmission electron microscopy (STEM).[52,66,68,70,72] For both methods, after the normalization of intensity variance is done, speckle patterns will form revealing the degree of MRO possessed by the structure. The normalized variance, V(k), can be calculated with the following relation:

$$V(k,Q) = \frac{\langle I^2(r,k,Q)\rangle}{\langle I(r,k,Q)\rangle^2} - 1 \qquad \text{Equation 1.2}$$

where I is the intensity on the image with respect to position of the image, r, scattering vector, k, and resolution in reciprocal space, Q.

As a scattering technique, FEM is widely employed to track the structural differences in various amorphous materials and alloys. Treacy and Gibson[71] had shown the depression of V(k) signal with annealing in amorphous Ge, which was attributed to the decrease in the population of medium-range ordered clusters. In another study, Stratton et al.[73] had studied the effect of amorphization precursor on the structural differences in $Al_{92}Sm_8$ metallic glass. They had shown that for the melt-spun ribbons, the dominant MRO structure resembles fcc-Al, whereas in samples produced with a SSAR, the dominant MRO structure is Sm-centered icosahedra.

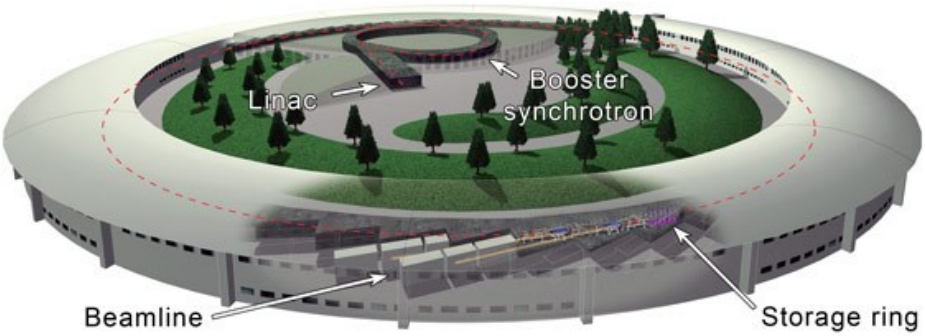

Figure 1.15: Schematic representation of European Synchrotron Radiation Facility in Grenoble, France [Image retrieved from [74]].

1.3.4 Synchrotron Light Source

Synchrotron light sources are state-of-art machines that enables scientist to perform experiments with powerful, high brilliance electromagnetic waves. Its vast usage are spans from basic sciences to life sciences and engineering; disciplines from physics and chemistry to archaeology, medical sciences to manufacturing and fabrication. The experiments are performed with a brilliant light called as “synchrotron radiation” which is produced with the following procedure: A pack of electron beam is ejected from an electron source, accelerated in a linear accelerator, and fed to the “booster ring”, a small cyclotron where the beam gains its designated energy and other beam characteristics, then fed to the large circular accelerator called the “storage ring”, in which it passes through auxiliary sections called bending magnets and insertion

devices (i.e. wigglers or undulators). A schematic of a synchrotron is given in **Figure 1.15**.

Synchrotron radiation production occurs in bending magnets and insertion devices via the electron bunches' interaction with them, as cycling electrons pass through these devices. The bending magnets are liquid He-cooled superconducting magnets; whose purpose is to bend the electron bunches' trajectory in order for electrons to cycle in the storage ring continuously (**Figure 1.16**.(a)). At the end of a straight section, as the electron bunch passes through a bending magnet, the exerted magnetic field by the magnet not only deflects the electron bunches, but also accelerates them, through which creation of a brilliant white radiation of electromagnetic waves is achieved[75–77]. Synchrotron radiation can also be obtained with insertion devices that are placed in the straight sections of the storage ring, namely wigglers and undulators. Insertion devices are large multipole magnets that force the passing through beam to oscillate at a very high frequency (**Figure 1.16**.(b)). During the electron beams' pass-by, each encountered pole change on the device act as a bending magnet, thus a coherent and high brilliance electromagnetic wave radiation is obtained. Albeit being both multipole devices, the difference between wigglers and undulators is the difference in deviation from its straight path of an electron bunch in each device. As passing through a wiggler, an electron bunch deviates higher than its natural opening angle, where in each deviation radiating electromagnetic waves[75,76]. Whereas, in an undulator, the deviation of the electron bunch is more gentle, causing overlapping of the radiated electromagnetic waves[75,76]. The major difference between two insertion device type is that due high interference of produced electromagnetic waves in undulators, the radiated light from it is much more brilliant and coherent, as compared to light produced from a wiggler. However, it should be noted that the radiation obtained from any insertion device is much higher in brilliance compared to light emitted from a bending magnet.

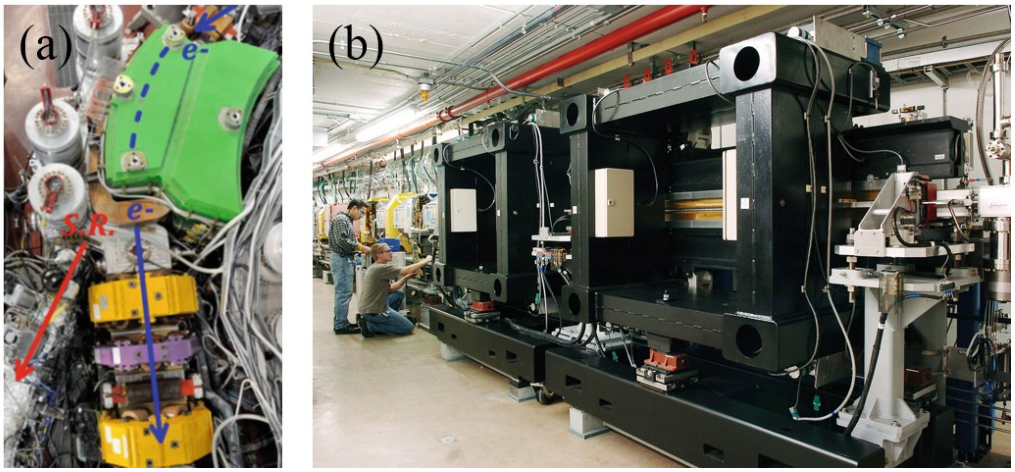

Figure 1.16: (a) Photograph of a bending magnet. The colored guides show the trajectories of the electron bunch (in blue) and the radiated light (in red)[76]. **(b)** A canted undulator that is being used in Advance Photon Source, USA[78].

The term brilliance should not be confused with the term brightness. Brilliance is defined as number of photons per time interval, per divergence angle, per 0.1% bandwidth of the average frequency and per cross-sectional area[75–77]. Brilliance is one of the most important parameters for a synchrotron, as it is the key parameter that defines the photon flux hits on the sample. Meaning that a light with high brilliance explains that the light has high flux with low divergence and low cross-sectional area. The brilliance comparison of the lightsources around the world, together with conventional X-ray generators is given in **Figure 1.17**.

The brilliant light generated from a storage ring is directed to beamlines for experimental usage. In a beamline, the brilliant white light first encounters the optical hutch of the beamline, where its diagnostics such as focusing, divergence and collimation is taken care of, then reaches to the experimental hutch of the beamline. The experimental techniques that are performed in a synchrotron can be categorized into three main branches; namely, scattering experiments (such as diffraction, inelastic scattering, photoelectron emission), imaging experiments (such as tomography, X-ray microscopy) and fabrication experiments (lithography, etc.). From an experimentalist's perspective, synchrotrons enable scientists to perform scattering

experiments with light having brilliances five-to-six orders of magnitude higher than laboratory scale X-ray generators.

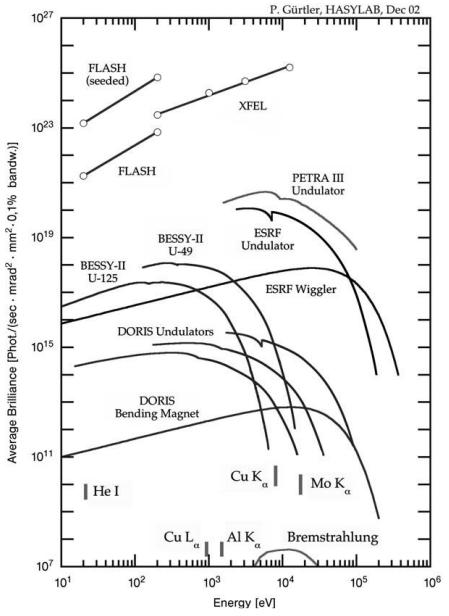

Figure 1.17: Brilliance comparison of some of the modern X-ray generators[79].

Most of the beamlines encourage users to perform *in situ* experiments; i.e. performing scattering experiments under the influence of thermal, mechanical, etc. forces. Typical example for an *in situ* experimentation is the *in situ* HEXRD experiments; i.e. collection of high energy diffraction patterns of materials whilst heating or cooling to probe the structural changes kinetically that are taking place in a phase transformation. HEXRD with *in situ* heating is widely used in metallic glass research, as one can quantitatively observe the structural changes taking place with high precision with respect to temperature; few examples regarding metallic glasses are given as follows. Antonowicz had showed that binary Al-RE alloy are showing a nano-scale phase separation prior to initial fcc-Al nanocrystallization in isothermal heating with combining *in situ* small angle X-ray scattering and wide angle X-ray scattering experiments (SAXS/WAXS)[80]. Whereas, Ronto et al. had shown that varying the solute chemistry leads to variation in initial devitrification products in $Al_{87}Ni_7RE_6$ alloys by *in situ* HEXRD[81]. Kalay et al. had studied the devitrification kinetics in $Al_{90}Sm_{10}$ alloy with HEXRD by *in situ* heating and had proved the nucleation followed

by growth is the dominant mechanism in primary fcc-Al nanocrystallization[82]. HEXRD experiments can also be under the influence of harsh mechanical forces. Sheng et al. had discovered that $Ce_{55}Al_{45}$ goes through polyamorphous phase transition with applied pressure via high pressure *in situ* HEXRD in a diamond anvil cell[83]. Eckert and Bednarcik et al.[84–86] had studied various metallic glass compositions with simultaneous tensile testing and HEXRD in order to investigate the structure-deformation relationship through *in situ* testing. Furthermore, scattering experiments can also be done *in operando* conditions, a widely used technique for structural investigations of battery materials in charge-discharge cycles[87].

1.3.4.1. Total Structure Factor

Throughout the years, synchrotron lightsources have become one of the essential tool for metallic glass research, due their high brilliance and state-of-the-art experimentation capabilities. One of the main usage of synchrotron radiation is the acquirement of total structure factor, S(Q), and calculation of pair distribution function (PDF), g(r), of materials with HEXRD technique for structural investigations. The experiments for obtaining total structure factor are generally called as total scattering experiments[69].

In a total scattering through an X-ray diffraction experiment, the acquired pattern reflects the material of concern's scattering behavior in terms of magnitude of wavevector, Q, versus intensity at the corresponding wavevector. The measured intensity at each wavevector, however, does not consist of solely the coherently scattered elastic light, rather additional scattering, i.e. Compton scattering, scattering signal from the background and ambient, and sample related contributions often mix with coherently scattered elastic light. These sample related parasitic signals can be presented as multiple scattering, thermal scattering, anomalous scattering and self-absorption[69,88,89]. Thus, in order to extract the purely structural scattering, corrections should be made to exclude the effects of stated parasitic contributors. Once corrections are done, total structure factor of the material can be obtained with the following equation:

$$S(Q) = \frac{I_c(Q) - \langle f(Q)^2 \rangle + \langle f(Q) \rangle^2}{\langle f(Q) \rangle^2}, \qquad \text{Equation 1.3}$$

where I_c stands for coherently scattered X-ray intensity and f(Q) stands for atomic scattering factor. In this study, mentioned corrections and calculations were done with pdfgetX3 software[88].

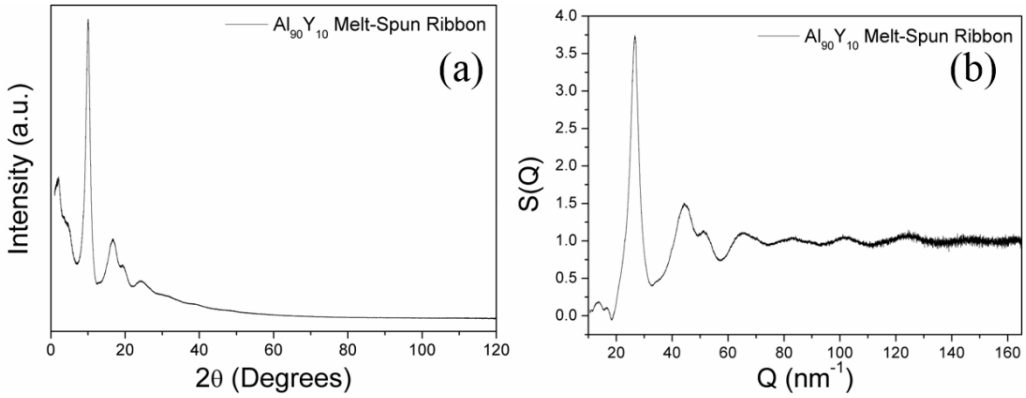

Figure 1.18: (a) Raw total scattering experiment data and **(b)** corresponding calculated structure factor of melt-spun $Al_{90}Y_{10}$ metallic glass.

Figure 1.18 shows the acquired diffraction pattern, obtained in ALBA synchrotron lightsource's MSPD beamline, and calculated structure factor versus wavevector of a melt-spun $Al_{90}Y_{10}$ metallic glass. In order to get the total X-ray structure factor of melt-spun $Al_{90}Y_{10}$ metallic glass, raw data given in **Figure 1.18**.(a) and diffraction pattern collected from the sample container were used as input in the pdfgetX3 software. Then, after adjusting the Q-range of the input, the software computes the mentioned parasitic scattering features and hence the total X-ray structure factor of the sample (**Figure 1.18**.(b)) was obtained as the output.

1.3.4.2. Pair Distribution Function

Pair distribution function (PDF), g(r), is a spatial distribution function that represents atomic pair-pair distances in a form of a histogram[69,90,91]. In other words, g(r) is "…like a distance map of the inside..." of the atomic structures in materials, as Egami and Billinge states[69]. PDF of a material can be derived from the total structure factor of the sample of concern with the following relation:

$$g(r) = 1 + \frac{1}{2\pi^2 r\rho_0}\int_0^\infty Q[S(Q) - 1]\sin(Qr)dQ, \quad \text{Equation 1.4}$$

where r is the distance operator, ρ_0 is the density of the material, Q is the wavevector ($Q = \frac{4\pi \sin\theta}{\lambda}$) and S(Q) is the total structure factor function. As the form of the above equation implies, PDF of a material can be derived by taking Fourier transform of the total structure factor (thus I(Q) in corrected form). The power of PDF relies on the fact that just by acquisition and correction of an X-ray diffraction pattern, one can obtain information about atom-to-atom correlations present in the structure.

Figure 1.19 shows experimentally derived PDFs of pure metallic fcc-Platinum and melt-spun $Al_{90}Y_{10}$ metallic glass. As being an atomic-correlation tool, PDF of crystalline Pt and amorphous Al-Y alloy clearly shows the structural differences, by means of atomic separation distance distributions. PDF of pure fcc-Pt shows sharp peaks at well-defined positions; as species in crystals have well-defined coordination numbers with well-established bond lengths, dictated both by thermodynamics and electronic interactions. Conversely, the given PDF of $Al_{90}Y_{10}$ metallic glass in Figure 1.19.(b) shows less intense broad peaks at ill-defined distances. The reason behind metallic glass have such an atomic distribution is that, crudely, metallic glasses have highly disordered structure with quite large free volume. Further, glassy structure cannot be defined with strict bond lengths and coordination numbers, rather, these quantities show certain kind of distribution among all constituent atoms in the structure. Hence, PDF of an amorphous material is representing this mentioned spatial distribution with respect to distance.

PDF analysis is also a powerful technique for characterization of SRO in both crystalline[69,90,91] and amorphous materials[69,91,92]. For the crystalline case, defects such as vacancies at certain atomic positions, anti-phase domains, and other point and linear defects can be inferred from the peak intensities and positions of the PDF of the crystalline material of concern. For the amorphous materials, PDF analysis reveals powerful information about the chemical and topological information about the first coordination shell (SRO) environment, albeit showing very little or no valuable information about higher order coordination, namely MRO. This fact is actually a

result of the input of the derived PDF that is total scattering experiments with X-rays and/or neutrons. As discussed previously on Section 1.3.3, diffraction of X-rays, neutrons or electrons generally occur through two-body correlations in the first coordination shell, meaning that elastic scattering of waves from materials (regardless of the inherent degree of order) arise from SRO environment in the structure. Thus, if one considers the structural aspect of MRO, that is three to four-body correlated atomic structures, diffraction experiments, hence, PDF analyses is quite "blind" to the distinct structural features in the MRO-scale. Experimental limitations on PDF calculation and its effect on resolving structures will be given in the forthcoming sub-section.

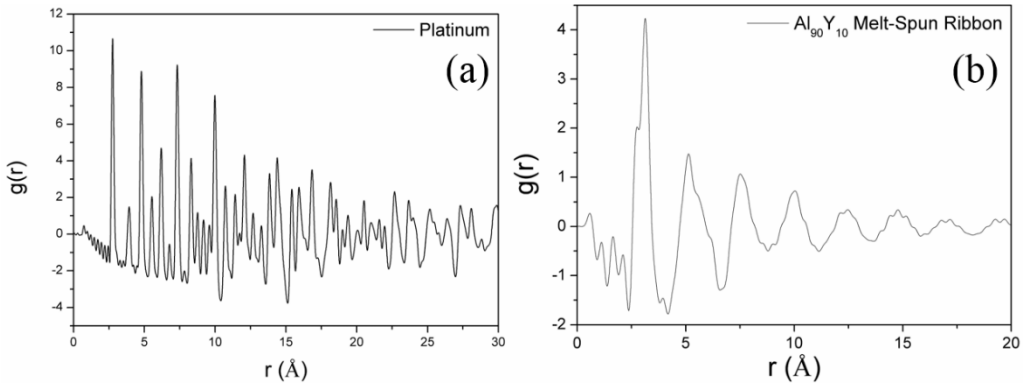

Figure 1.19: Pair distribution functions derived from total scattering experiments of **(a)** pure crystalline metallic Platinum[88] and **(b)** melt-spun amorphous $Al_{90}Y_{10}$ metallic glass.

Another disadvantage of PDF analysis on MRO characterization is that structural features that are manifested as medium-range ordered structures are said to form three dimensional networks[67,93–95]; whereas PDF data derived from total scattering experiments displays the structural features in one dimension. Although there are computational publications making use of PDF analysis for commenting on the high order solute-solute and solute-solvent correlations in the structure[96–98], to our best knowledge there is no experimental study with PDF analysis directly resolving and commenting precisely on the MRO structures in metallic glasses and other amorphous systems.

1.3.4.3. Effect of Experimental Parameters on Pair Distribution Function Calculation

As being a powerful tool for structural studies, recently PDF analysis has become one of the essential tools for materials scientists and crystallographers. Nevertheless, conducting a PDF analysis has its own perks and losses, in both mathematical and experimental means. Most of the experimental parameters that affect PDF calculation of materials will be discussed by referencing to **Figure 1.20**. The given figure has total X-ray structure factors and correspondingly derived PDFs of melt-spun $Al_{90}Tb_{10}$ metallic glass sample collected from three different lightsources, namely BL04-MSPD beamline of Alba Synchrotron Lightsource, MCX beamline of Elettra Synchrotron Lightsource, and a conventional laboratory diffractometer, Rigaku Ultima IV employing a Cu anode. Wavelength used in each total scattering experiment is indicated in **Figure 1.20**.(a). It should be stated that most of the experimental parameters in each total scattering experiment is quite different; available Q-range, brilliance of the lightsource, used detectors, etc. However, though the given results in **Figure 1.20** comprise the combined effect of mentioned experimental parameters, it is still safe to say that individual discussion of these effects is still possible. The total scattering experiments in Alba and Elettra Synchrotron Lightsource were done in the scoop of studies regarding the presented thesis.

Firstly, as being a Fourier transform, it is known that the resolution of a calculated PDF is directly proportional with the extent of the Q-range (i.e. the wavevector interval) of the acquired structure factor[69,90,91]. This is actually a combined effect exerted on the calculation by both the angular limit that can be scanned and the used wavelength, given that Q depends both on scattering angle and wavelength. As it can be seen from **Figure 1.20**.(a), the attained Q-ranges differ largely with the wavelength used; and also the reflection (Bragg-Brentano) geometry in conventional diffractometer hindered the scanning of high angles, with respect to 4-circle Huber diffractometers in synchrotron beamlines. As it can be seen in **Figure 1.20**.(b), owing to its large Q-range, PDF derived from acquired structure factor from Alba reveals atomic distributions quite nicely, whereas, PDF derived from the conventional

diffractometer resolves only the coordination shells without any intricate signal. Furthermore, the most important effect of Q-range on the resolution of PDF is the presence of termination ripples. As stated before, PDF is the Fourier transform of the structure factor function; meaning that the range that Fourier transformation integral is taken should have evident tracks on the PDF. As a total structure factor should have a finite Q-range limit due experimentation limitations, the limitation of exerted by the Q-range reveals itself mostly by creating extra/virtual ripples on the low r-region of the g(r). In the low r-region, g(r) curve should have no peak-kind of features, as there should be no atoms up until the thermodynamically defined bond length. Thus, if the total structure factor function is acquired in a narrow Q-range, due to the nature of the Fourier transformations, certain ripples can become apparent in the low-r region, thus creating the termination ripples. Hence, for a PDF to represent the structure of a material with highest precision and accuracy, the total structure factor that is used for PDF derivation should have highest possible attainable Q-range.

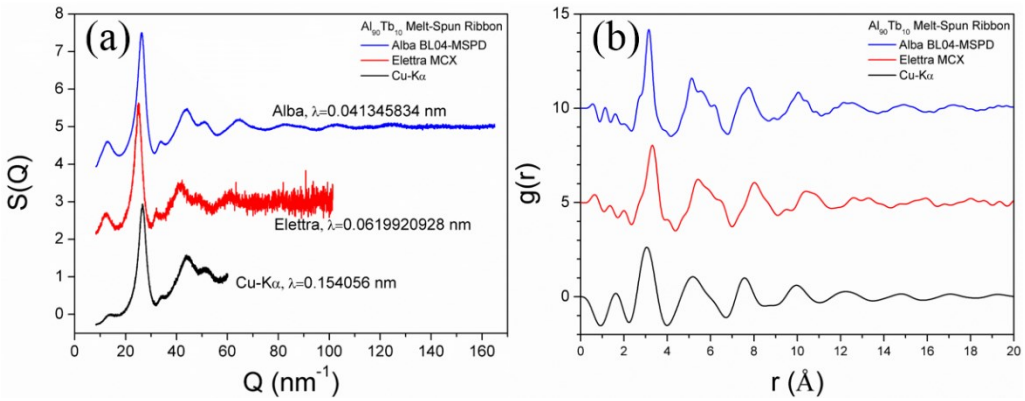

Figure 1.20: (a) Total X-ray structure factors and **(b)** correspondingly derived PDFs of melt-spun $Al_{90}Tb_{10}$ metallic glass with data collected with Alba and Elettra synchrotron lightsources, and a conventional diffractometer.

Brilliance (or, implicitly the flux on the sample) and detector selection are another limiting experimental conditions that affect the structure-resolving capability of a PDF calculation. Using a more brilliant light will increase the beam flux that is passing through a certain cross section on the material. Similarly, usage of fast detectors will also enable users to collect data more rapidly. As for the investigations of low

scattering materials, such as amorphous alloys with micrometres of thickness, these parameters exert a temporal constraint on the collection of total structure factor. Technically, a high quality PDF should also be calculated from a conventional diffractometer, with using a low-λ anode as silver and using a 2D plate detector. However, making such a total scattering experiment should take relatively long periods (severals days to weeks) in order to have decent Q resolution. Similarly, total scattering experiments on amorphous $Al_{90}Tb_{10}$ melt-spun ribbons in MCX beamline of Elettra Synchrotron Lightsource had taken around 8-10 hours of acquisition time with a 0D scintillator point detector and beam flux of 10^{11} ph/sec on 300x300 μm^2 cross section. Conversely, total scattering experiments of the same alloy in BL04-MSPD beamline of Alba Synchrotron Lightsource had taken around 40 minutes to 1 hour, in which 1D Mythen array detector was used with a beam flux of $4x10^{12}$ ph/sec on 15x15 μm^2 cross section. When one compares the wavelength and brilliance difference in the two total scattering experiment of an identical sample, and also compare the quality of the obtained PDFs, one can clearly understand the effect of brilliance and detector selection on the quality and precision of the total X-ray structure factor, hence on the PDF analysis.

1.3.5 Reverse Monte Carlo Method

As being an atomic simulation method, Reverse Monte Carlo (RMC) modelling is a widely used and celebrated technique by disordered materials community and it is being employed to derive three dimensional atomic configurations by fitting to experimental data[67,99,100]. Unlike molecular dynamics (MD) related methods which use interatomic potentials for calculating the structure of a system, RMC utilizes the experimental constraints, such as total X-ray or neutron structure factors, partial pair distribution functions, XANES and EXAFS signals, and also measured density of the sample and bond lengths between each atomic constituent pair.

To start a RMC model refinement, one should first introduce the required constraints properly. These constraints are not limited to experimental data such as high quality total structure factor data. Other than experimental datum or data, the basic constraints

required by the RMC are density of the sample (in number of atoms per volume format, i.e. in atoms/Å^3 unit), minimum bond lengths of each species (A-A, A-B and B-B bond lengths for a binary A and B system).

When the mentioned constraints are established to the system, RMC modelling of the system is performed iteratively with the following calculation scheme[99]: the software first calculates the element specific partial pair distribution functions of each atomic interaction in the provided simulation box. Then, the calculated partial PDFs are transformed to partial structure factors for each atomic interaction. Calculated partial structure factors are summed with properly used atomic scattering factors with their Q dependence (or for neutron case, scattering lengths instead of atomic scattering factors). The difference between the supplied experimental total structure factor and the calculated total structure factor of the initial configuration is calculated with the following formula:

$$\chi_o^2 = \sum_{i=1}^{m} \frac{\left[S^{configuration}(Q_i) - S^{experimental}(Q_i)\right]^2}{\sigma^2(Q_i)}, \qquad \text{Equation 1.5}$$

where summation is done over each data point from i to m, S denote the structure factors and σ is the provided confidence interval. Then, a randomly selected atom is moved, considering the provided minimum separation distances, and the difference between the supplied experimental total structure factor and the calculated total structure factor of the initial configuration is calculated with the following formula:

$$\chi_n^2 = \sum_{i=1}^{m} \frac{\left[S^{configuration-new}(Q_i) - S^{experimental}(Q_i)\right]^2}{\sigma^2(Q_i)}. \qquad \text{Equation 1.6}$$

If the calculated difference after the movement of the atom is smaller than the calculated difference before the movement, the movement is accepted and the new configuration becomes the initial configuration. If the above statement is not satisfied, the new configuration is accepted with a probability of $\exp(-\frac{(\chi_n^2 - \chi_o^2)}{2})$, otherwise the move is rejected. The explained iteration procedure is repeated for each iteration step until the calculation difference saturates at a certain value, at which the difference between the experimental data and the obtained structure is minimized.

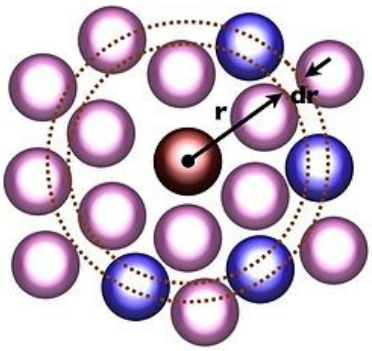

Figure 1.21: Schematic representation of discretization of space for partial PDF calculation[101].

One thing that must be mentioned is that RMC always tend to force the structure to maximum entropy to minimize the energy[99,100]. From structural analyses of amorphous materials point of view, this is actually an advantageous. When one oversees all other constraints and investigates the RMC calculated 3D simulation box of an amorphous material, and find manifestations of higher order correlations than short-range ordering (i.e. MRO), one cannot oversee his or her findings as calculation errors; rather as RMC pushes the system to maximum entropy, findings of higher order correlations should reflect a more extensive ordering in the actual sample, with respect to the RMC calculated model.

The analysis of RMC models having an amorphous structure is not straight forward compared to a crystalline structure, as amorphous materials lack long-range ordering (LRO), with well-defined unit cells. Thus, the simulated amorphous structures are analysed with calculation of partial pair distribution functions (partial PDFs), Voronoi Tessellation and bond angle distribution analysis.

Similar to previously explained pair distribution function, partial pair distribution function represents the spatial relationship of species in an element specific fashion. Meaning that rather than showing the distance distribution of every atomic specie, partial PDF gives the distance relation for the chosen specie only. Partial PDF can be further explained with the following example: for a binary alloy of A and B, there exists three partial PDFs which are pair correlation between A and A atoms, A and B

atoms and B and B atoms. As partial PDF of A-B pair correlation shows the spatial distribution by choosing an A atom and count the B atoms surrounding this A atom throughout the structure. This feature of partial PDFs is quite useful for analysing the solute-solute, solute-solvent and solvent-solvent interactions in alloys, as it represents the distance relationship with chemical sensitivity, which an ordinary PDF lacks. For a calculated simulation box, partial PDF calculation is performed not through Fourier transformation of the partial structure factors. Rather, due the 3D atomic configuration comprises the coordinates of each atom in the structure, it is calculated with the following formula:

$$dn_{\alpha\beta}(r) = \frac{N_\alpha}{V} g_{\alpha\beta}(r) 4\pi r^2 dr, \qquad \text{Equation 1.7}$$

where $dn_{\alpha\beta}(r)$ is the number of atoms located in the r+dr distance, N_α is the total number of atoms of the α species in the system. Partial PDF calculation is schematically represented in **Figure 1.21**.

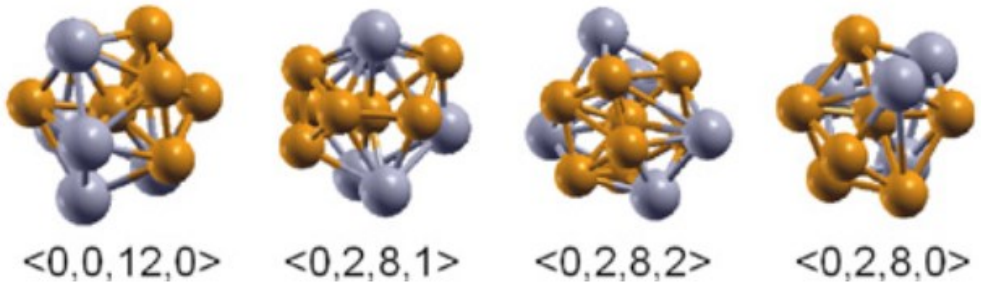

Figure 1.22: Schematic representation regular and distorted icosahedral clusters and their respective Voronoi indices that are present in CuZr metallic glasses[67].

Voronoi Tessellation is one the most widely used methods for analysing simulated structures. Such a tessellation is done by drawing a plane in the centre of the lines that connects the central atom to the atoms in the first neighbourhood. The volume enclosed by the drawn planes form a polyhedron called Voronoi polyhedron, which is analogous to Wigner-Seitz cell of a crystal[67]. Such polyhedra is represented with Voronoi index with a five number vector, $<i_3, i_4, i_5, i_6, i_7>$, where i_3 represents the number of triangular faces, i_4 represents the number of square faces, i_5 represents the number of pentagonal

faces, i_6 represents the number of hexagonal faces, and i_7 represents the number of heptagonal faces. The power of Voronoi Tessellation is that it unveils the topological structure and local symmetry of an atom in its first coordination shell. Furthermore, Voronoi technique also enables direct calculation of coordination numbers for each atom, without any further definition. Schematic representation of several SRO units with regular and distorted icosahedral symmetry is given in **Figure 1.22**[67].

Bond angle distribution analysis is also an important tool for investigation of local topological structures of atomic species in a simulation box. Likewise, as Voronoi Tessellation, bond angles on the first coordination shell is computed by the calculation of angular separation of the lines that connects the central atom to the atoms in the first neighbourhood. It should be mentioned that bond angle distribution is also presented in element specific fashion; meaning that in a binary A-B alloy, bond angles are computed and presented as A-A-A, A-B-A, B-A-A, B-A-B, A-B-B, B-B-B triplets.

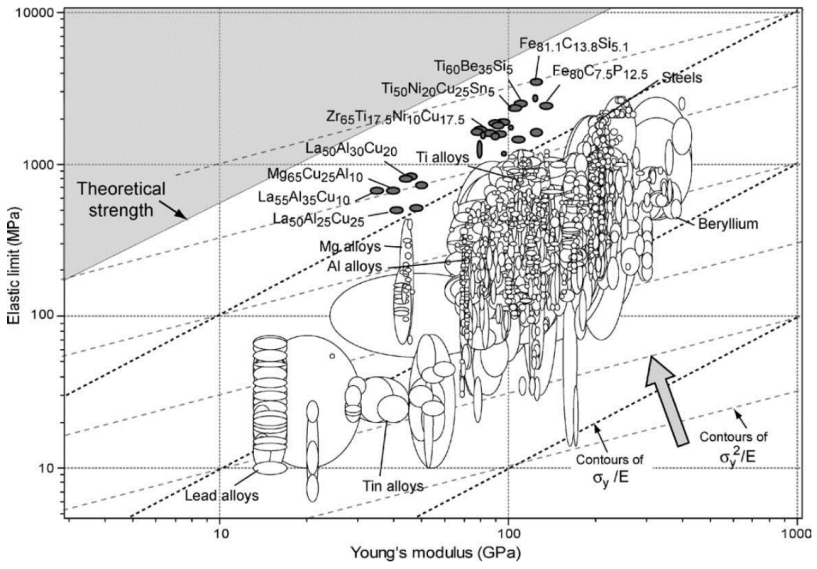

Figure 1.23: Elastic limit versus elastic modulus assessment plot for metals and alloys. Black and grey contours show the yield strain and resilience, respectively[102].

1.3.6 Conclusion and Thesis Organization

Metallic glasses, in amorphous structure and in partially devitrified state, together with their amorphous/nanocrystalline composite structures comprise a promising class of

new structural materials. An assessment of mechanical properties considering 1507 different metals and metallic alloy systems was made by Ashby and Greer and given in **Figure 1.23**[[102]]. As it can be clearly observed from the given figure, metallic glass compositions are showing superior mechanical properties as compared to crystalline counterparts. Hence, with resolving the soft-spot of critical casting diameter restriction this high strength and tough class of materials, metallic glasses could be the structural materials of the days to come.

The aim of this thesis is to study the structural aspects of metallic glasses through experimental and computational methods and projections from these findings were used to increase the size limitation and the mechanical properties of Al-based metallic glasses. The present chapter had given a comprehensive literature review on the historical aspects of metallic glasses, the glass formation phenomenon by considering various production techniques' –both thermodynamics and kinetics-wise–, and key characterization techniques that were used in the current study and also being used by the metallic glass research community. The second chapter concentrates on the structure of Al-based metallic glasses, mainly on $Al_{90}Tb_{10}$ marginal glass forming alloy. This chapter focuses on the structural investigation of $Al_{90}Tb_{10}$ melt-spun ribbons and sputtered thin films through HEXRD investigation with total scattering experiments and RMC modelling. Structural explanations were stated in the light of previous observations of change in phase selection hierarchy, observed by Yıldırım and Kalay[103]. Third chapter deals with production of amorphous/nanocrystalline composite powders by means of SSAR techniques, characterization of produced powders and their consolidation behavior. Studies regarding the effect of ex-situ composite formation of produced amorphous/nanocrystalline powders and micrometer sized pure Al powders on mechanical properties of bulk consolidates were also given in this chapter. The conclusions of the complete study along with and future recommendations were given and stated in the final chapter.

CHAPTER 2

SHORT-TO-MEDIUM-RANGE CORRELATIONS IN Al-RE METALLIC GLASSES

2.1 Abstract

The amorphous structure of $Al_{90}Tb_{10}$ metallic glasses produced by Cu-block melt-spinning and magnetron sputtering were investigated by a combined study of synchrotron X-ray diffraction, reverse Monte Carlo calculations and fluctuation electron microscopy. The total X-ray structure factors and pair distribution functions for both alloys were calculated and investigated in detail. Topological calculations on RMC models have shown that as-spun and as-sputtered glasses at the same composition have similar ordering in short-range scale. Fluctuation microscopy have revealed the structural differences in medium-range scale that were attributed to be the reason behind the previously reported devitrification path change. Structural variations in SRO and MRO scales were discussed in the light of *Efficient Cluster Packing* model.

2.2 Introduction

From their discovery 56 years ago by Duwez et. al[1], metallic glasses have been attracting much attention due their outstanding materials properties, making them promising candidate for vast engineering applications. Through the years, though many advancements have been achieved, a complete understanding of its structure is

still lacking, hindering optimization of their performance via any structural tailoring. The amorphous structure is known not to be completely random, yet have extensive chemical[67,104] and topological[104,105] ordering on short-range (SRO) and medium-range (MRO), as well. SRO is generally defined as the chemical and topological environment in constituent atoms' first coordination shell[104]. Analyses-wise, first coordination shell of any constituent atom is defined for a certain cut-off distance from the central atom of concern that is generally taken as first minima in its partial pair distribution function (PDF), a value generally less than 0.5 nm[36]. SRO structures in metallic glasses and their respective liquid states have still been debated, and several theories have been developed. In his seminal paper, Frank have proposed that metallic liquids should have icosahedral ordering in order to frustrate the transformation tendency into crystalline species[106]. Later, Bernal have proposed the concept of dense random packing (DRP) of atoms, treating them as hard spheres, and explained the structure as a constitution of regular Platonic polyhedra[107] that act as building blocks in three dimensions. Further, Gaskell have proposed a stereochemical model, saying structure of glasses consists of a cluster scheme with a specific cluster geometry, and chemistry[108,109]. The model states that the chemistry, topology and connectivity behavior of the clusters in liquids and amorphous solids are nearly identical with the crystalline species of the same composition[110]. Among all of the mentioned theories of SRO in metallic glasses and liquids, only Frank's hypothesis was fully proved to be true for both mono and multicomponent metallic liquids and glasses, both experimentally[111–114] and computationally[11,115,116]. DRP model is verified only for monoatomic liquids and alloy melts with insignificant chemical ordering[67]. The reason that DRP fails to explain the glassy structure is as its name implies, DRP model treats atoms as *"rigid and hard spheres"* meaning the distance between two bonded atoms can be calculated by summation of their corresponding atomic radii. This was found not to be true, as experimental evidence has showed significant bond shortening in glasses, implying deviations from true metallic bonding[67,117,118]. Though it was turned out to be valid for certain the metal-metalloid glasses, the stereochemical model is not fully explaining the glass structures; since the structure of glasses are not dominated by a single cluster geometry with certain bond lengths and coordination, rather clusters show a diverse

topology with respect to both chemical species and composition[13,119–121]. Besides, studies have showed that the dominant cluster topology and chemistry in glass and crystal of the same composition should not necessarily be the same[67].

SRO structures were found to form extended ordering without creating any long-range translational nor rotational order, namely medium-range ordering (MRO). MRO has been admitted to have general length scale of 0.5-3 nm[67,122]. The extension of SRO clusters into MRO structure occurs through connection of cluster vertices, edges, faces and also with interpenetration of two adjacent clusters[96,123,124]. Medium-range ordering is not a unique feature of the metallic amorphous systems. Experimental and computational studies have revealed that MRO structures are present in ionic[94,125], covalent[93,126] and chalcogenide[127,128] glasses. Moreover, experimental[117,129–131] and theoretical[11,96,97,132,133] studies have revealed that short-to-medium-range correlations also exist in the molten states of the materials as well, even in the non-glass forming melts[134,135]. The current structural explanation of MRO was established by Miracle[123,136,137] and coworkers[118,138–141] by taking DRP model's solute centered clusters as the local representative unit and constituting them in a densely packed topology with inherent free volume. The efficient cluster packing (ECP) model dictates that there exists a populous cluster with a certain coordination number, a quantity found by the radii ratio of solvent to solute atom ($R=R_{solute}/R_{solvent}$)[137,141]. Through this simple quantity of radii ratio, the model and its extensions can predict certain structural properties, namely coordination number around solute, minimum solute content(s) for amorphization[141], partial coordination numbers of constituents[138], packing efficiency, density, solute separation distance[123] and minimum angular separation of solute atoms[139]. The model also predicts the "interstices" that minor solvent atoms can occupy, without breaking down the efficient packing. As being a purely geometrical approach, efficient cluster packing model is in excellent agreement with the experimental studies of structural features for both solute-lean and solute-rich glasses of various sizes of solutes[123,137].

Structural investigation of metallic glasses via experimentation is mainly being done through total scattering experiments with X-rays[115,131,142], neutrons[143–145] and

electrons[146–148]. Through analysis of elastic scattering from different sources of radiation, total structure factors (S(Q)) and pair distribution functions (PDF) can be calculated. S(Q) and PDF are essential tools for structural investigations and contain valuable information about chemical and topological structural features[69]. Aluminum-based metallic glasses, specifically rare-earth (RE) containing constitutions are suitable choice for study the metallic glass structure as the diffraction patterns of these alloys contain extra reflections, namely pre-peak and the side peak (see Fig. 1), accompanying the amorphous scattering peaks[21,67]. In our previous studies on Al-RE glasses, the origin of the pre-peak is found to stem from the RE-RE scattering via RMC calculated partial structure factors[95,129]. As the X-ray form factors of RE are quite large with respect to the Al solvent, the extended ordering of the RE clusters tend to cause extra reflections on the scattering intensity[95,129,149]. Previous experimental[73,95,150,151] and theoretical[96,129,152,153] analysis of binary Al-RE glasses have shown that solute (RE) centered clusters tend to form network-like structures, leaving out non-crystalline pure Al regions. The presence of pure Al regions was also confirmed by 3D atom probe tomography (APT) both in the as-quenched state[95] and on annealing prior to primary crystallization[154]. Furthermore, observations of pre-peak in the Al-RE melts in both MD calculations[96] and experiments[129,132,155] also show that ordering of RE atoms tend to take place well above the liquidus temperature, as well. Thus it is evident that chemical and topological ordering of SRO clusters in the medium-range land scale is an important factor and easy-to-probe feature in binary Al-RE metallic glasses.

In a recent study, we have shown the alteration of crystallization path for $Al_{90}Tb_{10}$ metallic glasses produced with melt-spinning and DC magnetron sputtering[156]. The sputtered thin film has by-passed the second crystallization step of melt-spun ribbon's devitrification sequence, and continued with the third reaction of the melt-spun ribbon. Moreover, sputtered thin films were also showed a nano-scale phase separation before initial devitrification step, which is confirmed by thermal analysis and microscopic examinations. The size and number density of the initial devitrification product, nanocrystalline fcc-Al phase, is also showed discrepancies with changing production route.

In this study, we analyze the amorphous structure of melt-spun ribbons and sputtered thin films through high energy X-ray diffraction (HEXRD), reverse Monte Carlo (RMC) simulations and fluctuation electron microscopy (FEM). Diffraction patterns obtained via HEXRD is used to calculate experimental total X-ray structure factors and experimental pair distribution functions, which are used as constraints for RMC simulations. RMC simulations are investigated topologically with Voronoi polyhedral and related bond-angle and coordination number analyses. FEM experiments was done for correlation with the RMC models and experimental observations of MRO. The devitrification sequence variation is explained via investigation of SRO and MRO structures of as-spun and as-sputtered $Al_{90}Tb_{10}$ metallic glasses.

2.3 Experimental Procedure

Ingots of $Al_{90}Tb_{10}$ were prepared using electric arc melting under Ar atmosphere from highly pure Al (99.99 wt.%) and Tb (99.9 wt.%) elements. Amorphous samples were produced by two different techniques. Amorphous ribbons having approximate thickness of 30 μm were prepared using a Cu block single melt-spinner at a tangential speed of 30 m/s. Amorphous thin films having approximate thickness of 10 μm were produced using liquid nitrogen cooled copper target cooled magnetron sputtering process. The complete amorphous phase for both samples were confirmed by XRD and transmission electron microscopy (TEM). Further, compositions of both samples were confirmed by microprobe analysis.

High energy X-ray diffraction (HEXRD) experiments were conducted at BL04-MSPD beamline of ALBA Synchrotron Light Source. Free-standing samples were attached to the goniometer with a 135^{o} inclination with respect to the incoming X-ray beam to prevent blockage of data collection on high Q-range ($Q = \frac{4\pi sin\theta}{\lambda}$ where θ is the Bragg's angle and λ is the wavelength of X-ray radiation). The data were collected in transmission flat plate geometry. A double Si monochromator was used to select the wavelength of 0.04134 nm. The data were collected on a Q-range of 2.7-263.2 nm^{-1} using Mythen array detector. The raw HEXRD data collected for amorphous melt-spun ribbon and magnetron sputtered thin film were corrected for background,

polarization, absorption, multiple, Compton scattering and then converted to the total structure factor function, S(Q) using the Equation 2.1:

$$S(Q) = 1 + \frac{I^c(Q) - \sum_{i=1}^{n} a_i |f_i(Q)|^2}{\left|\sum_{i=1}^{n} a_i f_i(Q)\right|^2}, \qquad \text{Equation 2.1}$$

where $I_C(Q)$ is the coherent scattering intensity normalized to a_i, atomic concentrations, and $f_i(Q)$ is the atomic scattering factors for each constituent atoms[69]. Pair distribution functions (PDF) for both as-spun and as-sputtered samples were calculated by taking the Fourier transformation of the calculated S(Q) by using Equation 2.2. Calculations and corrections were done using the PDFgetX3.1 software[88].

$$g(r) = 1 + \frac{1}{2\pi^2 r \rho_0} \int_0^\infty Q[S(Q) - 1] \sin(Qr) dQ. \qquad \text{Equation 2.2}$$

Reverse Monte Carlo (RMC) simulations were done using RMC++ simulation package[157] in order to represent the atomic configuration of the samples in real space dimension. In a cubic simulation box, 20,000 atoms were randomly distributed with the proper stoichiometry, density and nearest neighbor distances with periodic boundary conditions. Density of the $Al_{90}Tb_{10}$ melt-spun is measured with Archimedes' method. Because of the difficulties with the measuring the density of the thin film, it was taken from the room temperature value from ab-initio Molecular Dynamics (MD) simulations for the same composition[155]. The cut-off distances for the partial pairs for the first shell distances in the RMC calculations were chosen from direct Fourier transforms of experimental S(Q) and from the mentioned ab-initio MD calculations. For the simulation experiments, the difference between the measured S(Q) from HEXRD experiments and the calculated S(Q) from each RMC modeled configuration is determined by the following equation.

$$\chi_0^2 = \sum_{i=1}^{n} \frac{[S_0(Q_i) - S_0^c(Q_i)]^2}{\sigma(Q_i)^2}, \qquad \text{Equation 2.3}$$

where S_0 is the experimental and S_0^c is the calculated structure factor. Approximately 10^6 iterations were performed for a constant σ(Q) value of 0.002, to minimize the χ^2.

The local atomic structure of the system was investigated using Voronoi Tesellation analysis. The results were represented in terms of Voronoi indices such as < n_3, n_4, n_5, n_6, n_7 > in which n_i represents the number of i-edged faces of Voronoi polyhedra. In Voronoi analysis, each atom is represented by a Voronoi polyhedron. Each face consisting the polyhedron corresponds to a neighboring atom, and the edge number of the face shows the number of the common neighbors shared by the central atom and the neighboring atom. The coordination number of each atom was also calculated as the total number of faces of each polyhedron.

Fluctuation electron microscopy (FEM) experiments were performed using an aberration and probe corrected FEI Titan field emission scanning/transmission electron microscope. The change in variance was recorded from 1000 sample positions with a beam size of 2 nm. Specimens for FEM analyses were prepared using electropolishing with a solution of 25 vol.% nitric acid and 75 vol.% methanol at 241K.

2.4 Results and Discussion

Figure 1 shows the experimental total X-ray structure factors, S(Q), calculated from HEXRD patterns and the corresponding RMC fits for as-spun and as-sputtered $Al_{90}Tb_{10}$. In the experimental S(Q) of both as-spun and as-sputtered $Al_{90}Tb_{10}$, it can be clearly seen the extra reflections, pre-peak and side peak, along with the diffuse amorphous scattering peaks at wave momentums of ~13 nm^{-1} and ~33.9 nm^{-1} for melt-spun ribbon and ~12.9 nm^{-1} and ~33.8 nm^{-1} for sputtered thin film, respectively. As aforementioned above, the presence of these extra features are scattering manifestation of prominent Al-Tb interaction. The positions of pre and side peak is converted to real space distance using the equation $D = \frac{2\pi}{Q}$, and it was found that Al-Tb distances of sputtered thin film is found to be 2 pm expanded with respect to melt-spun ribbon. In addition to slight shift in the positions, Lorentzian fitting was performed on the extra reflections had revealed that both pre and side peaks are broader for sputtered thin film, with respect to melt-spun ribbon[156]. Previously, we attributed the broadening of the pre and side peaks to be the indications of a relative “disorder” in sputtered thin films with respect to melt-spun ribbons.

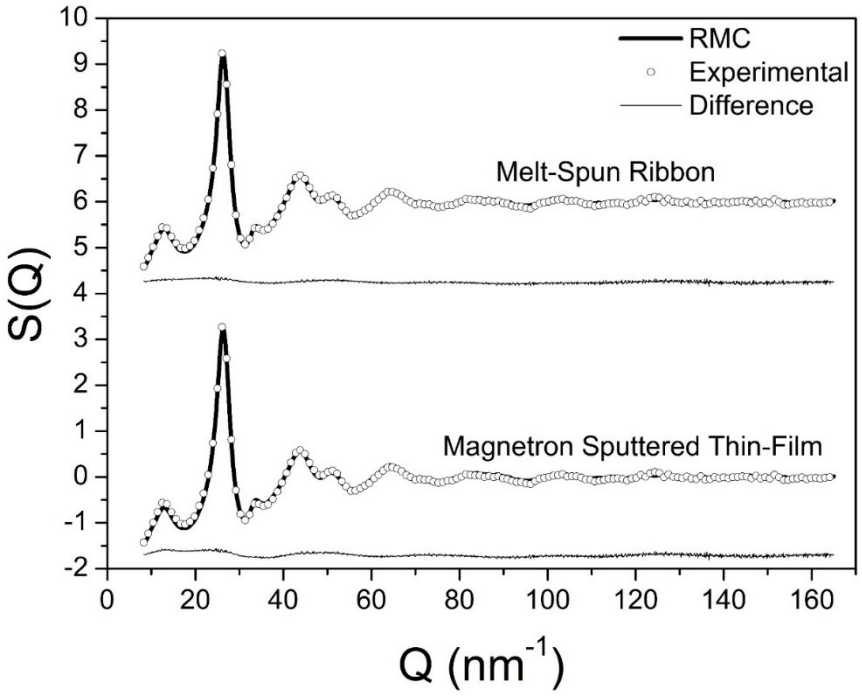

Figure 2.1: Experimentally measured (open circles) and RMC fitted (solid line) total structure factors of melt-spun ribbons and magnetron sputtered thin films of $Al_{90}Tb_{10}$.

Reverse Monte Carlo (RMC) is a simple, yet useful simulation technique that enables users to obtain partial pair-pair correlations for disordered systems by application of proper constraints[67,99,100]. Along with experimental S(Q), Figure 1 also shows the RMC fits of as-spun and as-sputtered $Al_{90}Tb_{10}$ metallic glass alloys. As the difference line implies, reasonable fits were obtained for both cases, including the extra scattering features in the low-Q region and the fluctuations in the high-Q region.

Pair distribution function (PDF) is an essential tool for structural inspection, containing exquisite information about the local environment of constituent atoms, namely bond lengths, coordination number, bond-orientation angles of pairs[69,90]. PDFs derived from HEXRD results for as-spun and as-sputtered $Al_{90}Tb_{10}$ are given in Fig. 2.2.(a). Estimated bond distances from Goldschmidt radii in elemental forms of Al and Tb are also indicated in the mentioned figure. It can be clearly seen that for the first coordination shell both glasses produced from two different synthesis routes have quite matching PDFs. However, examination of the first coordination shell together with

the bond distances estimated with elemental Goldschmidt radii have revealed that all bond pairs' distances, namely Al-Al, Al-Tb and Tb-Tb, have deviated from the estimated values. A similar phenomenon was previously seen in Zr-Cu(-Al) and Zr-Ni-Al alloys and attributed to the charge transfer between the metallic solute and solvent atoms[142,158]. It should be stated that such partial covalent behavior of atomic bonds was observed irrespective of the production route. Lastly, it was observed that the intensity of the peak located 3.9 Å, corresponding to Tb-Tb bonds, is slightly higher for the sputtered thin film with respect to melt-spun ribbons.

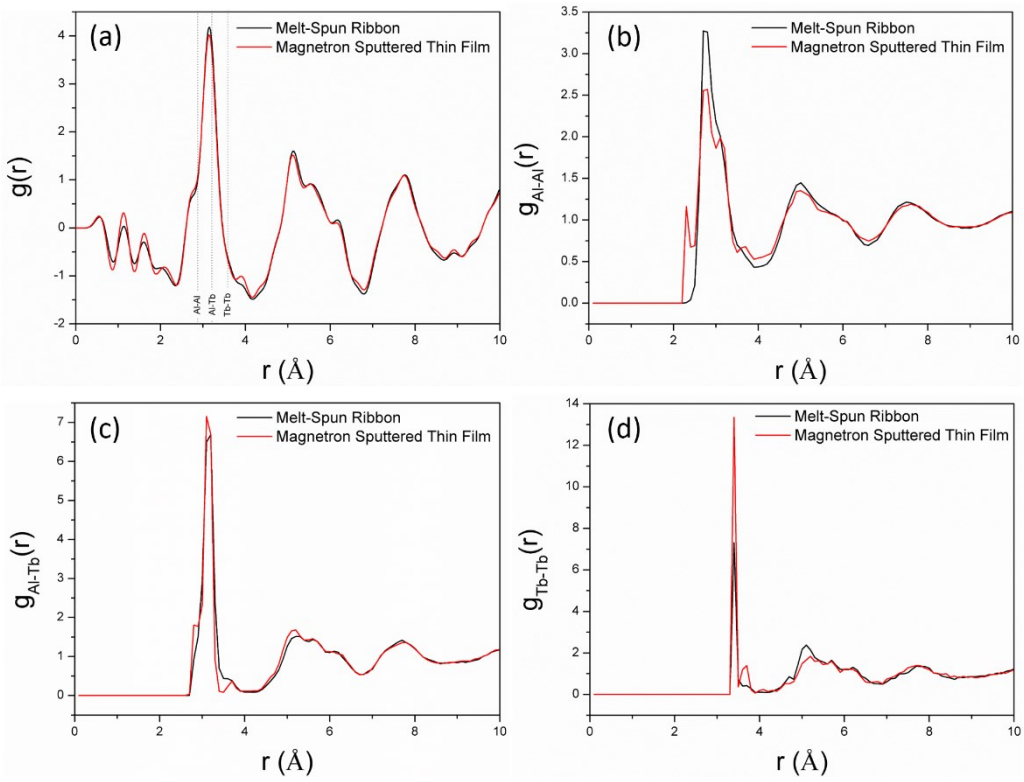

Figure 2.2: (a) Experimental pair distribution functions (PDF) derived from HEXRD for as-spun and as-sputtered $Al_{90}Tb_{10}$. **(b-d)** Partial PDFs of Al-Al, Al-Tb and Tb-Tb of as-spun and as-sputtered $Al_{90}Tb_{10}$ calculated from simulated RMC models.

For further investigation, partial PDFs, $g_{Al\text{-}Al}(r)$, $g_{Al\text{-}Tb}(r)$ and $g_{Tb\text{-}Tb}(r)$, were derived from RMC fitted models (Fig. 2b-d). As foreseen from the experimentally calculated PDF, though there are slight intensity differences, partial PDFs of Al-Al, Al-Tb and Tb-Tb interactions showed similar patterns, showing similar correlations of

coordination for as-spun and as-sputtered $Al_{90}Tb_{10}$. The calculated partial PDF also revealed the intensity difference in the peak located at 3.9 Å of experimental total PDF. As it can be seen in the in the Tb-Tb partial PDF, Figure 2.(d), there is a clear extra peak for the sputtered thin film, whose location corresponds to the aforementioned peak with an intensity difference.

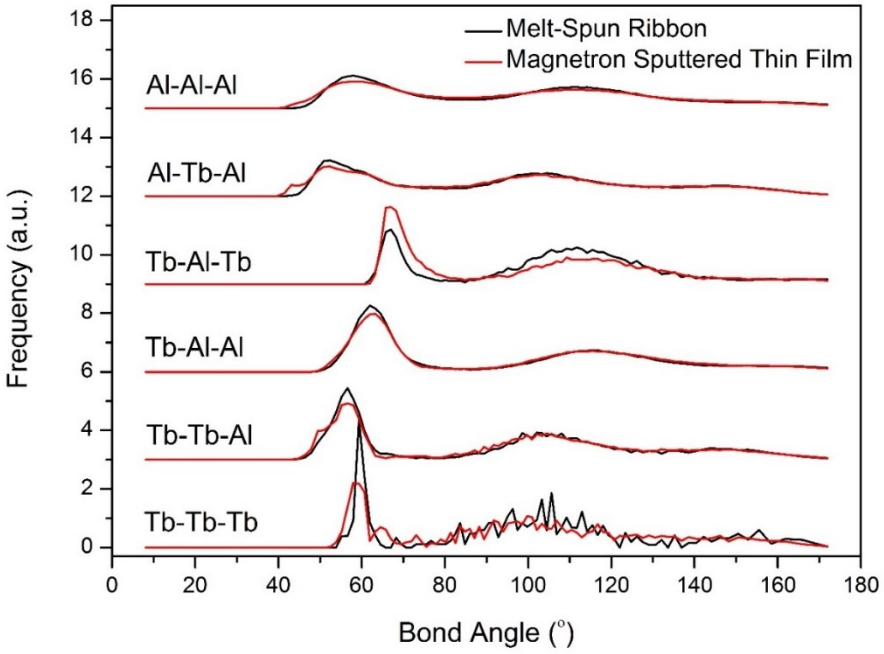

Figure 2.3: The distribution of bond-orientation angles for as-quenched and as-sputtered $Al_{90}Tb_{10}$ alloys calculated from simulated RMC models.

As stated above, Miracle's ECP model[123,136,137] can successfully give out information about local structures using basic atomic properties, such as atomic radii of constituents and alloy composition. The ECP model also predicts the site occupancies and defects with their related parameters from mentioned atomic properties, for fcc-kind of clusteral arrangement scheme. The atomic radii and structural parameters for model related calculations were adopted from [[118]]. For the calculations, radii of aluminum and terbium atoms were taken as 1.41 and 1.76 Å, respectively. For validation of the model for the current $Al_{90}Tb_{10}$ metallic glass, density was computed with the given theoretical relations in [[123]]. The model predicts the density of $Al_{90}Tb_{10}$ metallic glass alloy with 5% accuracy with respect to measured density of melt-spun

ribbons and with 10% accuracy with respect to the density computed from *ab initio* MD calculations[155].

Table 2.1: Comparison of average bond orientation angles of as-spun and as-sputtered $Al_{90}Tb_{10}$ from simulated RMC models

$Al_{90}Tb_{10}$	**Al-Al-Al**	**Al-Tb-Al**	**Tb-Al-Tb**	**Tb-Al-Al**	**Tb-Tb-Al**	**Tb-Tb-Tb**
Melt-Spun Ribbon	61.8	53.3	67.5	64.6	56.7	60.1
Magnetron Sputtered Thin Film	62.1	53.0	67.9	65.2	56.6	60.1

Bond-orientation angle distributions were calculated for Al-Al-Al, Al-Tb-Al, Tb-Al-Tb, Tb-Al-Al, Tb-Tb-Al and Tb-Tb-Tb triplets of as-spun and as-sputtered $Al_{90}Tb_{10}$ from RMC calculated models, and given in Figure 3. The values of the first shell bond angles are summarized in Table 2.1. As it can be seen from the tabulated results, the average values of bond-orientation angles of as-spun and as-sputtered cases are fairly similar. However, as seen in Figure 3, the bond-orientation angles are much more distributed around the average value for the as-sputtered case; as peaks of each angular triplet of sputtered thin film are broader with respect to melt-spun ribbons'. The frequencies of the bond-orientation angle distributions are also quite similar, yet few deductions can be made. Tb-Tb-Tb coordination is much stricter and well defined for melt-spun ribbon as compared to sputtered thin film as a large bond-orientation angle frequency difference is observed. Whereas, angular frequency of Tb-Al-Tb coordination is higher in the first shell of sputtered thin films as compared to melt-spun ribbons. Furthermore, for both cases, Al-Tb-Al bond angles were found as 53° and Al-Al-Al bond angle triplet as 62°. The values for both Al-Al-Al and Al-Tb-Al is in good agreement with the ECP model, as these values coincide with the predicted minimum angular separation for optimal packing[139]. Thus, from solute-solvent bond angles stand point, the packing of clusters in the first coordination shell can be said to be optimally packed. Considering all of the bond-orientation triplets, one can clearly see that a vast distribution of bond angles is present, an indication of irregular polyhedral coordination in the first shell of both as-spun and as-sputtered cases. Due the complex polyhedral coordination, making comments about local structure just by

bond angle analysis can be misleading. Thus, by making use of the simulation models that was used in RMC modelling, Voronoi Tessellation analyses was applied on the models of as-spun and as-sputtered $Al_{90}Tb_{10}$.

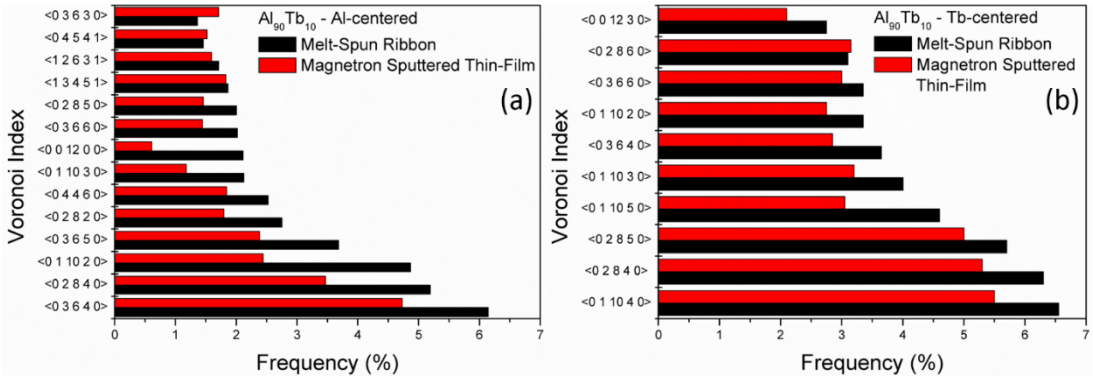

Figure 2.4: Comparison of frequent Voronoi Polyhedra, calculated for both melt-spun ribbon and sputtered thin film with respect to (a) Al-centered and (b) Tb-centered clusters.

Voronoi indices of most abundant clusters for melt-spun ribbons and sputtered thin films were compared in terms of Al-centered and Tb-centered clusters as in Fig. 4a and 4b, respectively. Diversity of cluster types are significantly lower in the melt-spun ribbon case as compared with sputter-deposited films. In our models consisting of 20,000 atoms, the total number of Voronoi polyhedra types for melt-spun ribbon is 941, whereas for sputter-deposited film case is 1279. The dominant Voronoi polyhedra types of Al-centered clusters for both as-spun and as-sputtered cases were found to be similar, yet relative occurrence frequencies are lower in the model of sputtered thin film. The dominant polyhedra for Al-centered clusters were found as <0 3 6 4 0>, <0 2 8 4 0>, <0 1 10 2 0> and <0 3 6 5 0>. Topologically, one striking difference between melt-spun and sputtered models is the frequency depression of icosahedral cluster, <0 0 12 0 0> in the model of sputtered thin film. This discrepancy can be explained with the difference in the amorphization precursor and cooling rate for melt spinning and magnetron sputtering. In the case of sputtering, the amorphous phase is quenched from vapor phase, whereas liquid phase is quenched in melt spinning. Considering the facts as liquid structure is dominated by icosahedral topology[106,113] and it is known that

icosahedral ordering gradually intensifies as reaching to the glass transition[11], the higher frequency of regular icosahedra in melt-spun ribbons could be a legacy from the molten state. Thus, quenching from vapor state could suppressed icosahedral ordering with respect to quenching from molten state. Cooling rate difference can also be the reason behind the depression of icosahedral ordering in sputtered thin films, as the cooling rate in magnetron sputtering was three orders of magnitude higher with respect to melt-spinning. Kinetics of high cooling rate quenching could have force the structure to form distorted polyhedral topologies, inhibiting the formation of regular icosahedron, rather forming icosahedra with extrinsic four-fold and six-fold disclinations such as <0 2 8 2 0> and <0 3 6 3 0>. Similar phenomena were previously observed for first-principles calculations of Cu-rich CuZr glass[67], that has a similar solute-to-solvent ratio to Al-Tb[118]. Cheng and Ma have observed that increasing cooling rate have decreased the frequency of regular icosahedron and promoted the distorted icosahedra formation. For the case of Tb-centered clusters, Voronoi polyhedra types were again found to be matching for both melt-spun ribbon and sputtered thin film. For both cases polyhedra with highly coordinated four and six-fold disclinations as <0 1 10 x 0> and <0 2 8 x 0> types were stand out. These results are in good agreement with our previous study on $Al_{91}Tb_9$ alloy[132], as we had seen that the mentioned Tb-centered cluster types increase in population by reaching and cooling down below the glass transition. One minor difference in Voronoi polyhedra of as-spun ribbons and as-sputtered thin films is that the frequency of <0 1 10 5 0> topology was depressed in sputtered thin film. Similar to the case of Al-centered clusters, the depression was found to be compensated with an increase in the frequency of more distorted topology of <0 2 8 6 0> cluster. The reason behind this observation can be explained with the ideas that were given above for the suppression of regular icosahedra in Al-centered polyhedra. However, in addition to cooling rate effect on clusters distortion, change in the amorphization precursor may have a slightly prominent effect on this observation. Previous studies on Al-RE melts had revealed the coordination of RE atoms in the liquid state is around 16, and nearly matches the RE coordination in amorphous state[96,129,152]. Thus quenching from vapor state rather than liquid may have lead the clusteral arrangement of atoms with 16 coordination to

be more distorted. Nevertheless, with minor differences aside, the topology selection around RE atoms seems to be independent of both cooling rate and the precursor.

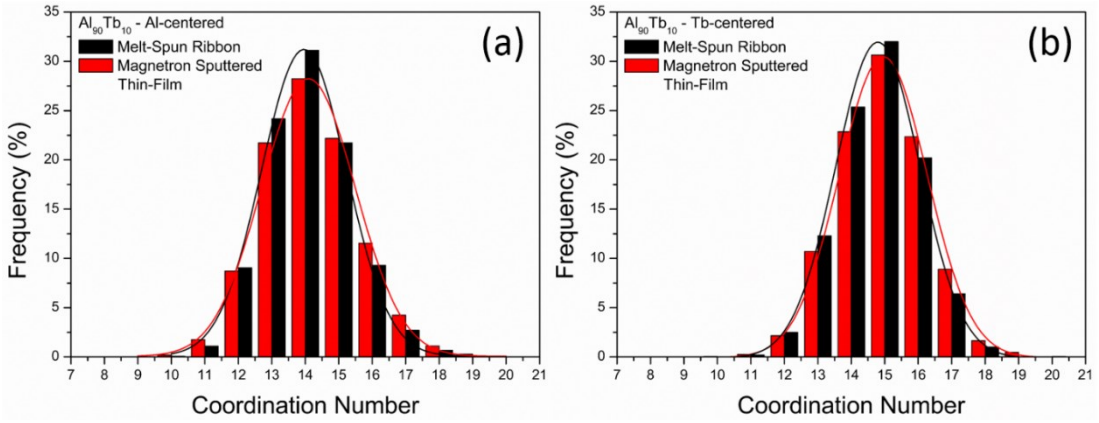

Figure 2.5: Coordination numbers calculated for (a) Al and (b) Tb centered from Voronoi Tessellation of as-quenched and as-sputtered $Al_{90}Tb_{10}$.

Coordination numbers for both Al-centered and Tb-centered clusters were calculated using Voronoi Tessellation were given in Fig. 5a and 5b, respectively, and in Table 2. It can be seen that the average local coordination number of Tb-centered clusters are 15 in both as-spun and as-sputtered cases. Whereas average local coordination number of Al-centered clusters are 14 for the as-spun and as-sputtered $Al_{90}Tb_{10}$, respectively. The computed coordination numbers are in good agreement with the coordination numbers we had reported for the melt-spun $Al_{90}Tb_{10}$[95] and also with X-ray absorption fine structure measurements for Al-RE alloys with similar constitution[159,160]. Thus, as expected from the finding from the literature[161,162], the results show that average local coordination numbers for both Al and Tb-centered does not change by changing the amorphization precursor and the cooling rate.

The local coordination numbers according to structural efficient cluster packing model of Miracle[137,138] is computed and given in Table 2. It should be kept in mind that the computed values of local coordination from mentioned theories makes use of the experimentally found radii of the atomic species in alloyed states with an error of ±6 pm[118]. As it can be seen from the comparison in Table 2, ECP model overestimates the local coordination around Tb atom as 17, and underestimates local coordination around

Al atom as 13. The mismatch between the observations and calculations could arise from the fact that structural models of glasses accounts atomic configurations solely topologically, without considering chemical interactions between solute and solvent atoms. Deviations from the predicted values is an indication of chemical effects arising from bonding, considering the fact that Al-RE interaction could not to be not purely metallic due electronic configuration choice of RE's 4f valances.

Table 2.2: Comparison of local average coordination numbers of as-spun and as-sputtered $Al_{90}Tb_{10}$ from simulated RMC models and ECP model

	Al-centered	Tb-centered
Melt-Spun Ribbon	14	15
Magnetron Sputtered Thin Film	14	15
ECP Model	13.08	17.00

By combining all the results; partial PDFs, bond angle and Voronoi analyses, and calculated coordination numbers, an overall conclusion can be drawn as changing the amorphization precursor and increasing the cooling rate does not alter the topological SRO drastically. The given SRO analyses of melt-spun ribbons and sputtered thin films show that producing amorphous structures from different production techniques result into the same SRO for the same solute content of RE. Though slight distortions on the topology of SRO structures in sputtered thin films were found to be present.

Previous studies on $Al_{90}Tb_{10}$ melt-spun ribbons and magnetron sputtered thin films by Yıldırım et al. showed that changing the amorphization precursor alters the crystallization path on thermal devitrification[156]. Upon thermal devitrification, both melt-spun ribbon and magnetron sputtered thin film produces nanocrystalline fcc-Al as their first crystallization product, thought the fcc-Al nanocrystals in sputtered thin film are more populous and much finer in size as compared to melt-spun ribbon. The ribbon continues to devitrify with a metastable hexagonal phase and with further annealing, the hexagonal phase transforms into a metastable cubic phase with a first-order thermal reaction. The sputtered thin films, however, produces the metastable cubic phase directly after fcc-Al crystallization. As the present results show, both melt-

spun ribbons and sputtered thin films possess similar SRO. Thus, alteration of devitrification path could be due to the change in medium-range correlations via change in the amorphization precursor and cooling rate[156].

Figure 6 shows the variance, V(Q), for the melt-spun ribbon and sputtered thin film. The crystalline reflections of fcc-Al are indicated in Figure 6 for guidance, as well. It should be noted that FEM data are more often presented using $k = \frac{sin\theta}{\lambda}$ for the momentum transfer, but we use $Q = 4\pi k$ here for comparability with the HEXRD results. As being highly sensitive to medium-range correlations[66,122,163], qualitative inspection of the FEM patterns indicates the structure of thin films are more disordered with respect to melt-spun ribbons, as the variance of thin films are depressed than ribbons. Considering the shift and broadening of pre-peak and RMC calculated SRO analyses that had been done on as-spun and as-sputtered glasses, together with the devitrification path difference between the two glasses[103,156], we could interpret FEM results as ordering is much more pronounced for melt-spun ribbons the medium-range length scale. The V(Q) for melt-spun ribbon shows reflections of possible fcc-Al-like medium-range order (MRO) which was also reported by previous studies[73,164]. In our aforementioned study, we had reported the initial fcc-Al nanocrystallization number density is three orders of magnitude higher for thin films than ribbons, reaching values of 10^{25} m^{-3},[156]. Difference in the number density of primary devitrification product for the glasses with the same alloy composition indicates that fcc-Al-like MRO structures are probably smaller in size and more finely distributed in the thin film than of ribbon. On further examination of FEM analyses, one can see the unidentified reflections on FEM patterns. We think these peaks are manifestations of Al-depleted MRO network in the glass[95,132,150,156], as these peaks coincide with many of the reflections of the well-known Al-rich Al-Tb intermetallics (i.e. Al_3Tb, Al_4Tb, $Al_{17}Tb_2$). However, considering the devitrification paths of the $Al_{90}Tb_{10}$ melt-spun and sputtered samples, both glasses devitrify through crystalline phases with unidentified space group symmetries[156]. Thus, if one considers the theory that MRO structures in glassy structure to resemble the atomic correlations in the devitrification product, the unidentified reflections in FEM patterns could be reflections these Al-depleted MRO.

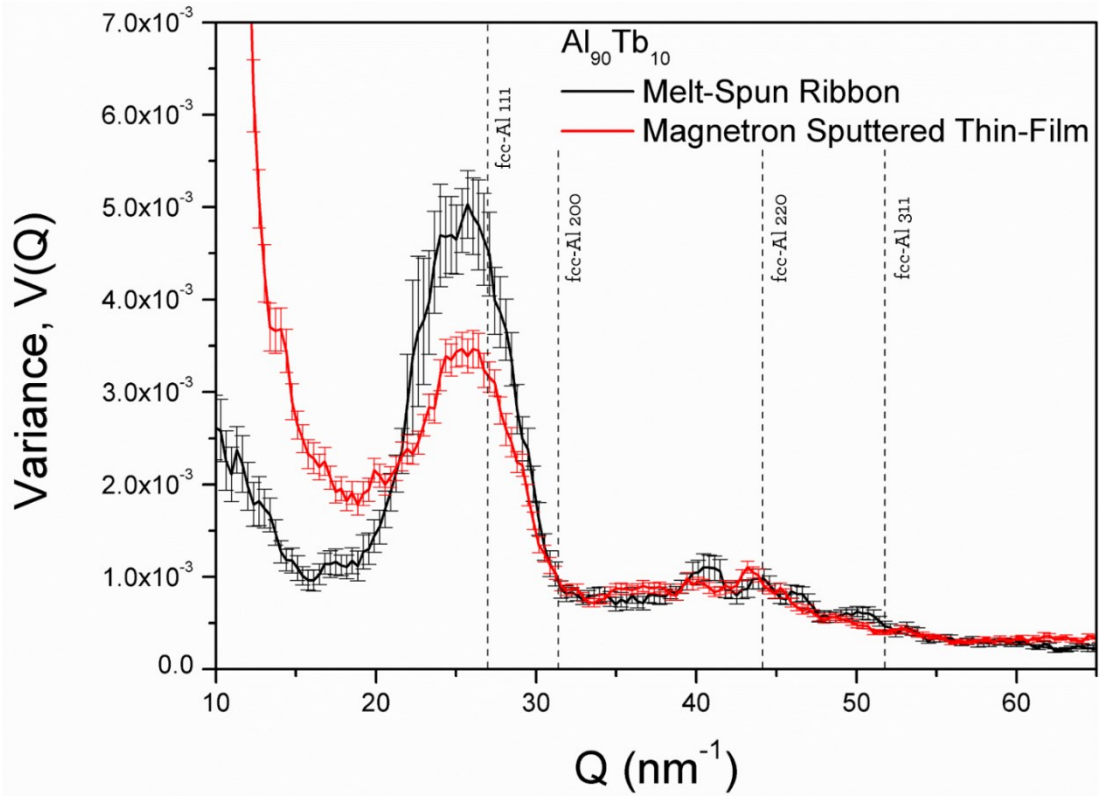

Figure 2.6: Fluctuation Electron Microscopy patterns obtained for as-spun and as-sputtered $Al_{90}Tb_{10}$ metallic glasses [Courtesy of P.M. Voyles].

There also exists positional difference of reflections between two FEM variances of melt-spun ribbons and sputtered thin films; meaning that the scattering manifestations of MRO from two amorphous phases with the same composition may differ. Observation of such disparity could be the reason for the devitrification path alteration: After the completion of initial fcc-Al devitrification, with RE rejection occurring while nearly pure fcc-Al nanocrystallization[151,165,166], the medium-range structural correlations of the respective retained amorphous phases could go into different configurations. The solute rejection from nanocrystals to amorphous matrix could also change the ordering on the first coordination shell, which can induce alterations on the higher order coordination of both solute and solvent atoms, as MRO structures are extended ordering of first shell coordination[67,104]. Keeping the idea of MRO structure could decrease the total free energy of the system via increasing the packing

efficiency[123,141], the nucleation of different devitrification products after initial fcc-Al nanocrystallization could be promoted energetically, as well.

Short-to-medium-range structural ordering in the glassy state looks as an evident structural feature of the amorphous structure. The results of the current study indicate that for two Al-Tb glasses of same composition, changing the production variables, like changing the amorphization precursor and the cooling rate does not alter the SRO around both solute and solvent atoms, rather extended ordering of SRO structures in the medium-range is altered. Thus, as our previous study points out[156], glasses of same composition with different MRO structures had showed different the thermal devitrification behavior, both crystallization path-wise and initial crystallization precipitation-wise. Considering the mentioned observations, hence arises the question about the roots of short-to-medium-range ordering. We believe that metallic amorphous phase formation in glass forming systems is essentially dependent on the properties of alloy system and the production procedure. For a glass forming alloy, the physicochemical interaction of constituent atoms defines the bonding behavior of the solute and solvent atoms. Chemical and topological SRO formation seems to be taking place via a combined effect of the chemical bonding behavior and the constraint exerted from the size difference of constituents. As a result, whether the system is in molten or glassy state, chemical and topological ordering on first coordination shell is defined. The results of our previous Monte Carlo study of $Al_{91}Tb_9$ glass forming system[132] proved that idea, as topology of Tb-centered clusters were equivalent through cooling from well above the liquidus to room temperature. Similar equivalent SRO evolution was also observed in MD calculations on CuZr liquids and glasses[11,167,168]. The atomic size relations should also be considered for SRO evolution. By taking only the atomic radii into consideration, ECP model has quite high precision in predicting the structural parameters of glassy alloys. Considering the fact that the stability of a glassy system is highly dependent on the space filling in three dimensions (i.e. packing efficiency)[136,137,169], it is logical to assume purely geometry-driven topology formation has a prominent effect on the ordering in the first coordination shell. Furthermore, both current results and previous theoretical results from the literature[12,67] builds up the idea of low dependence of SRO selection with respect to

production procedure; meaning, SRO formation is a weak function of amorphization precursor and cooling rate. Stemming from this idea it may also be speculated that even quenching temperature may have a dim effect on SRO formation in glasses. Thus, the solute-centered (RE) clusters with a certain number solvent atoms (Al) act together in the structure as if they are like a structural element, which may be called as "superatom"'s[129].

The observations on melt-spun and magnetron sputtered $Al_{90}Tb_{10}$ glasses, however, have revealed that though SRO is equivalent in both melt and vapor quenched samples, whereas higher order correlations, namely MRO structures is high dependent on the production procedure. When all the given results were considered, changing the amorphization precursor from molten state to vapor state, together with the three order of magnitude increase in the cooling rate, caused sputtered thin films to be more structurally homogeneous, with respect to melt-spun ribbons of same composition. The structural differences for two cases in the medium-range regime can be discussed through both amorphization precursor and cooling rate points of view. The experimental and theoretical analysis of binary Al-RE and ternary Al-RE-TM glasses with various choice of RE atoms has been revealed that the structure of liquid quenched Al-RE based glasses have either distinct chemical heterogeneities, namely pure and amorphous Al regions of few nanometers[129,170], or the alloy show a nano-scale phase separation before the precipitation of the initial devitrification product, fcc-Al nanocrystals[80,154,171]. As mentioned before, presence of pure-Al regions was observed in the HEXRD and *ab initio* MD constrained RMC calculations of Al-RE glasses and also in the molten state, well above the liquidus temperature[95,129,132]. As formation of pure Al regions in the structure is attributed to the division of the amorphous structure via a polymer-like linking of so called superatoms (i.e. RE-centered clusters coordinated with definite number Al atoms). After RE-centered clusters collect a certain number of solvent Al atoms, the remainder of the Al atoms fill in spaces between the network formed by so called superatoms, without crystallizing in the glassy structure. Furthermore, the number density of these pure Al regions is nearly in the same order of magnitude with the primary devitrification products' number density. If one considers that the superatoms' network formation is

still observable on the molten state, as well, through observation of the pre-peak in HEXRD pattern and with the RMC models, one can end up with a conclusion of implications of structural ordering both in SRO and MRO regime commences way before reaching to the glass transition temperature. Thus, we may hypothesize that pure Al regions are actually inherited from the molten state, which also implies molten state also possess structural features on the medium-range land scale.

Building from the ideas stated, we may also speculate about the cooling rate dependence of the MRO formation. The quenching rate of rapid solidification is known to be one of the controlling parameters for the chemical and topological stability of the glassy structures[12,67,172]. As different quenching temperature and cooling rate can cause distortions on the three dimensional configurations of both solute and solvent centered clusters, thermal annealing is found to be an effective way of reaching to the atomic configuration with the lowest free energy[36,162]. Moreover, quenching with the lowest possible cooling rate (just below the critical cooling rate for amorphization) is also an effective way of approaching to the configuration with the lowest free energy, as the system has relatively more time with faster kinetics with gradual increment of viscosity for α-relaxation, with respect to quenching from higher cooling rates. Conversely, with the reduced kinetic effects, higher cooling rate processing will result in a structure with more homogeneous in both clusters' topology sense and chemistry sense. However, from stability perspective of amorphous phase in Al-RE metallic glasses, the homogeneity arising from high cooling rate application is an energetically metastable state, as evolution of distinct chemical heterogeneities were observed in the amorphous structure with lower cooling rate quenching of the same metallic glass alloy[95]. Hence, with the energy exerted from thermal annealing, before the initial devitrification step, the amorphous phase first forms the chemical heterogeneities of nanometer sized Al-rich and Al-depleted regions via nano-scale phase separation[103], and then devitrifies into crystalline species. The observed nano-scale phase separation reaction before initial devitrification event could be interpreted as the relaxation of the structure through forming energetically more stable amorphous configuration by chemical separation of constituent atoms. Furthermore, the observed nano-scale phase separation of amorphous structure into Al-rich and Al-depleted

regions on thermal annealing sets up the glass structure for the crystallization events by forming the missing MRO structures. Formation of missing medium-range correlations on thermal annealing both ease the forthcoming nucleation event and also influence the phase selection hierarchy on devitrification. As stated before, such nano-scale phase separation reactions were previously observed in sub-T_x annealed melt-spun $Al_{88}Y_7Fe_5$ metallic glass with APT[154] and also in binary $Al_{91}Gd_9$ and $Al_{92}Sm_8$ glasses with small angle X-ray scattering[80,171].

2.5 Conclusion

The solid-state amorphous structure of marginal glass forming $Al_{90}Tb_{10}$ alloy produced with Cu-block melt-spinning and DC magnetron sputtering was investigated. The total X-ray structure factors for both alloys had shown extra scattering peaks. The pre-peak of as-sputtered alloy had shifted to higher-Q and broadened with respect to as-spun alloy. The experimental PDF and RMC calculations had shown that short-range ordering in both alloys are fairly similar. Local coordination number around Al and Tb-centered clusters were found as 14 and 15, respectively for both glasses. The SRO structures were found to be in good agreement with ECP model, regarding to local partial coordination numbers and bond angle separations. The structural difference between as-spun and as-sputtered alloys on medium-range scale was detected with FEM. The devitrification path difference between these alloys of same composition was attributed to the structural differences of MRO, rather than ordering on the first coordination shell.

2.6 Acknowledgement

This work partially supported by the Scientific and Technological Research Council of Turkey (TUBITAK) under Grant No. 113M346. The high-energy *in situ* X-ray experiments were performed at the BL04 - MSPD beamline of the ALBA Synchrotron Facility, and financially supported by CALIPSO program. Appreciation is expressed to Inmaculada Peral and Oriol Vallcorba for his valuable help in HEXRD experiments. Work at Ames Laboratory, sample synthesis, was supported by the US Department of

Energy, Basic Energy Sciences, Division of Materials Science and Engineering, under Contract No. DE-AC02-07CH11358.

CHAPTER 3

Al-RE-BASED AMORPHOUS/NANOCRYSTALLINE COMPOSITE POWDER PRODUCTION AND CONSOLIDATION

3.1 Abstract

Amorphization and consolidation behaviors of several Al-based metallic glass forming alloys with mechanical milling or alloying were studied with high energy shaker milling followed by pressing and sintering. In the first trials mechanical milling technique was adapted and failed to produce amorphous forms of gas-atomized $Al_{90}Sm_{10}$ and suction casted $Al_{85}Sm_7Fe_5Cu_3$ alloys with extensive milling for 140 hours. Secondly, mechanical alloying was adopted as a production route, and partially amorphous $Al_{88}Sm_7Ni_5$ and $Al_{88}Sm_7Fe_5Ni_3$ powders were obtained. As-milled state of mechanically alloyed $Al_{88}Sm_7Fe_5Ni_3$ amorphous/ nanocrystalline composite powders were characterized using XRD, SEM, DSC, HEXRD and TEM. Consolidation behavior of mechanically alloyed $Al_{88}Sm_7Fe_5Ni_3$ amorphous/ nanocrystalline composite powders was studied and optimized with the help of DSC, and adapted to sintering in a muffle furnace. Finally, consolidation of bulk ex-situ composites with mentioned powders and pure Al powder were produced by warm pressing and mechanical behavior of these structures were investigated with compression and hardness tests with post-mortem SEM studies. This work partially supported by the Scientific and Technological Research Council of Turkey (TUBITAK) under Grant No. 113M346.

3.2 Introduction

Aluminum based metallic glasses are an important class of amorphous alloys with their promisingly superior properties for structural engineering applications. The experimental work on Al-based metallic glasses have revealed that these alloys possess quite high strength, far beyond that any conventional crystalline Al alloy could ever reach, together with reasonable ductility[21,27], low density and superior corrosion resistance[173,174]. However, the main hindrance behind their commercial usage is that Al-based metallic glasses obtained via rapid solidification techniques could only be produced in very small cross-sections. There are many studies in literature concerning improvement of the glass forming ability (GFA) of Al-based metallic glasses through compositional tailoring. This was done through alloying a base composition of Al and rare earth metals (RE) with transition metals (TM) and metalloid atoms, solely[175] or in combination[21,176]. Nevertheless, by making use of trial & error method and phenomenological guidelines (i.e. Inoue's empirical GFA rules), the GFA of Al-based metallic glasses on rapid solidification processing is still quite low; ranging from several micrometer ribbons[24,25] to 1 mm casted rods[33,174].

As stated above, production of Al-based "bulk" metallic glass structures are tedious and in inconclusive with rapid solidification processing. Powder metallurgical production techniques is found to be a remedy for that problem. The main route of powder processing for obtaining bulk metallic glass samples is done by three main steps: production of amorphous powders, pressing and sintering of the amorphous powders below their crystallization temperature. This way was found to be useful for obtaining bulk glassy structures, that can and/or cannot be produced with rapid solidification processing[177–181]. The amorphous powder production for powder metallurgical route can either be done by using another rapid solidification technique called "gas atomization" [36,53] or SSAR processing routes, namely mechanical milling and alloying[36,53,54,57]. Detailed explanation of glass formation of the mentioned rapid solidification and SSAR processes are given with thermodynamical and kinetic aspects in Chapter 1, Section 1.2.4. The consolidation of amorphous powders can be done

either with cold pressing, followed by sintering below crystallization temperature or by warm pressing procedures.

Table 3.1: Literature review of mechanically alloyed Al-based metallic glasses

Alloy Composition	Production Parameters	Ball-to-Weight Ratio	Final Microstructure	Reference
$Al_{60}Fe_{20}Ti_{15}Ni_5$	High Energy Mill 30 hours	10:1	Amorphous	[182]
$Al_{60}Fe_{15}Ti_{15}Mg_5B_5$ $Al_{60}Fe_{15}Ti_{15}Co_5B_5$ $Al_{60}Fe_{15}Ti_{15}Zr_5B_5$	High Energy Mill 35 hours	10:1	Amorphous	[179]
$Al_{65}Cu_{20}Ti_{15}$	High Energy Mill 25 hours	10:1	Amorphous +Al_2Cu	[59]
$Al_{85}Fe_{15}$	Planetary Mill 300 hours	20:1	Amorphous	[183]
$Al_{85}Fe_{15}$ $Al_{89}Fe_{17}$	High Energy Mill 50 hours	10:1	Amorphous	[184]
$Al_{75}Ni_{10}Ti_{10}Zr_5$	Planetary Mill 110 hours	20:1	Amorphous	[180]
$Al_{85}Y_7Fe_5Ni_3$ $Al_{83}Y_7Fe_5Ni_5$ $Al_{81}Y_7Fe_5Ni_7$	High Energy Mill 30 hours	10:1	Amorphous +Unknown	[185]
$Al_{82}La_{10}Fe_4Ni_4$ $Al_{88}La_6Fe_3Ni_3$	Planetary Mill 350 hours /300 hours	20:1	Amorphous Amorphous +fcc-Al	[181]

Gas atomization method for amorphous powder production is generally used for alloys with high GFA [53,177], as by nature it is a rapid solidification method. In this method,

the master alloy is melted in a crucible and sprayed form an orifice beneath the crucible with He or Ar positive pressure. The sprayed molten metal is then breaks down to small droplets, “atomized”, with applied of high pressure gas. Owing to Gibbs-Thomson effect, particles ranging from nm-to-µm sizes undercools to a greater extent. These small undercooled droplets solidify rapidly with quite high cooling rates, ~10^5-10^6 K/sec, forming metallic glass powders. As stated, production of amorphous powders with mechanical milling and alloying routes were already given in Chapter 1, Sections 1.2.4.1 and 1.2.4.2.

As mentioned before, one way for bulk production of Al-based metallic glasses is to obtain amorphous powders with SSAR processing with subsequent consolidation. Previous works on Al-based metallic glass powder production are generally concentrated on powder production from mechanical milling and alloying. Production of amorphous powders were generally done using planetary and high energy ball milling in most of the reports. Highlights on the amorphous Al-based powder production with mechanical alloying is given in Table 4.1. All compositions given in that will be given Table 4.1 and throughout the chapter will be in atomic percentages, unless stated. The produced powders are typically consolidated using various techniques, such as vacuum sintering[180,183,186], and spark plasma sintering[33,177,181].

In this study, production of Al-RE based amorphous powders and their consolidation behavior is studied. In the first part, production routes and parameter utilization, and characterization of produced powders are explained. In the second part, consolidation trials and their corresponding mechanical behavior are given.

3.3 Experimental Procedure

Gas atomized powders of $Al_{90}Sm_{10}$ were produced at Ames Laboratory with high pressure gas atomization technique. High purity alloying elements (>99.99 w.t.%) were melted at 1473 K in a Al_2O_3 crucible and atomized using He gas with 5.5 MPa pressure. The obtained powders were screened using ASTM standard sieves using a vibratory shaker. Suction casted rods were prepared using an Edmund Bühler arc melting unit using high purity constituents (>99.5 w.t.%) under Ar atmosphere. Prior

to suction casting, melting of the charge was repeated three times to ensure the chemical homogeneity. The suction casted rods of 2 mm diameter and 3-4 cm in height was obtained using the suction casting apparatus that was attached to the mentioned arc melting unit. The rods were crushed with a hardened steel mortar before charging for the mechanical milling experiments. For mechanical alloying, high purity elemental powders (>99.5 w.t.%) weighted to match the stoichiometry and they were fed directly into vial.

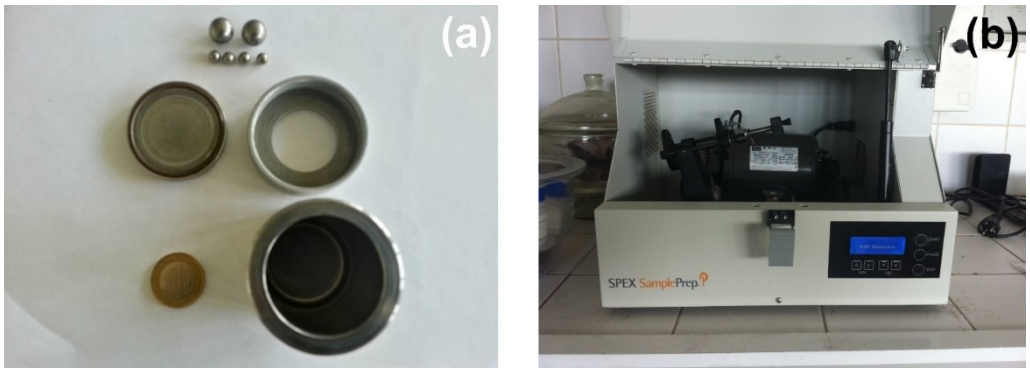

Figure 3.1: (a) Hardened ball and vial set and **(b)** SPEX 8000M high energy shaker mill used for mechanical milling and alloying experiments.

Mechanical milling and mechanical alloying processes were done using SPEX 8000M high energy shaker mill (**Figure 3.1**.(a)) that is rotating at 1425 rpm. The charges were milled using six hardened steel balls (two 1.27 mm and four 0.635 mm in diameter) and vial (**Figure 3.1**.(b)). As the cooling unit of the SPEX mill was not sufficient for the milling experiments, a fan was placed on top of the mill. With the fans support, the observed vial temperature had not exceeded 308 K. For some of the milling experiments the vial fed with the samples were closed under moderate oxygen partial pressure which caused unwanted oxidation on the milled samples. Thus, for the rest of the experiments the vial fed with charge was closed in a glovebox having oxygen partial pressure less than 20 ppm under Ar overpressure. All of the milling experiments were done using an optimized ball-to-weight ratio of 10:1. For each milling experiment 2 grams of charge was fed and the final yielding was on the order of 1.95 grams. The milling was done on 100 minute periods, with 40 minutes of rest between each period. The rest was done in avoidance to overheat the milled powders. The vial was also

turned upside down before each period of milling to ensure the chemical homogeneity and to prevent agglomeration.

The consolidation of amorphous/nanocrystal composite powders were performed using uniaxial pressing and sintering, and warm pressing. Uniaxial pressing processes were done using two hydraulic presses with maximum loads of 30 and 300 tons. The dies and hydraulic presses used in this study can be seen in **Figure 3.2**. Initial trials had shown that the effective pressure that can be obtained from the hydraulic presses are 125 MPa and 1300 MPa with 15 mm diameter dies, for presses with 30 and 300 tons load capacities, respectively. Green compacts of the samples were obtained with the application of the mentioned effective pressure for 30 minutes using dies of 15 mm diameter dies. Sintering trials were done using differential scanning calorimeter (DSC) and a muffle furnace. Temperatures and durations of the first thermal transformation of green compacts were predetermined by isothermal DSC holds at various temperatures from ~10 mg samples. Sintering of the samples that had been subjected to mechanical tests were also carried out in DSC, as it provides information about thermal events that are taking place, together with providing certain atmosphere control. For sintering trials with muffle furnace, samples were enclosed within vacuum evacuated a Pyrex tube with Ar positive pressure. For each sintering trial, muffle furnace was preheated to the predetermined sintering temperature that was obtained from the isothermal DSC holds. Consolidation with warm pressing was done with the mentioned 30 tons load capacity hydraulic press. The warm pressing setup was only viably used in the low load capacity press, for that reason in order to increase the effective pressure on the powders, a smaller die with diameter of 10 mm was used. The effective pressure on the powders was on the order of 250 MPa. Warm sintering consisted of the following: The 10 mm die with its insulating jackets was placed on the press, and it was heated up to temperature range of 473-523 K with a hot-air blower. Temperature of the ambient and the die was tracked with a K-type thermocouple and an infra-red thermometer, respectively. A dark dot was painted on the die and used as a pointing area for the infra-red thermometer, for a proper measurement. The procedure used for warm pressing was as follows:

i. The powders were sieved with a vibratory shaker to obtained a homogeneous particle size distribution,
ii. The screened powders were put into the die,
iii. A pre-pressing without heating was done,
iv. Warm pressing was done for a predetermined time and temperature under constant load.
v. Certain measures were taken in order to protect the load cell of the press from the heating apparatus.

Figure 3.2: (a) A 15mm diameter die used for pressing experiments. **(b)-(c)** The hydraulic presses used for the experiments having 30 and 300 tons of maximum loads, respectively.

Thermal characterization of the as-milled powders, green compacts and also the sintering trials of the mechanical test samples were conducted using SEIKO SII X-DSC7000. For both isochronal and isothermal DSC runs, the samples of ~6 mg were weighted and loaded into Al crucibles. The isochronal measurements were done with heating rates of 10, 20, 30 and 40 K/minutes. For isothermal holds, the samples were first heated to the determined temperature with 100 K/minutes and hold for 120 minutes. The experiments were conducted up to 723 K under high purity N_2 flow of 40 cc/minutes. Baseline correction were performed for each heating rate using empty Al crucibles as reference. Morphological and chemical analyses of the specimens were done using FEI Nova NanoSEM 430 Field Emission Gun (FEG) and JEOL JSM 6400 scanning electron microscopes (SEM), both attached with energy dispersive X-ray spectroscopy (EDS) units, operated at 20 kV. For surface topological investigations, the accelerating voltage of SEMs were depressed to 5-10 kV, to increase the surface sensibility. Transmission electron microscopy (TEM) investigations were done using

JEOL 2100F-FEG TEM, operated at 200 kV. Powder samples were prepared for TEM by sedimentation of powders in ethanol for 10 minutes and dropping onto holey carbon grids. Conventional X-ray diffraction (XRD) experiments were done using Rigaku Ultima IV and Bruker D8 Advance diffractometers with Cu-Kα radiation. XRD patterns were collected at Bragg-Brentano geometry with 10°-100° 2θ range, 0.02° step size and 0.1°/minute scan rate. XRD patterns of bulk samples were conducted in Bruker D8 diffractometer with parallel beam geometry, using the given experimental parameters. Synchrotron XRD experiments were performed in ALBA Synchrotron Radiation Light Source's BL04-MSPD beamline. A beam energy of 30 keV (0.0413 nm) was selected by a Si(111) double crystal monochromator. The photon flux in the beamline at 30 keV was 4x1012 photons/second through a beam cross-section of 0.5x0.5 mm2. Phase transformations occurring in the samples were detected by Mythen array detector, having capability of scanning 40° instantaneously. The samples were heated with a hot air blower with a heating rate of 20 K/min. Hot air blower was calibrated with Si standard sample prior to experiments. Samples were loaded into low X-ray absorbing borosilicate capillary tubes. Diffraction pattern from the empty capillary tube with the same experimental parameters was also collected for baseline and air scattering correction. Particle sizes of the as-milled powders were determined using Malvern Mastersizer 2000 particle size analyzer and FEG-SEM. Mechanical tests were performed using INSTRON 5582 UTM universal testing machine. Compressions tests were performed at room temperature (300 K) according to ASTM E-9 standard. For compression tests from consolidated bulk samples, cylindrical samples of 3 mm in diameter and 1.5 mm in height were cut using ultrasonic disc cutter device. Sample surfaces were grinded after the cutting procedure. A strain rate of 0.01 and 0.005 mm/mm.minute was applied for the compression tests. Hardness measurements were carried out using Shimadzu HV-2 Micro Vickers indenter with application of 980.7 mN of load for 10 seconds. Powders samples were impregnated in epoxy resin for hardness measurements. Both powders-embedded-in-resin and bulk samples were metallographically prepared before hardness measurements. Density of produced bulk samples were determined using the Archimedes method with xylene

($C_6H_4(CH_3)_2$) or distilled water. Before every density measurement, precision was calculated measuring pure bulk copper piece which yielded an error margin of 0.09%.

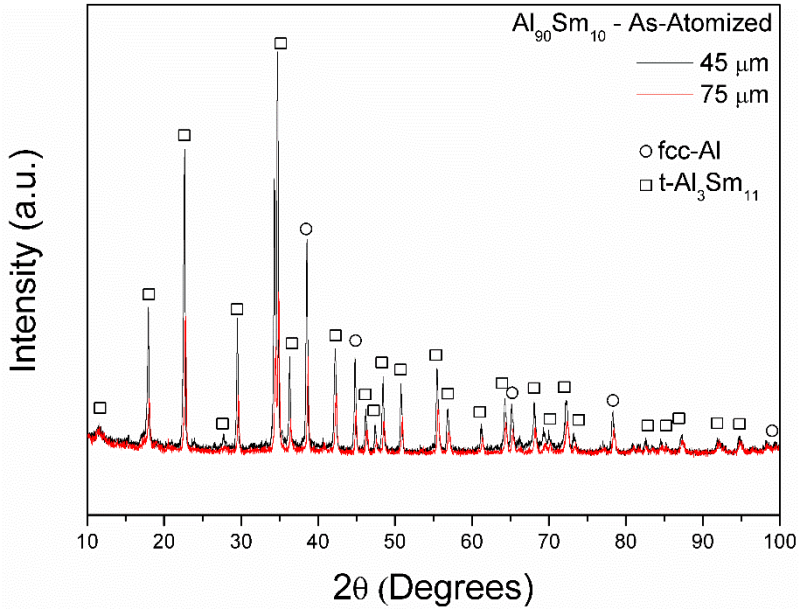

Figure 3.3: XRD patterns of as-atomized $Al_{90}Sm_{10}$ powders with mean particle sizes of 45 and 75 micrometers.

3.4 Results and Discussion

3.4.1 Amorphous/Nanocrystal Powder Synthesis

3.4.1.1 Mechanical Milling

Mechanical milling trials was initiated with gas atomized $Al_{90}Sm_{10}$ binary alloy powders of 45 and 75 micrometers. Powders were sealed under moderate partial oxygen pressure with a ball-to-weight ratio of 20:1. Pre-milled microstructures of gas atomized powders were investigated with XRD and SEM. As seen from Figure 3.3, microstructures of the powders were consisting of fcc-Al and metastable tetragonal $Al_{11}Sm_3$ phases. Backscattered electron (BSE) images of powders in as-atomized condition were taken under SEM is given in Figure 3.4. As it can be seen from the figure, powders have spherical geometry. The figure also reveals tetragonal $Al_{11}Sm_3$ phase giving out a lighter contrast, due its heavy Sm-rich constitution.

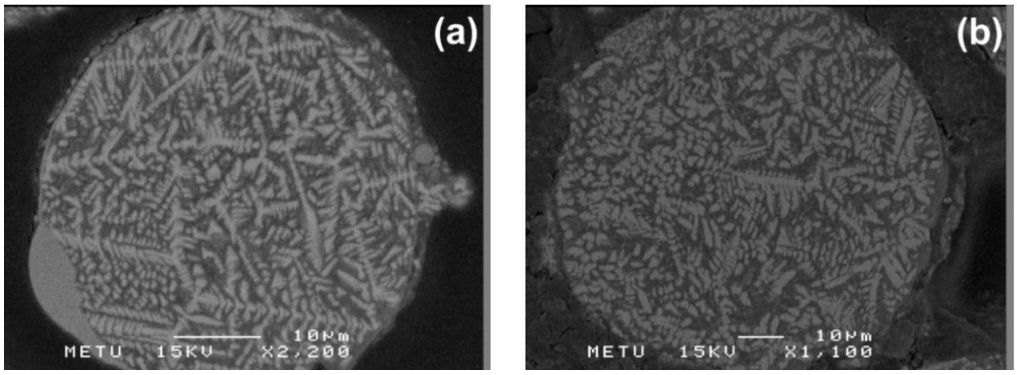

Figure 3.4: Backscatter electron images of as-atomized $Al_{90}Sm_{10}$ powders with mean particle sizes of **(a)** 45 and **(b)** 75 micrometers.

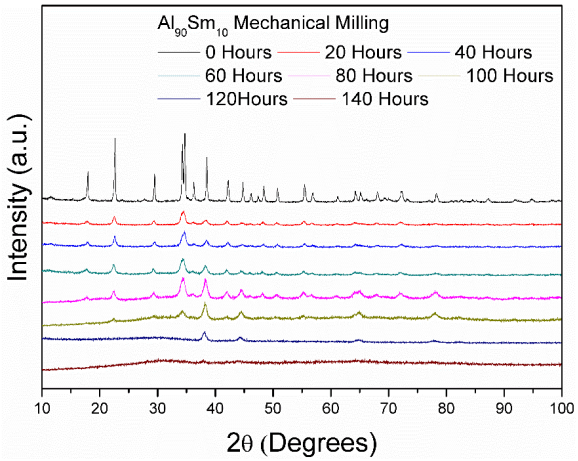

Figure 3.5: Phase evolution during mechanical milling of 45 µm-sized gas atomized $Al_{90}Sm_{10}$ powders.

The temporal phase evolution of mechanically milled $Al_{90}Sm_{10}$ binary gas atomized powders were given in Figure 3.5. To observe the phase evolution, milling was interrupted every 10 hours and an appropriate amount of sample was taken out of the vial to collect the corresponding XRD patterns. As it can be seen from Figure 3.5, with increasing milling time, the peak intensities of the crystalline reflections decrease whilst their full-width-at-half-maximum (FWHM) values increase. Further, after milling for 110 hours, the observed XRD pattern comprised only of fcc-Al phase and an amorphous phase. Although XRD patterns seem to indicate a "desirable" microstructure, further investigations had revealed that it is misleading. Chemical

analysis of powders subjected to 140 hours of milling, with EDS, had revealed that the composition of the powders as 22±2%a.t. O, 71±1%a.t Al, 7±1%a.t Sm (Figure 3.6).

The main reason for the oxidation problem was attributed to the fact that the vial was closed in moderate oxygen partial pressure. As stated above, the vial was opened up in every 10 hours, for phase evolution observation, and the and it was closed down under moderate oxygen partial pressure. Keeping in mind that this procedure was repeated throughout the total milling time of 140 hours, oxygen was probably incorporated into the structure progressively through the milling. Thus, an amorphous phase consisting of Al, Sm and O was formed, rather than forming a metallic Al-Sm amorphous phase. To eliminate the detrimental effect of partial oxygen pressure on the mechanical milling, the powders was started to be sealed in glovebox under Ar positive partial pressure to prevent oxidation of the alloy during milling. The intervals for microstructural evolution observations were also increased, in order to prevent oxidation, further.

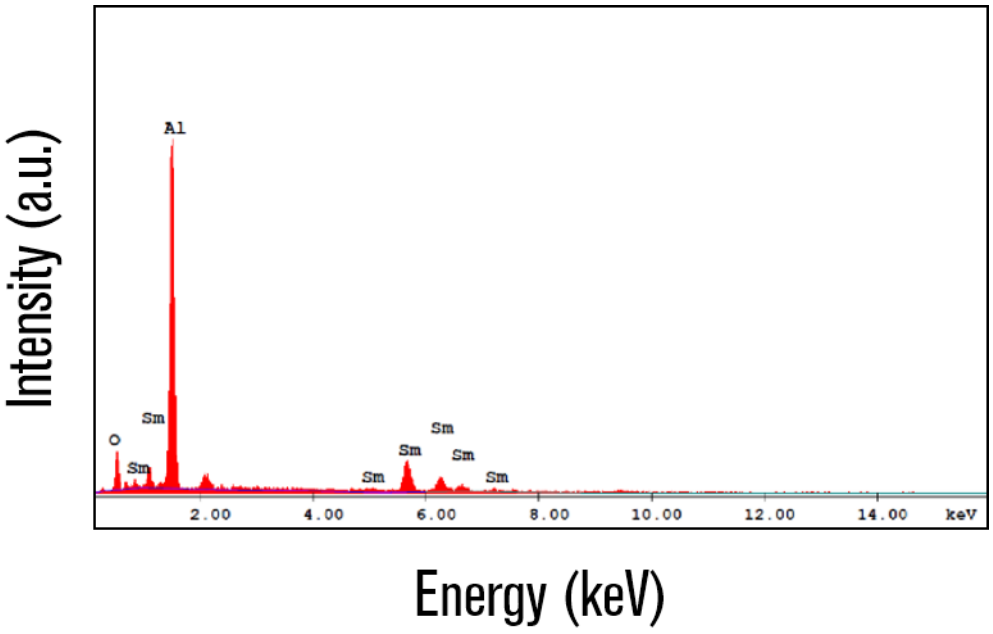

Figure 3.6: EDS spectrum of 45 µm-sized gas atomized $Al_{90}Sm_{10}$ powders, mechanically milled for 140 hours.

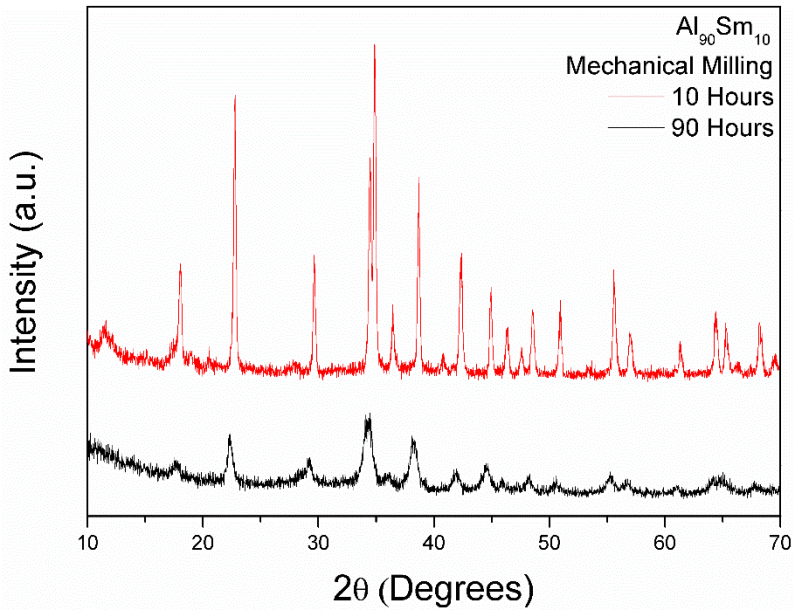

Figure 3.7: XRD patterns of gas atomized 75 μm-sized $Al_{90}Sm_{10}$ powders after mechanical milling for 10 (black line) and 90 hours (red line).

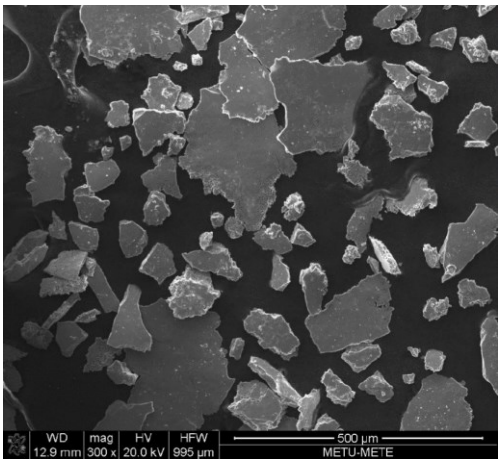

Figure 3.8: SEM image of gas atomized 75 μm-sized $Al_{90}Sm_{10}$ powders after mechanical milling for 90 hours.

Mechanical milling of gas atomized $Al_{90}Sm_{10}$ binary alloy powders was repeated again with powders of 75 micrometers in size with the mentioned precautions. The XRD patterns of powders milled for 10 and 90 hours were given in Figure 3.7. As it can be seen in the figure, crystalline reflections decrease in intensity and increase in FWHM with increasing milling time. Chemical analysis indicated that closing the vial in low

oxygen partial pressure and Ar positive pressure atmosphere had overcame the oxidation problem. However, the results were still credited as unsatisfactory, as after 90 hours of milling, the microstructure of the powders were still consisted of fcc-Al and an unidentified Al-Sm intermetallic phase that still had withstood to high energy supply via mechanical means, without forming any amorphous phase. Figure 3.8 shows a sample SEM image of powders milled for 90 hours. It was seen that with mechanical milling, powders became agglomerated with the cold-welding and fracturing phenomena, as inferred from the morphologies seen in Figure 3.8.

As projected amorphization could not be attained via milling of gas atomized binary Al-Sm crystalline powders, it was decided to continue mechanical milling trials with an alloy with a higher GFA. In literature, it was established that though there is not a direct relationship between the GFA of alloys under rapid solidification versus mechanical milling, alloys with higher GFA in rapid solidification has almost always high GFA under mechanical milling conditions, as well[54,57]. Using the stated idea, it was thought that the amount of produced amorphous phase will increase and the milling time to reach complete amorphization would decrease, if an alloy with a higher GFA was used. Adapting the ideas through using Inoue's empirical rules for increasing GFA[36,41], Al-Sm binary alloy was substitutionally[136,137] alloyed with transition metals for enhancement of the binary alloy's GFA. For that reason, $Al_{85}Sm_7Fe_5Cu_3$ alloy was produced with arc melting followed by suction casting method. As it was known that suction casting has an effective cooling rate of 10^2 K/seconds[9], the alloy was suction casted into rod shape to increase the supplied undercooling to the melt, by which the suppression of nucleation of possible equilibrium phases was achieved. The suction casted rod was crushed using a hardened steel mortar and it was fed to milling vial in coarse powder form. Figure 3.9 shows the backscattered electron image of as-suction casted microstructure of $Al_{85}Sm_7Fe_5Cu_3$ alloy. It can be seen that the microstructure consists of large Sm-rich primary rod phases. Along with the Sm-rich rods, the rest of the microstructure consists of a low-Z concentrated primary phase, and Sm-rich and low-Z concentrated eutectic phase.

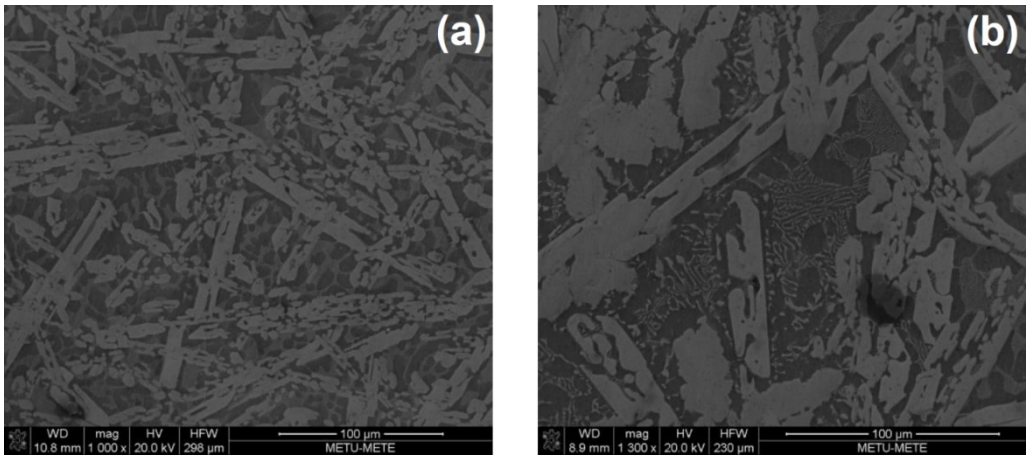

Figure 3.9: Backscattered electron micrographs of as-suction casted $Al_{85}Sm_7Fe_5Cu_3$ alloy.

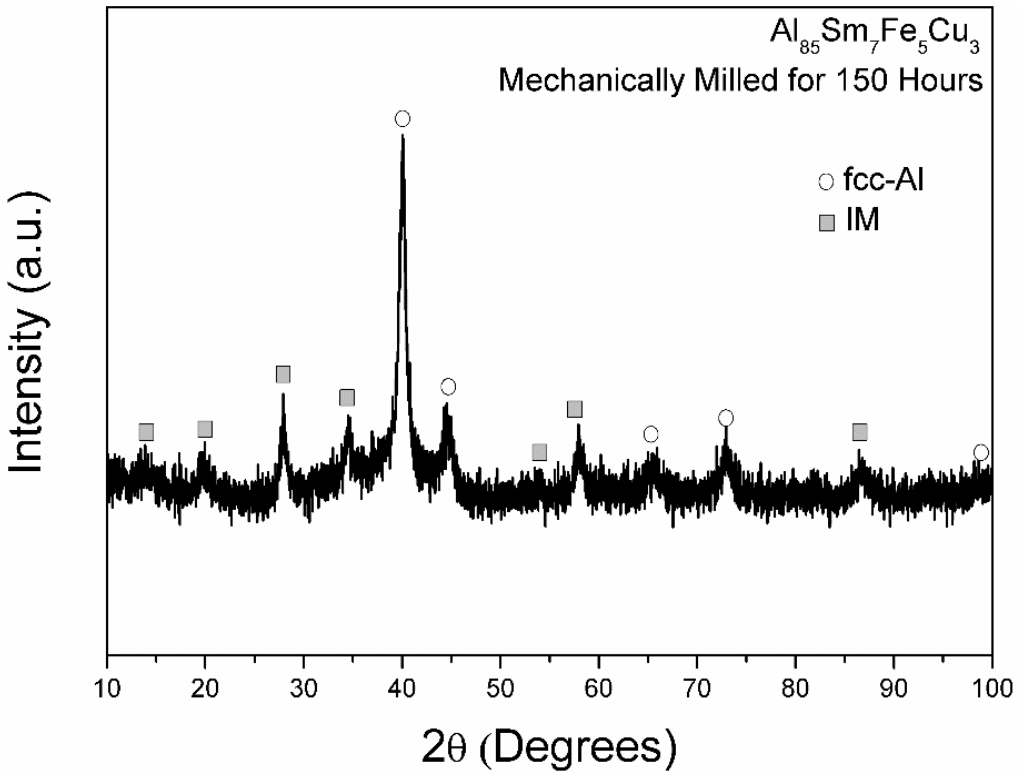

Figure 3.10: XRD pattern of suction casted $Al_{85}Sm_7Fe_5Cu_3$ alloy, after 150 hours of milling.

For the mechanical milling of $Al_{85}Sm_7Fe_5Cu_3$ alloy, a ball-to-weight ratio of 20:1 was used. The vial was closed under glovebox with positive Ar partial pressure. Figure

3.10 shows the XRD pattern that was obtained after milling for straight 150 hours. As it can be seen from the figure, even with extensive mechanical milling, the microstructure of the obtained powders was not fully amorphous, having crystalline fcc-Al and unknown intermetallic phase(s) inside. As compared to the mechanical milling gas atomized of $Al_{90}Sm_{10}$ alloy, lower peak intensities and broader peaks were obtained. However, even after an extensive milling of 150 hours, metallic glass phase formation was still found not to be satisfactory enough for the sake of the presented research. Detailed analyses of EDS and XRD were failed to revel any oxide phase after milling.

3.4.1.2 Mechanical Alloying

As unsatisfactory results were obtained via mechanical milling procedures, mechanical alloying procedure was adopted for metallic glass powder production trials. As stated in the Introduction Chapter and Experimental Procedure part of this chapter, mechanical alloying procedure uses pure elemental powders as starting material. Mechanical alloying trials were also conducted using SPEX 8000M high energy shaker mill. A ball-to-weight ratio of 20:1 was used for all of the powders produced with mechanical alloying means.

Figure 3.11 shows the XRD pattern of the $Al_{88}Sm_7Ni_5$ alloy, mechanically alloyed for 55 straight hours. Unlike mechanical milling trials, X-ray diffraction pattern of the mechanically alloyed ternary alloy had revealed formation of an amorphous phase accompanied with substantial amount of nanocrystalline fcc-Al and unknown intermetallic (IM) phase(s). The final microstructure of $Al_{88}Sm_7Ni_5$ amorphous/nanocrystalline composite was not still in an ideally desired condition, as there still exists unwanted IM phase(s). The intermetallic phases are generally attributed to be an unwanted species in amorphous/nanocrystalline composites due to the reason that IM phases are generally crystallize in faceted morphologies[36], creating sharp edges when crystals are terminating. This is not desired crystals with sharp termination features act as stress concentration centers in the microstructure [187,188], leading to premature failure of the material under mechanical loading. Furthermore, studies on devitrification of the Al-RE and Al-RE-TM metallic glasses had revealed

that these glasses lose their intrinsic ductility on the amorphous state and in amorphous/fcc-Al nanocrystalline composite state when Al-RE rich IM phases start to form [25,28,29,155]. As stated, comments made for formation of IM phase become irrelevant in the case of fcc-Al nanocrystalline phase. Presence of nanocrystalline fcc-Al phase is said to be desirable, since formation of amorphous/nanocrystalline composite increases the strength and hardness of the material, as compared to solely amorphous phase[21]. The enhancement of mechanical properties through introduction of fcc-Al nanocrystals was found out to be independent of crystal's morphology (i.e. same for dendritic or spherical), rather depends on the composition field around the crystal[189].

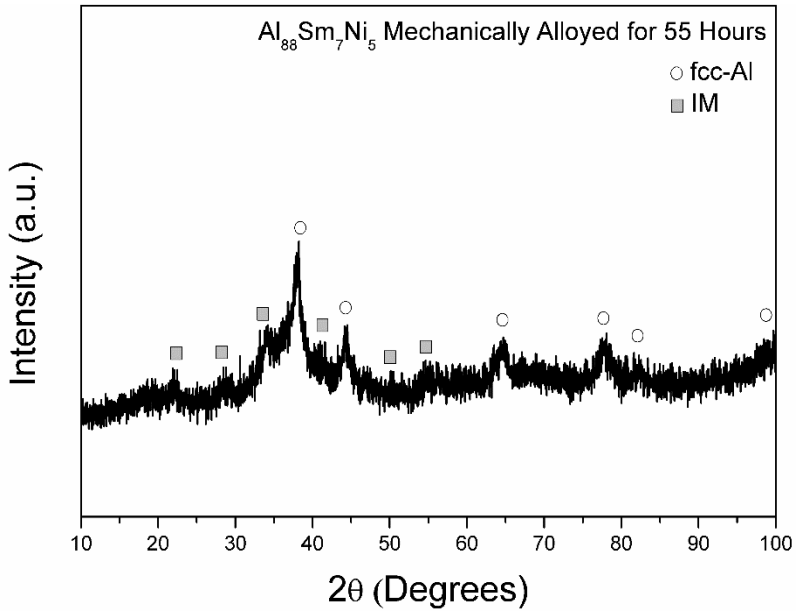

Figure 3.11: Microstructure of mechanically alloyed $Al_{88}Sm_7Ni_5$ alloy milled for 55 hours, revealed via XRD pattern.

The aim in the next mechanical alloying trials was set to depress the IM precipitation in the final microstructure. IM precipitation is known to be depressed by either (i) increasing the "effective quenching rate"[54] by increasing the milling time or (ii) mechanically alloying an alloy composition that is known to have higher GFA due complex the constituent chemistry. The first remedy was declined for the forthcoming mechanical milling trials since dissolution of crystalline IM phase could take up to

several tens of hours, reaching a total milling time of 150-200 hours/sample. Because of the stated temporal problem, the second strategy was adopted for the continuation of mechanical alloying trials, that was the addition of TM elements for tailoring GFA for the desired conditions.

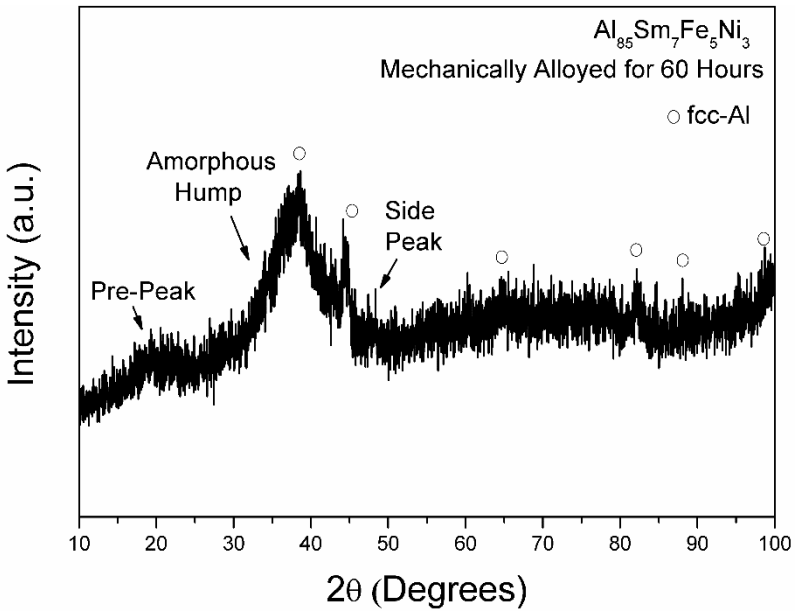

Figure 3.12: Microstructure of mechanically alloyed $Al_{88}Sm_7Fe_5Ni_3$ alloy milled for 60 hours, revealed via XRD pattern.

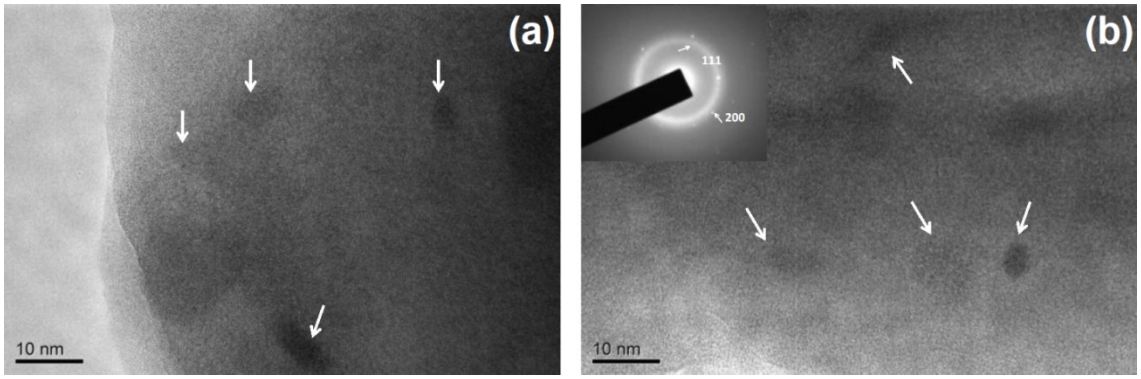

Figure 3.13: BF images and SADP of mechanically alloyed $Al_{88}Sm_7Fe_5Ni_3$ alloy milled for 60 hours.

Figure 3.12 shows the XRD pattern of the $Al_{88}Sm_7Fe_5Ni_3$ alloy, mechanically milled from pure elemental powders. The mechanical alloying was lasted for 60 straight

hours, using a ball-to-weight ratio of 20:1. As the diffraction pattern reveals, the microstructure of the 60 hours mechanically alloyed powders consisted of amorphous phase and nanocrystalline fcc-Al phase. The eye-catching features of pre-peak and side-peak on the diffraction pattern further implies the amorphous phase formation. As stated before, presence of such extra features revealed strong Al-RE and RE-RE interaction from partial structure factor analyses[95,129]. In Al-RE metallic glasses, RE atoms tend to collect high number of Al atoms around them, according to their respective radius ratio over Al[95,132,137,155,190]. Thus, formation of pre- and side-peaks are implicit indicators that amorphous phase had formed a "desired amorphous microstructure"; i.e. with mechanical alloying, an amorphous phase with atomic configuration resembling to the configurations that could be obtained from rapid solidification was achieved. The broadening of the fcc-Al peak around 38° belonging to 111 reflection implies that the fcc-Al crystals were on the order of nano-sizes. It should be noted that there are some extra crystalline reflections in the given XRD pattern. Although, these peaks cannot be precisely resolved from the high background noise on the data, it was attributed to the presence of an IM phase. Detailed information about the IM phase will be given in the forthcoming sections. It should be also stated that the mechanical alloying of the same composition was performed for longer milling times as well, however, it was observed that fcc-Al nanocrystalline phase was persisting despite increased milling time. Thus, considering the fact that extensive milling could also induce nanocrystallization, via deformation-induced crystallization mechanism[191,192], the optimal milling time for the $Al_{88}Sm_7Fe_5Ni_3$ alloy was determined to be 60 hours.

Figure 3.13 shows the BF and SADP of 60 hours mechanically alloyed $Al_{88}Sm_7Fe_5Ni_3$ powder. BF images of the powders had shown distinct dark contrast areas on a featureless matrix. This observation is a clear indication for presence of fcc-Al nanocrystals (giving out a dark contrast due diffraction and chemical means) embedded on amorphous matrix. SAD pattern, given in the inset of Figure 3.13(b), obtained from the same region further confirmed the deduction derived from the BF images. As it can be seen from the figure, SAD pattern consists of diffraction rings of

fcc-Al, together with amorphous halo of the metallic glass phase. There also exist extra diffraction spots that cannot be indexed with fcc-Al reflections. Presence of these reflections were attributed to the existence of unknown, yet unwanted IM phase, which also revealed itself on the XRD pattern. However, investigation of the sample under BF condition had shown that the all crystalline species embedded in the amorphous matrix had spherical morphologies, without revealing any crystalline facets. Thus, from XRD and TEM investigations the mechanically milled alloy was characterized to be an amorphous/nanocrystal composite. The produced powders consist of an amorphous phase matrix with spherical fcc-Al and unknown IM nanocrystals.

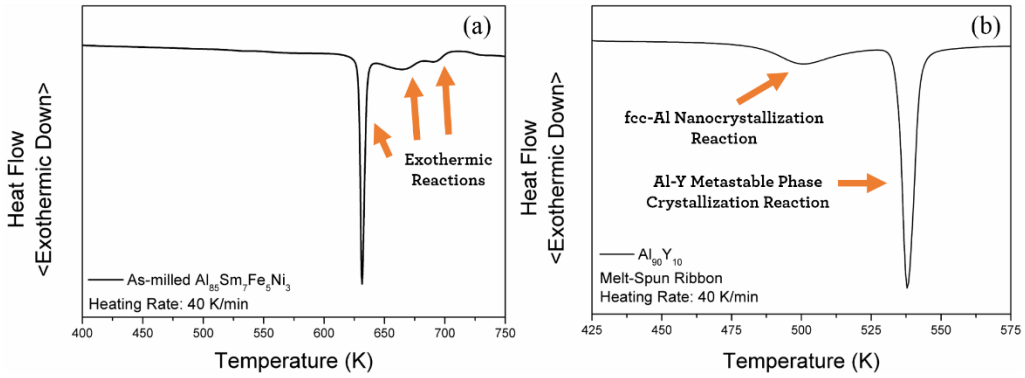

Figure 3.14: DSC traces of **(a)** mechanically alloyed $Al_{88}Sm_7Fe_5Ni_3$ alloy milled for 60 hours, and **(b)** $Al_{90}Y_{10}$ melt-spun ribbon, under isochronal constant heating rate conditions.

Thermal characterization of the mechanically alloyed $Al_{88}Sm_7Fe_5Ni_3$ amorphous/nanocrystalline powder was done using DSC. Figure 3.14.(a) shows the thermal behavior of the powders in isochronal constant heating rate condition. The DSC trace of the $Al_{88}Sm_7Fe_5Ni_3$ amorphous/nanocrystalline powders had shown three exothermic reactions upon isochronal heating. The onset temperature of the initial crystallization for $Al_{88}Sm_7Fe_5Ni_3$ amorphous/nanocrystalline powder was determined to be at 628 K. The shape of the first crystallization event did not resemble to the characteristic temperature and shape of fcc-Al nanocrystalization event that takes in Al-based metallic glass alloys (Figure 3.14.(b))[193–195]. Thus, the first crystallization event on the DSC trace was stated to be crystallization of an unknown IM phase. This

assumption was come out to be true from *in situ* HEXRD experiments, which will be described later. One thing that should be mentioned is that the pre-existence of fcc-Al nanocrystals in the structure could also "screened" the exothermic fcc-Al nucleation from the Al-rich (RE-depleted) regions in the amorphous structure. Due to pre-existence of fcc-Al nanocrystals, the nucleation number density could be lower than an expected value of on the orders of 10^{22} m^{-3},[195,196]. Thus, having low number of nucleation events could release an enthalpy lower than the background noise of the DSC trace, hence, screening the exothermic fcc-Al nanocrystallization event.

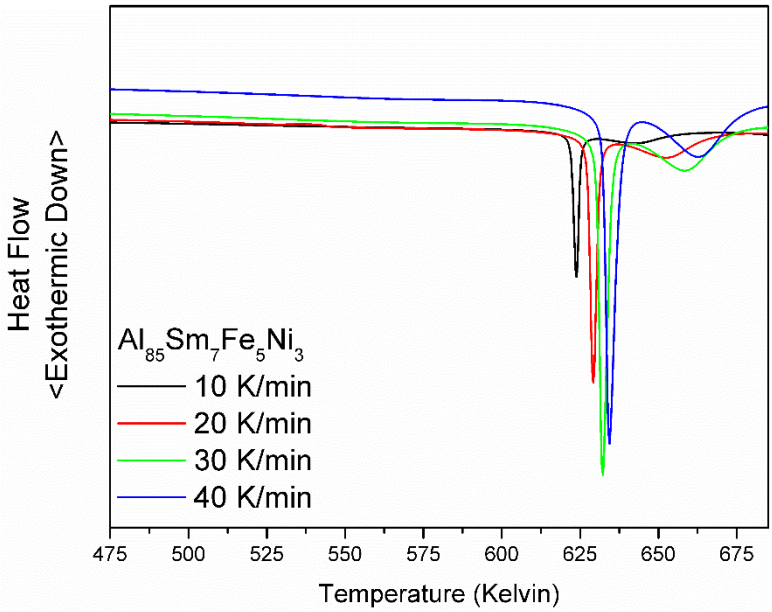

Figure 3.15: DSC traces of mechanically alloyed $Al_{88}Sm_7Fe_5Ni_3$ alloy milled for 60 hours under isochronal constant heating with varying rates.

In order to measure the thermal resistance of the $Al_{88}Sm_7Fe_5Ni_3$ amorphous/nanocrystalline powders, activation energies of fcc-Al nanocrystallization and second exothermic event (at 628 K) were calculated using Kissinger[197] and Ozawa[198] approaches via DSC runs. Kissinger method is one of the most widely used approaches for calculation of activation energies of first order transformations. Kissinger method derives the activation energy of an exothermic reaction by making use of the heating rate dependence of transformation temperatures, with assuming the reaction reaches its maximum rate at the peak temperature[197]. Activation energy of an

exothermic reaction with Kissinger approach can be calculated with the following formula:

$$\ln\left(\frac{\Phi}{T_p^2}\right) = c\ \left(-\frac{E_c}{RT_p}\right) \qquad \text{Equation 3.1}$$

where φ, T_p, and E_c corresponds to heating rate, peak temperature and activation energy, respectively. Activation energy of an exothermic reaction can be calculated by plotting $\ln(\varphi/ T_p^2)$ versus $1/T_p$ and fitting a linear function to the data. The slope of the fitted equation will correspond to the activation energy per gas constant for the exothermic reaction of concern. Ozawa method is quite similar to the Kissinger approach, only differing in their assumptions about the reaction kinetics. In Ozawa method, it was assumed that the reaction order to be constant with varying heating rates[198]. Activation energy of an exothermic reaction with Ozawa approach can be calculated with the following formula:

$$\ln(\Phi) = c\ \left(-\frac{1.052E_c}{RT_p}\right) \qquad \text{Equation 3.2}$$

where φ, T_p, and E_c corresponds to heating rate, peak temperature and activation energy, respectively. Activation energy of an exothermic reaction can be calculated by plotting $\ln(\varphi)$ versus $1/T_p$ and fitting a linear function to the data. The slope of the fitted equation will correspond to the activation energy per gas constant for the exothermic reaction of concern.

Table 3.2: Calculated activation energies for $Al_{88}Sm_7Fe_5Ni_3$ amorphous/nanocrystal composite with Kissinger and Ozawa approaches.

$Al_{85}Sm_7Fe_5Ni_3$	**Activation Energy**	
	Kissinger (kJ/mol)	**Ozawa (kJ/mol)**
fcc-Al	80	85
IM crystallization	419	408

Table 3.3: Activation energies of Al-RE and Al-RE-TM alloys determined using Kissinger and Ozawa methods.

Glass Composition	Kissinger (kJ/mol)	Ozawa (kJ/mol)	Reference
$Al_{90}Sm_{10}$	171 ± 3	171 ± 2	[82]
$Al_{86}Ni_6Y_{4.5}Co_2La_{1.5}$	324 ± 30	333 ± 30	[199]
$Al_{85}Ni_5Y_6Co_2Fe_2$	294 ± 31	303 ± 31	[199]

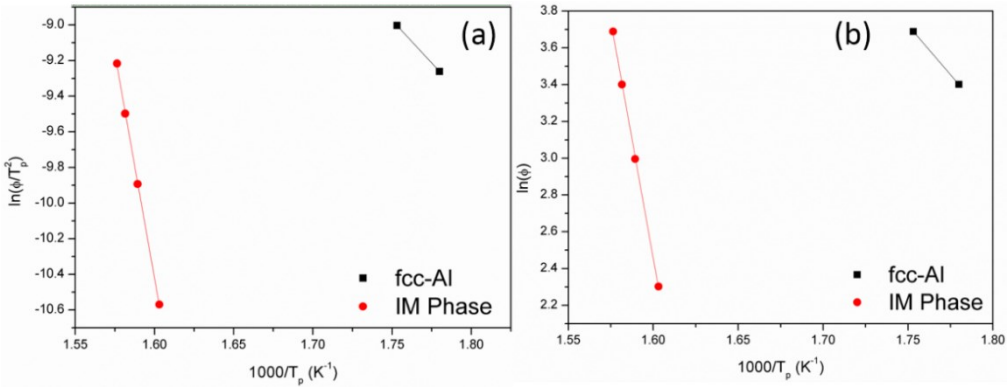

Figure 3.16: (a) Kissinger and **(b)** Ozawa plots for activation energy determination.

For calculation of activation energies of fcc-Al crystallization and second exothermic crystallization event (IM precipitation) DSC isochronal runs with constant heating rates of 10, 20, 30 and 40 K/minutes had conducted. Figure 3.15 shows these DSC traces of $Al_{88}Sm_7Fe_5Ni_3$ amorphous/nanocrystalline powders for various heating rates. By analyzing the data given in the Figure 3.15, activation energies of the mentioned reactions were calculated (Figure 3.16) with both Kissinger and Ozawa approaches and given in Table 4.2. Activation energies of fcc-Al and IM crystallization events were found as 80 and 419 kJ/mole with Kissinger method, and 85 and 408 kJ/mole with Ozawa method, respectively. In order to compare the calculated results with the findings in the literature, activation energies of Al-RE and Al-RE-TM alloys calculated using Kissinger and Ozawa methods were given in Table 4.3. Comparing with the literature data, our result for activation energy of fcc-Al nanocrystallization is quite

low. This result can be interpreted considering two different approaches: by the findings of conventional XRD and TEM observations-wise, and by nucleation kinetics-wise. In the former approach, one should bear in mind the fact that the microstructure of the amorphous/nanocrystalline composite had fcc-Al nanocrystals in the as-milled state after 60 hours of mechanical alloying. From this perspective, for system to reach a metastable equilibrium nanocrystal population in isochronal thermal heating conditions, fcc-Al precipitation is expected to be rather energetically favorable due the parent phase that crystals are nucleating is chemically heterogeneous. The mentioned heterogeneity should not be mistaken with nano-scale chemical heterogeneity in the amorphous state[103], rather a chemical field is present due diffusion fields around the nanocrystals. According to our previous studies on Al-Tb metallic glasses, Wavelength of these chemical fields is known to be on the order of several nanometers in length. Hence, due presence of the chemical heterogeneity on nanometers scale are present, the energy needed for long range diffusion prior to nucleation is therefore depressed. The latter approach for the low activation energy requirement for fcc-Al nucleation is basically looking from a different perspective to the ideas stated for the former approach. From nucleation kinetics-wise, although they have a negative enthalpy of mixing[200], it is known that Al-RE based metallic glasses tend to phase separate in nanometer regime before nucleation event of fcc-Al precipitation[154,171]. Building on the idea stated in the former approach, the diffusion fields around the crystalline species in the amorphous matrix could have undergone a nano-scale phase separation into Al-rich and Al-deficient areas, creating discontinuities on the diffusion fields of the crystals. Hence, again by eliminating the energy required for the long-range diffusion of rejected solute elements on nearly pure-fcc-Al precipitation, the activation energy for nucleation thus could be depressed.

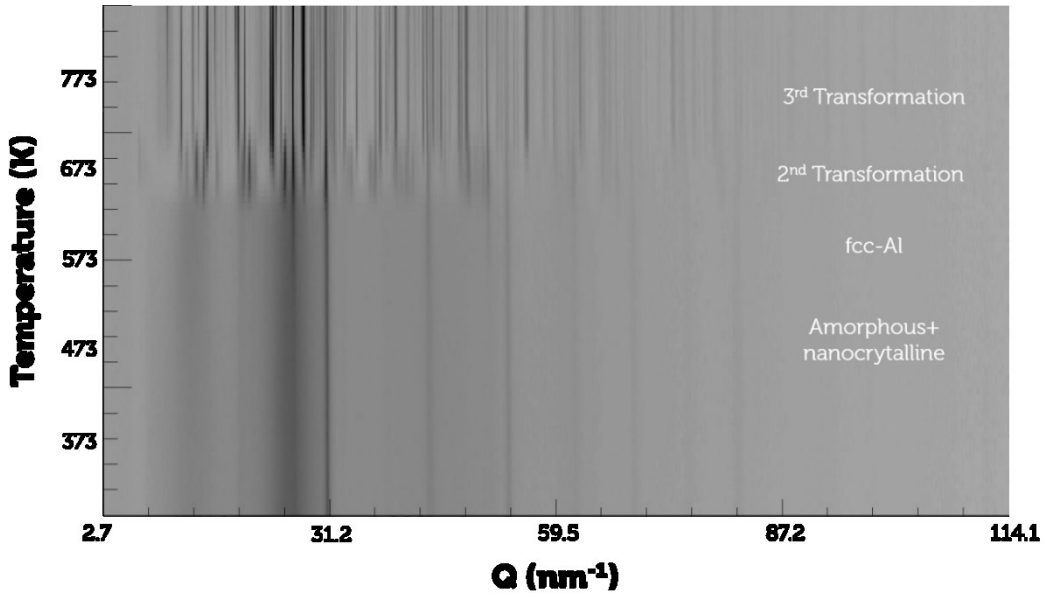

Figure 3. 17: 2D surface plot of *in situ* heating HEXRD results of 60 hours mechanically milled $Al_{88}Sm_7Fe_5Ni_3$ amorphous/nanocrystalline powder.

From consolidation point of view, the result that should be looked for should be precipitation of the IM phases with facets. As explained earlier, the IM phase present on the as-milled state has a spherical morphology, and it was justified as the mentioned phase decreased its surface potential by decreasing its surface area in spherical form[37,44,201]. However, IM crystals that precipitate with the thermal influence could nucleate and grow in faceted manner, due change in the degree and form of the force exerted. Thus, activation energy for the precipitation of the second exothermic thermal event (i.e. IM phase formation) is an important metric for sintering experiments. Activation energy of the IM phase nucleation calculated with Kissinger and Ozawa approaches were found out to be around ~410 kJ/mole (Table 4.2). This is quite a high value, meaning that the energy requirement for long-range diffusion of chemical species is quite high, as well as the to be formed surfaces' energies[201]. Together with a high transformation temperature (at 628 K) and high activation energy requirement of the IM phase, it was concluded that the thermal stability of the as-milled $Al_{88}Sm_7Fe_5Ni_3$ amorphous/nanocrystalline powders are quite high and further appropriate for sintering application.

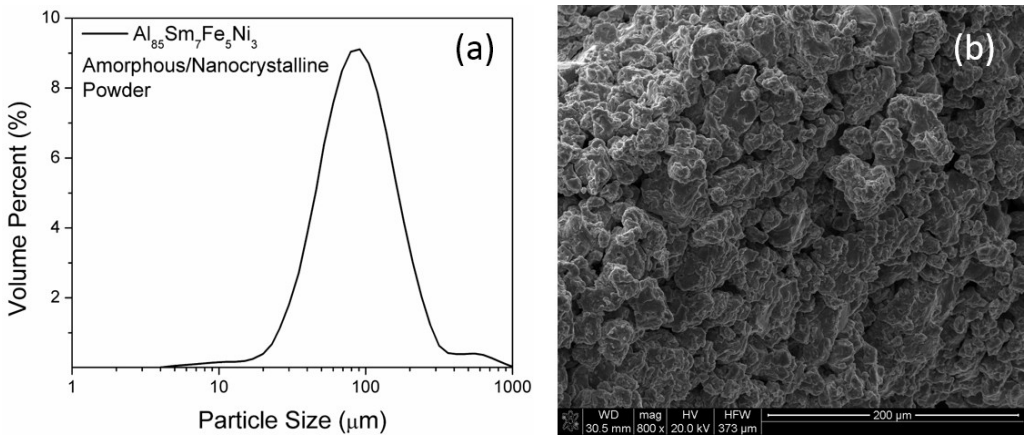

Figure 3.18: (a) Particle size distribution obtained from the particle size analyzer. **(b)** A close-up SEM image from a large as-milled $Al_{88}Sm_7Fe_5Ni_3$ amorphous/ nanocrystalline powder.

Although DSC gives out valuable information about the thermal characteristics of an investigated sample, it lacks revealing information about chemical information of the products of thermally activated reactions. For that reason, $Al_{88}Sm_7Fe_5Ni_3$ amorphous/nanocrystalline powders' thermal behavior was also studied with *in situ* HEXRD in ALBA Synchrotron Lightsource's BL04-MSPD beamline. Figure 3.17 shows the 2D surface plot of the obtained diffraction patterns. In the figure, each collected diffraction pattern is represented as a greyscale line segment, where the intensity variations of each diffraction pattern is converted to greyscale for ease of inspection. *In situ* collected grayscale-line-segment converted diffraction patterns than stacked on top of each other to form a 2D surface plot. When the room temperature data in Figure 3.17 was scrutinized, the IM phase could be clearly observed. Though it should be mentioned that the peaks for the unknown IM phase are quite broad with respect to fcc-Al reflections. Thus, it was an expected result not to clearly observe IM phase reflections with conventional XRD measurements, owing to its relatively low resolution. As compared to synchrotron-based XRD, $Al_{88}Sm_7Fe_5Ni_3$ amorphous/nanocrystalline powders first undergone fcc-Al precipitation at 538 K, then unknown IM phase formation (corresponding to the second exothermic event in DSC traces) was occurred at 626K and the unknown IM phase decomposed into another unknown IM phase (corresponding to the third exothermic event in DSC

traces) at 660 K. The disparity in transformation temperatures measured with DSC and *in situ* HEXRD has two experimental reasons. Firstly, the heating rates in both techniques were different: the heating rate in DSC experiments were 40 K/minute, whereas it was 20 K/minute in *in situ* HEXRD experiments. Secondly, *in situ* HEXRD experiments were done on a rather open atmosphere as compared to DSC experiments. As stated on the Experimental Procedure part, for the *in situ* HEXRD experiments, the powders were filled and sealed into low X-ray absorption capillary tubes and heated using a hot air blower that was placed underneath the sample containing side of the capillary tube, on open atmosphere conditions. As compared with the sample environment in the DSC device, in which samples were heated in an atmosphere controlled furnace with high precision thermocouples, temperature measurement and control in *in situ* HEXRD experiments was expected to be shifted with respect to each other.

The distribution of particle sizes of the as-milled $Al_{88}Sm_7Fe_5Ni_3$ amorphous/nanocrystalline powders were first conducted using Malvern Mastersizer 2000 particle size analyzer device. The particle size distribution of the $Al_{88}Sm_7Fe_5Ni_3$ amorphous/nanocrystalline powder after 60 hours of mechanical alloying is given in Figure 3.18.(a). As the figure reveals, the particle sizes of the as-milled powders have shown a Gaussian distribution, and the mean particle size was determined to be around 100 micrometers. One thing that should be mentioned is that in order to get a statistically significant result, 2 grams of amorphous/nanocrystalline powder was fed into the particle analyzer device for analysis. This was a problematic issue, as stated before, each mechanical milling/alloying trial had yielded around 2 grams of powders, owing to the predetermined ball-to-weight ratio. In other words, conducting particle size analysis would be impractical as single analysis uses all of the yield from the batch. Thus, it was suggested to investigate the morphology and size analysis of powders using optical techniques, such as SEM.

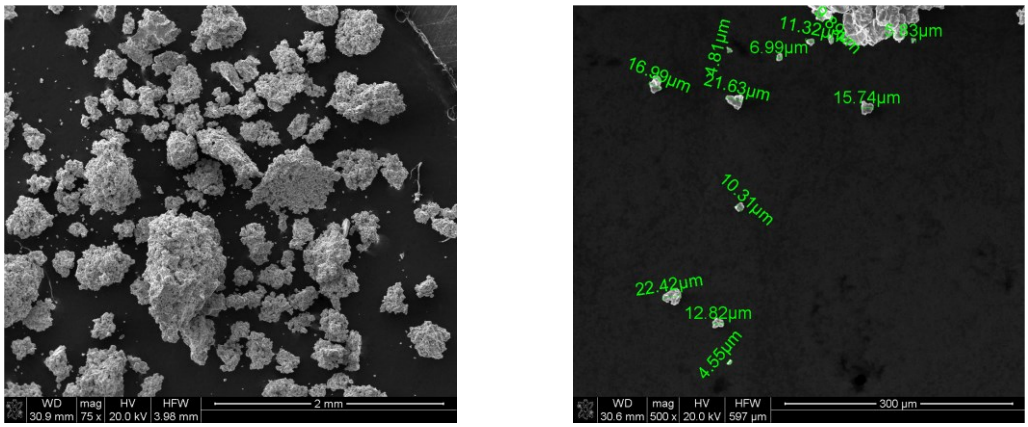

(a) **(b)**

Figure 3.19: SEM images of **(a)** agglomerated and **(b)** small sized as-milled $Al_{88}Sm_7Fe_5Ni_3$ amorphous/nanocrystalline powders.

Figure 3.18.(b) shows a close-up look from a large powder the of as-milled $Al_{88}Sm_7Fe_5Ni_3$ amorphous/nanocrystalline powder. As it can be seen from the figure, particles of sizes around 100 micrometers are actually large agglomerates composed of sub-100 µm particles. As stated earlier, during the milling of powders, exertion of mechanical energy to the powders occurs through successive cold-welding and fracture of the particles. Using this idea, we can say that each sub-100 µm particle is actually a "grain", and these "grains" are forced to intercalate into each other via cold-welding and also gets "fractured". Due stochastic trajectory of the milling agent (i.e. balls), one can say these events are the cause of the agglomeration of the powders during the milling. Furthermore, findings on the literature states that the mean particle size that can be obtained from a milling/alloying procedure is a strong function of the temperature of the milling/alloying experiment. It was stated that particle size is inversely proportional to the milling temperature[54]. The correlation can be explained with the following example: performing milling/alloying in cryogenic environment would result in producing particles with mean sizes around nm, whereas in the current study, as stated in the experimental procedure part, the average temperature attained during the milling/alloying experiments was around 305 K, giving out a mean particle size of ~100 µm. One other evidence for the stated agglomeration hypothesis is the observing the presence of large number of powders having the sizes equivalent to the

powders that forms the agglomerate. SEM images of the agglomerated and small sized powders were given in Figure 3.19. Thus, it was concluded that the $Al_{88}Sm_7Fe_5Ni_3$ amorphous/nanocrystalline powders after 60 hours of mechanical alloying result in agglomerates of ~100 μm that are composed of agglomeration of much smaller particles of 10-30 μm.

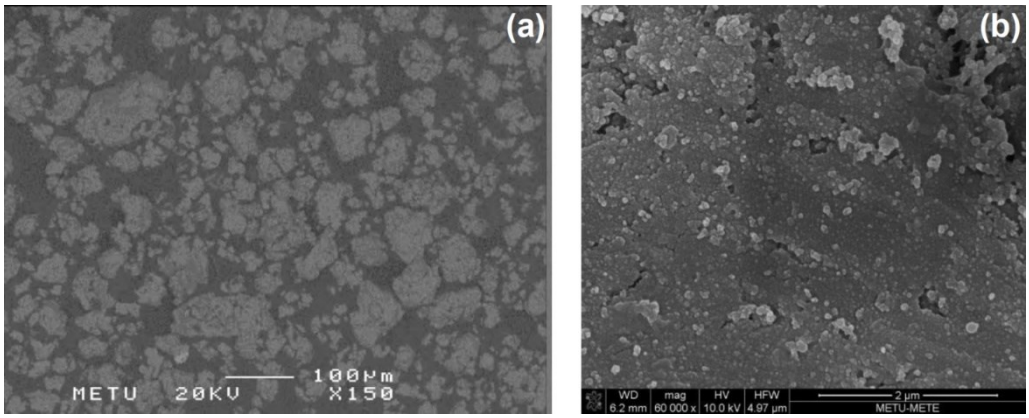

Figure 3.20: (a) Cross sectional and **(b)** close up view of as-milled $Al_{88}Sm_7Fe_5Ni_3$ amorphous/nanocrystalline powders.

The intergranular structure of the agglomerates were investigated by embedding particles into epoxy resin followed by metallographic preparation. SEM images of the intergranular structure of the $Al_{88}Sm_7Fe_5Ni_3$ amorphous/nanocrystalline powders were given in Figure 3.20. As it can be seen from the figures, it can be inferred that the agglomerates are quite rigid, formed nearly by intermixing of two smaller particles, as the image reveals quite low grain boundary area.

Hardness measurements were conducted on the powders that were embedded into the epoxy resin and metallographically prepared. The mean hardness of the $Al_{88}Sm_7Fe_5Ni_3$ amorphous/nanocrystalline powders were found as 154 Hv with a standard deviation of ±63. The observed value was found not the be satisfactory, as in our previous studies in $Al_{90}Tb_{10}$ melt-spun ribbons, hardness values as high as 280 Hv was reached in amorphous/nanocrystalline composite form[166]. However, one should consider the statistical significance of the results with the high standard deviation from the mean value. The reason for the high standard deviation in hardness results was attributed to

the effect of embedding powders into the epoxy resin. It was known that performing a hardness measurement on a material that is not supported by a material with high rigidity could cause problem, as a particle should not move whilst performing an indentation. For that reason, hardness measurements made on self-supporting green compacts of the $Al_{88}Sm_7Fe_5Ni_3$ amorphous/nanocrystalline powders will be given in the following sections of the current chapter, for the re-evaluation of the given hardness measurements.

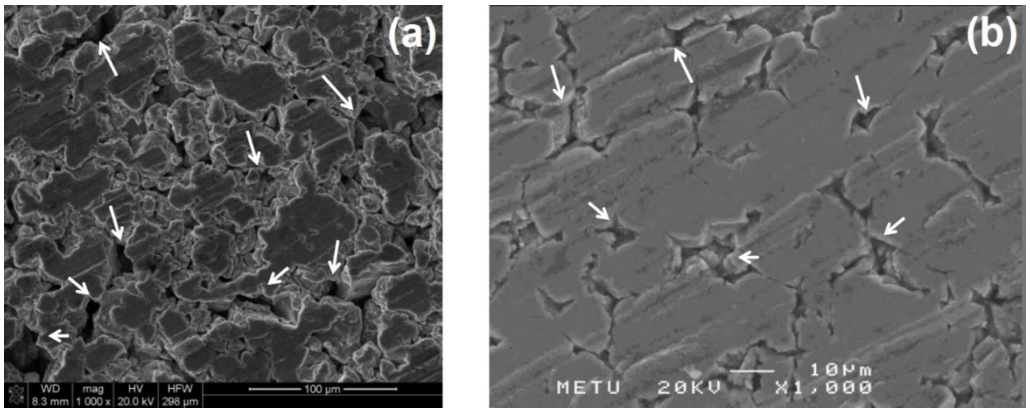

Figure 3.21: SEM images of green compacts produced with applied loads of **(a)** 22 tons and **(b)** 50 tons.

3.4.2 Consolidation with How Pressing and Sintering

All of the trials for bulk sample production were performed with $Al_{88}Sm_7Fe_5Ni_3$ amorphous/nanocrystalline powders. The production parameters were optimized and its microstructural and thermal behaviors were characterized, as explained in the previous section. As stated in the Experimental Procedure section, green compacts of amorphous/nanocrystalline powders were produced via cold pressing by a uniaxial hydraulic press in cylindrical shape. Due novelty of $Al_{88}Sm_7Fe_5Ni_3$ amorphous/nanocrystalline powders, there are no data regarding the amorphous density of the alloy. Thus, relative densities of the produced green compacts were compared with the theoretical density of crystalline counterpart of the mentioned alloy, calculated as 3.8 g/cm^3.

For the first trial, a green compact of 1 mm height and 15 mm in diameter was obtained under 22 tons of load from $Al_{88}Sm_7Fe_5Ni_3$ amorphous/nanocrystalline powders. The density of the green compact was determined as 2.74 g/cm^3. Considering the crystalline density of $Al_{88}Sm_7Fe_5Ni_3$ alloy, a 72% densification was achieved with the cold pressing to form green compact. This result was considered to be unsatisfactory, as it is around 10-15% lower than the aimed densification. The reason for aiming a higher densification is that denser the green compact, higher the final density of the sintered sample, with least number of defects, such as porosity, etc. Owing to achieved densification was insufficient, latter trial was repeated with applications of 50 tons of load. Eventually, the densification of the new green compact was determined to be 85%, with a density of 3.22 g/cm^3. Surface morphologies of the mentioned two green compacts were presented in Figure 3.21. For the purpose of accurate comparison, SEM images of the two green compacts in Figure 3.21 were obtained with the same magnification. The figure reveals the effect of applied load on the compaction of the green compacts; as it can be seen from Figure 3.21, increasing the applied load from 22 to 50 tons had decreased the number of porosities and made its distribution scarcer. Beside the porosity scarcity, inter-powders distances became much lower in the high-load counterpart, causing the ~15% increase in the density.

Prior to sintering of the produced green compacts, to test the legacy of thermal stability, thermal analyses on the samples were done by isochronal DSC scan. As Figure 3.22 reveals, green compacts had shown the thermal behavior as the as-milled $Al_{88}Sm_7Fe_5Ni_3$ amorphous/nanocrystalline powders. Analyses on features of thermal behavior, such as crystallization temperatures and their corresponding enthapies were also found to be nearly equal. Thus, it was concluded that the effect of cold-pressing on the structure of the material is either none or negligibly minute, within the error of DSC experimentation.

Initial trials for sintering of the green compacts were done using DSC. The purpose for choosing such a route is that DSC provides fair atmospheric control on its furnace, together with its capability of revealing the operating phase transformations temporally. Considering the initial crystallization temperature of 628 K, observed for

both as-milled and as-pressed material, isothermal hold temperatures were chosen as 573, 583 and 593 K. In all isothermal holds, loaded material and the reference were first heated up to the isothermal hold temperature with 100 K/min and heat flow versus time data was recorded.

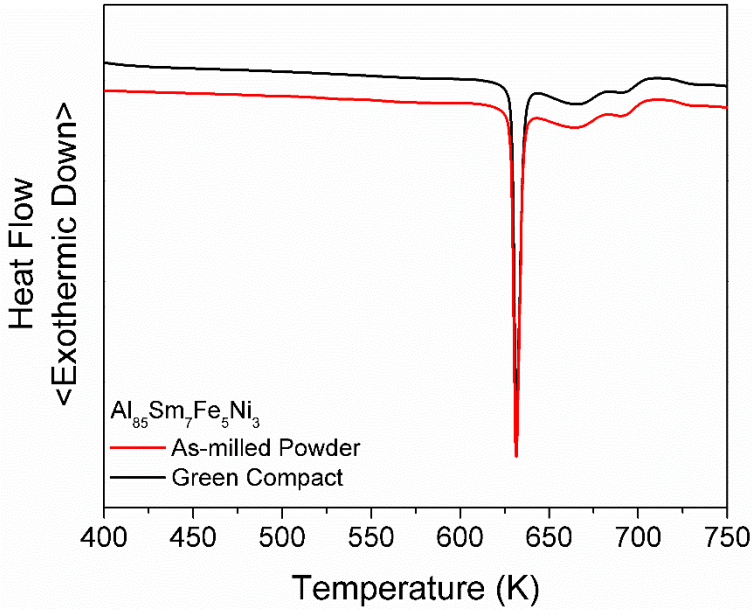

Figure 3.22: Isochronal DSC scans of $Al_{88}Sm_7Fe_5Ni_3$ amorphous/nanocrystalline alloy in as-milled and as-pressed conditions.

First the effect of applied load during cold pressing on sintering was tested by sintering green compacts produced with 22 and 50 tons of applied loads, and presented in Figure 3.23. Obtained isothermal DSC traces had shown no correlation between the applied load whilst cold pressing on isothermal phase transformation characteristics, as both samples had undergone crystallization reactions within 15 minutes at 593 K. Thus, together with the isochronal DSC data, it was further concluded that the effect of applied pressure on cold pressing has either negligible or no effect on thermal behavior of the green compacts.

Bearing the fact in mind that metallurgical bonding is enhanced with increased applied pressure on cold pressing, the sintering trials were continued with the samples cold pressed with applied load of 50 tons. Figure 3.23 shows thermal events occurring through the isothermal DSC holds at 573, 583 and 593 K for green compacts produced

50 tons of applied load. Deduced from the given data, the time allowed for sintering (i.e. time elapsed for crystallization reaction to take place) at isothermal hold temperatures of 573, 583 and 593 K were found as 90, 40 and 15 minutes, respectively. As 573 K isothermal hold provides an adequate temporal range of 90 minutes for the sintering, it's chosen as the isothermal hold temperature for the sintering trials.

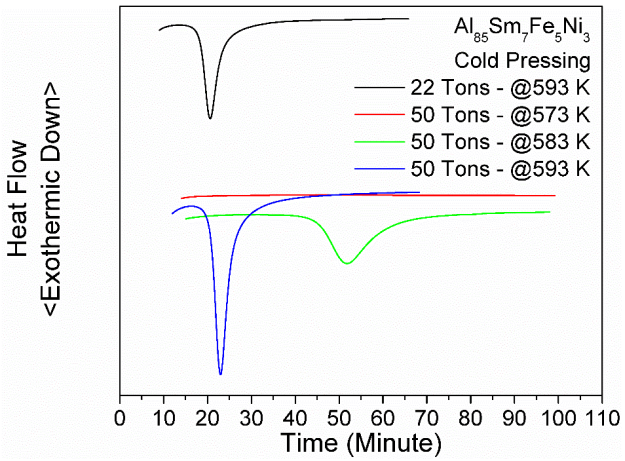

Figure 3.23: Isothermal DSC holds of produced green compacts under applied loads of 22 and 50 tons.

Sintering trials were started with green compacts of $Al_{88}Sm_7Fe_5Ni_3$ amorphous/nanocrystalline alloy that were sintered at 573 K for 60 and 90 minutes. Densities sintered samples for 60 and 90 minutes were determined as 3.5 and 3.65 g/cm^3, corresponding to 92% and 96% compaction. SEM images of sintered samples at 573K for 60 and 90 minutes were given in Figure 3.24. Post-sintering investigation of $Al_{88}Sm_7Fe_5Ni_3$ amorphous/nanocrystalline green compact sintered at 573 K for 60 minutes had revealed uneven and irregular sintering behavior. Meaning that, the surface of the sintered green compact was composed of regions with fine metallurgical bonding, in which porosities were small and round shaped, indicating well sintering (Figure 3.24.(a)), together with regions of poor metallurgical bonding showing large porous areas (Figure 3.24.(b)). The stated problem was found not to be correlated with sintering time, as same problem was also seen in the 90 minutes sintered sample. Keeping in mind that the applied load on cold pressing was the same for both samples, it was concluded that the reason behind non-uniform metallurgical bonding in the

materials stems from the non-uniform load distribution on the powders during the cold pressing process. Due stated reason, several precautions were taken in the cold pressing step, such as:

i. Powders were inserted into the die in a more homogeneously distributed fashion.
ii. New dies with delicate surface finishes were started to be used.
iii. Obliquity of the metal piece that the die was placed was adjusted with a water gage before every cold pressing trial.

For the next sintering trials, it was observed that the stated precautions were become a remedy, and the state problems were not observed for the sintering trials that are yet to be presented.

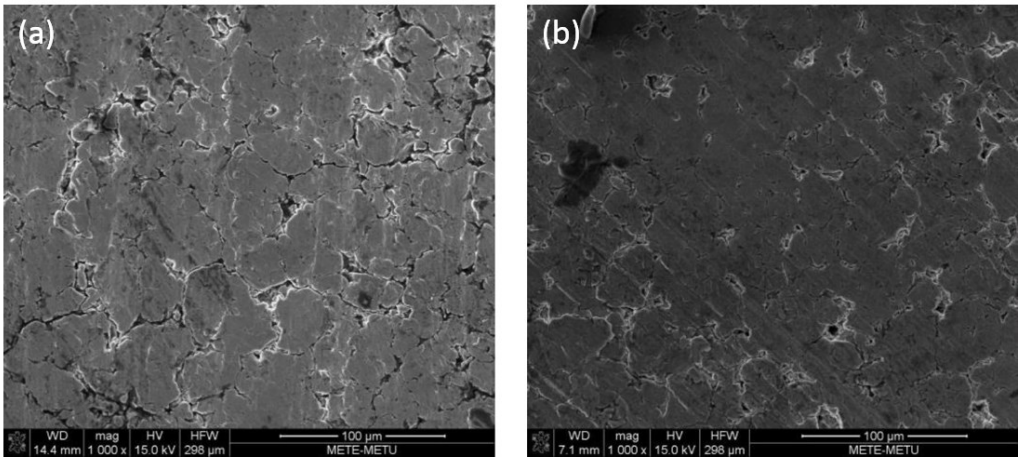

Figure 3.24: Surface images of $Al_{88}Sm_7Fe_5Ni_3$ amorphous/nanocrystalline compacts in the **(a)** as-pressed and **(b)** as-sintered state.

In the light of the stated solutions for the unequal load distribution problem, the sintering trial of $Al_{88}Sm_7Fe_5Ni_3$ amorphous/nanocrystalline green compact produced with 50 tons of applied load was repeated. The green density of the compact was determined as 3.5 g/cm^3, which corresponds to 91% compaction. The produced green compact was sintered with isothermal DSC hold at 573 K for 60 minutes, under provided atmosphere control. The density of the sintered compact was determined as

3.7 g/cm^3, corresponding to 97% compaction. Unlike the results given above, SEM investigation was conducted on the sintered sample (Figure 3.25.(b)) had shown well and evenly distributed metallurgical bonds throughout the consolidated samples surface, with a depression in the sizes and homogeneity for the distribution of the pores, as well.

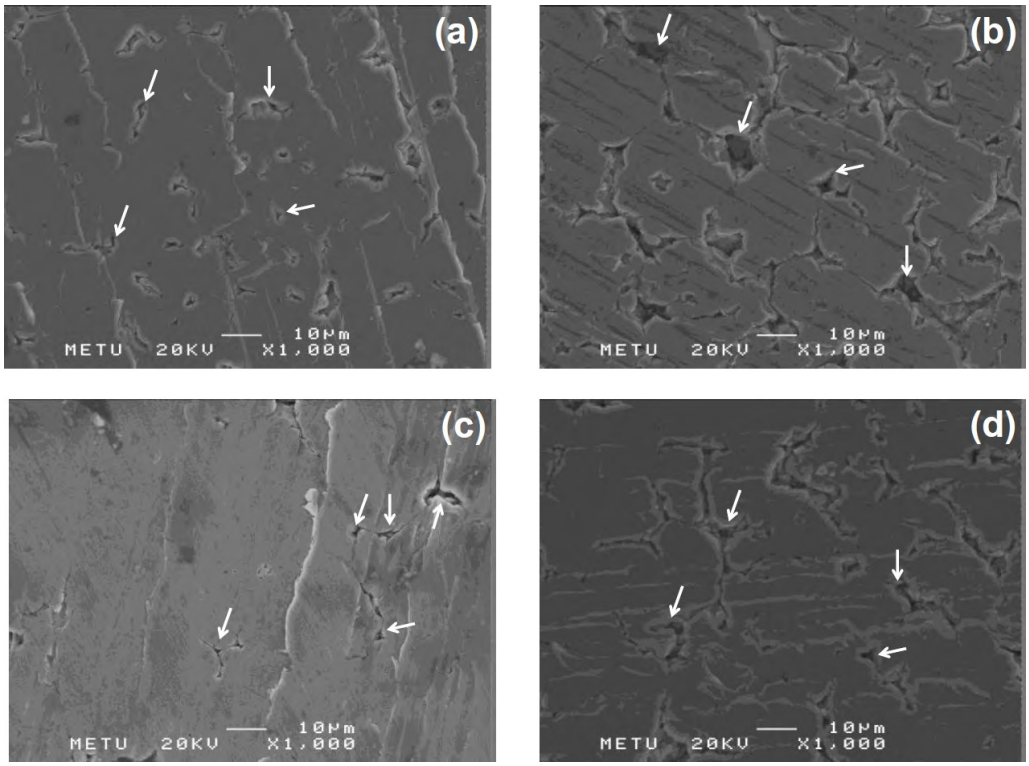

Figure 3.25: Surface images of $Al_{88}Sm_7Fe_5Ni_3$ amorphous/nanocrystalline samples produced with 50 tons of applied load, sintered at 573 K for **(a-b)** 60 minutes and **(c-d)** 90 minutes. Arrows indicate porosities.

For determination of the mechanical properties, compression tests were performed on the produced sintered compacts. Compression tests of the consolidated samples were done at room temperature according to ASTM E-9 standard[202]. To comply with the mentioned testing standard, cylinders of 3 mm in diameter were cut from the consolidated samples, whose dimensions in the as-sintered condition were 15 mm in diameter with 1.5 mm in height. Albeit the tediousness of the process with regular sample preparation processes, cutting of the cylinders were done using ultrasonic disc

cutter, a TEM sample preparation device usually used for brittle materials. Lateral surface of the cut cylinders were grinded with sand paper to remove any kind of surface roughness occurred after the cutting procedure. According to the ASTM standard, strain rate in compression was determined as 0.01 mm/mm.minutes for the first compression trials.

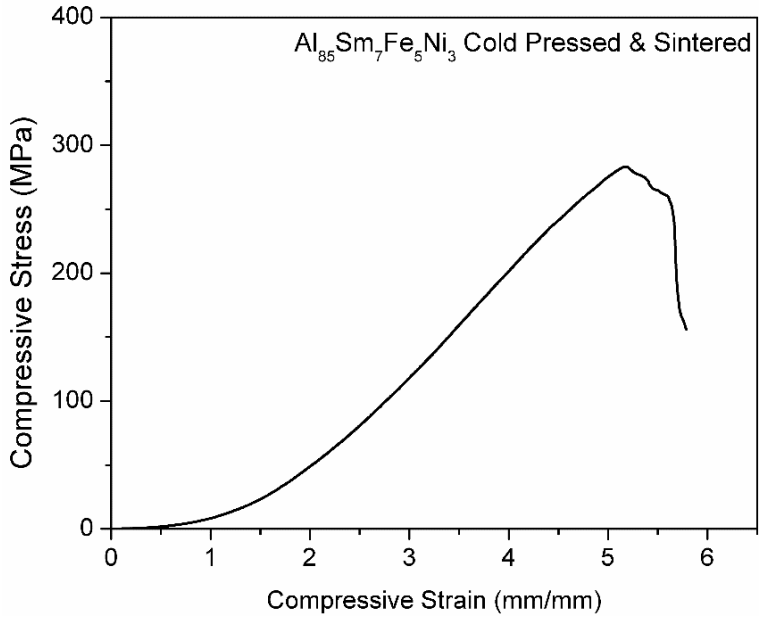

Figure 3.26: Compression test result of $Al_{88}Sm_7Fe_5Ni_3$ amorphous/nanocrystalline sintered compact, prepared according to ASTM E-9 standard.

Compression test result of $Al_{88}Sm_7Fe_5Ni_3$ amorphous/nanocrystalline sintered compact is given in Figure 3.26. The compression strength of the material was determined as 280 MPa. The sample had fractured under compression as it reached to its maximum elastic strain. This phenomenon is typical of the amorphous materials, regardless of their bonding nature[187], as most of the materials having amorphous structure fails by the time its yield strength is reached[203]. Figure 3.27 represents the fracture surface(s) of the sample after failing in the compression test. As it can be seen from the Figure 3.27.(a), the crack that lead to the failure of the sample had started from its edge, and propagated through the sample towards its central axis. Figure 3.27.(b) shows the SEM image of the fracture surface of the compressed sample. The stairway-like structure implies that the applied stress did not dispersed evenly in the

microstructure, rather seems to be accumulated in several regions causing pattern, leading to brittle fracture. The stairway-like pattern is known to be called as "shear banding", and they are characterized as structural special features that accumulate the applied stress in narrow regions[203,204].

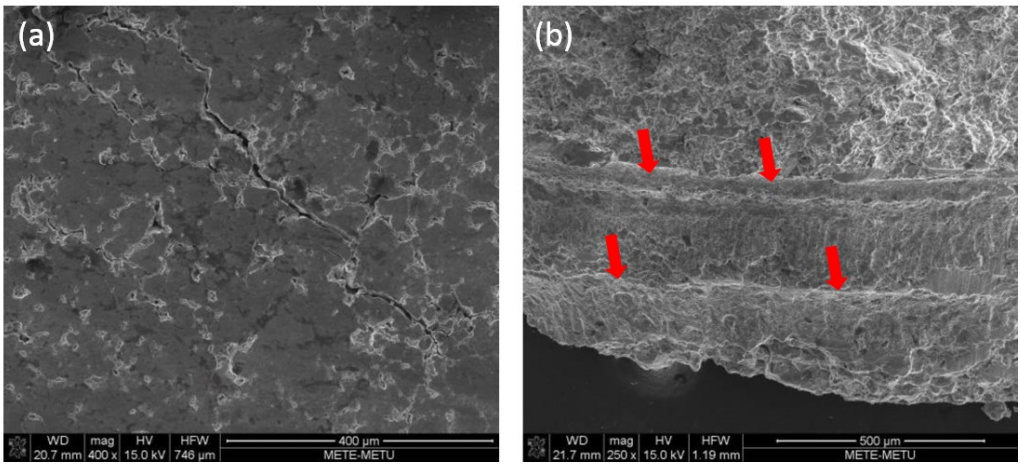

Figure 3.27: (a) Lateral view and **(b)** fracture surface of $Al_{88}Sm_7Fe_5Ni_3$ amorphous/nanocrystalline sintered compact, prepared according to ASTM E-9 standard.

Aforementioned previously, compression test samples were cut from the sintered compact with the use of ultrasonic disc cutter device. Further, it has been stated that the lateral surface of the cylinder was grinded with sand paper to remove the ridges to eliminate stress concentration centers. However, as post-mortem SEM images of the sample given in Figure 3.27.(a) shows that the crack that had led to failure of the sample had started from the lateral edge of the cylindrical sample. Because of the unexpected crack initiation from the samples lateral surface, observed mechanical properties were found to be below the expected values. The used standard justifies its strict geometrical constraints by aiming to determine the yield strength and maximum compressive strength of the material, however, in the case of solely yield strength determination, the stated geometrical constraints are said to be overruled[202]. Thus, in the light of the obtained results, the compression test was repeated directly on the as-produced, large $Al_{88}Sm_7Fe_5Ni_3$ amorphous/nanocrystalline sintered compacts, in order to minimize the surface defects.

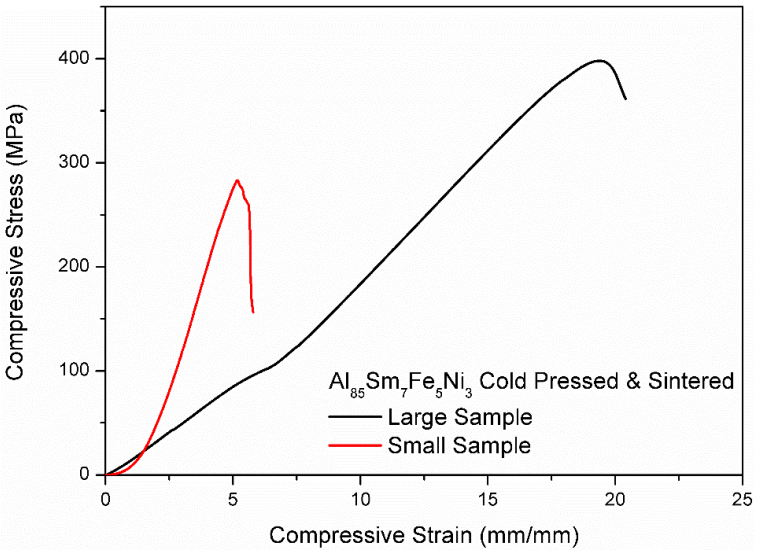

Figure 3.28: Comparative compression test result of $Al_{88}Sm_7Fe_5Ni_3$ amorphous/nanocrystalline of cut and large samples.

Figure 3.28 shows the compression test result of the $Al_{88}Sm_7Fe_5Ni_3$ amorphous/ nanocrystalline sintered compact. $Al_{88}Sm_7Fe_5Ni_3$ amorphous/nanocrystalline sintered compact in as-sintered condition and morphology had shown 400 MPa of compressive stress. One could see the clear difference in the compressive strength loss due to sample geometry. A striking difference that comes to eyes it the quite high compressive strain and low Young's Modulus showed by the large sample, as compared to cylindrical sample. However, though the obtained result could be true for the large sample, it may not reflect the true material property of the sample, as the standard states[202]. Thus, comparison of respective compressive strains and Young's Moduli could be misleading. Comparison of the compressive stresses of the samples exclusively is more accurate.

3.4.3 Consolidation with Warm Pressing

Ex-situ composite formation is one of the most widely used technique of enhancing the strength and strain response of the metallic glasses. The term "ex-situ composite formation" can be explained as introduction of non-soluble second phase particles, such as ceramic or refractory metals, into the structure for improvement of materials properties[205,206]. This technique should not be confused with "in-situ composite

formation", in which, conversely, a composite structure is formed upon application of external forces, e.g. thermal devitrification[195,207] or deformation induced crystallization[192,208]. To make us of the enhancement effect of secondary phase addition to the produced amorphous/nanocrystalline powders via ex-situ composite formation, in this part of the study, the effect of introduction of micrometer sized crystalline Al powders into $Al_{88}Sm_7Fe_5Ni_3$ amorphous/nanocrystalline powders was investigated.

Figure 3.29: An ex-situ composite sample, produced with warm pressing.

The results of this study will reflect only ex-situ composite formation effect on the $Al_{88}Sm_7Fe_5Ni_3$ amorphous/nanocrystalline samples, as the results presented in Section 3.2 had shown that samples did not undergo any in-situ phase transformations upon pressing. Thus, pure Al powders were added mechanically to synthesized amorphous/nanocrystal powders to form ex-situ composites. Consolidation of the ex-situ composite powders were done using the warm pressing setup. Powders were pressed using the dies having 10 mm diameters; the final dimensions of all warm pressed samples are 10 mm in diameter and 2 mm in height. For extended information about the warm pressing procedure, please consult to the Experimental Procedure section.

The warm pressing experiments were started with the production of bare $Al_{88}Sm_7Fe_5Ni_3$ amorphous/nanocrystalline powders, in order to compare the results of the warm pressing route to the previously represented results of cold pressing and sintering. Warm pressing of the samples was performed with an applied load of 22 tons at 493 K for 10 minutes. It was observed that after the heating unit reached its set temperature of 493 K, the temperature measurements made on the die were found to

fluctuate ±10 K during the process. Photograph of the consolidated sample produced with warm pressing is given in Figure 3.29.

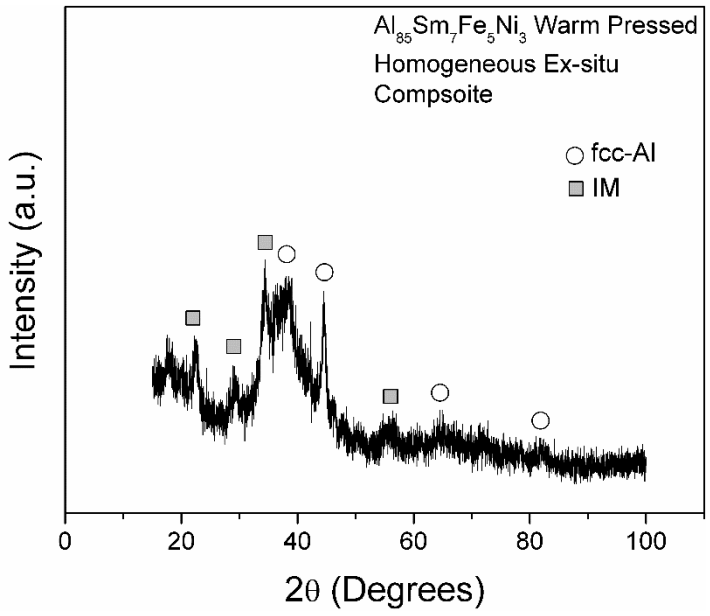

Figure 3.30: XRD pattern of the warm press consolidated $Al_{88}Sm_7Fe_5Ni_3$ amorphous/nanocrystalline alloy.

Density of the warm press consolidated $Al_{88}Sm_7Fe_5Ni_3$ amorphous/nanocrystalline alloy was found as 3.5 g/cm^3 that corresponds to a densification of 92%. Compared to its cold pressed and sintered counterpart, density of the warm press consolidated sample corresponds to the lowest density that was attained for cold pressed and sintered samples. The reason for relatively low density achievement is that the warm pressing was done with an applied load of 22 tons on the sample; likewise, the lowest observed density for the cold pressed and sintered product was also produced with the same applied load. Retrospectively, the densification was found to increase by increasing the applied load on cold pressing from 22 to 50 tons. However, due to the size limitations of the high load capacity hydraulic press, the warm pressing setup could not be integrated with it.

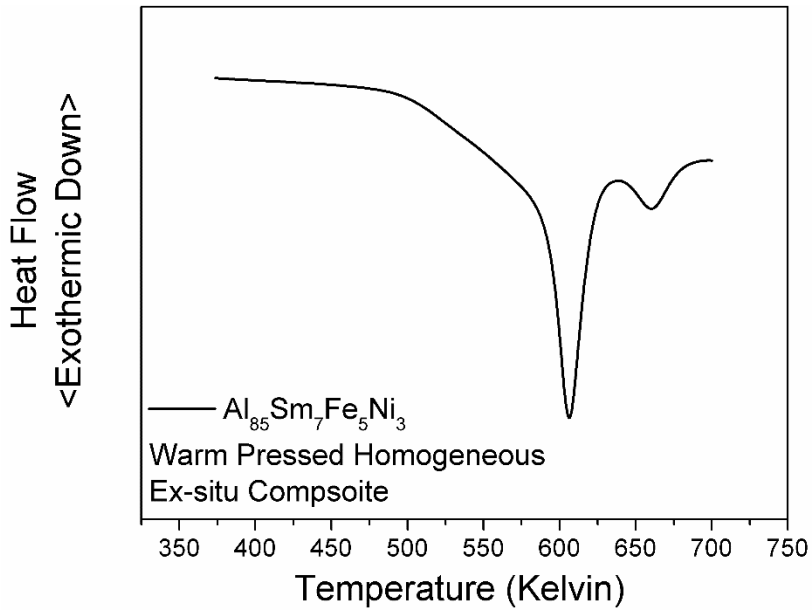

Figure 3.31: Isochronal DSC trace of the warm press consolidated $Al_{88}Sm_7Fe_5Ni_3$ amorphous/nanocrystalline alloy.

XRD pattern of the warm pressed $Al_{88}Sm_7Fe_5Ni_3$ amorphous/nanocrystalline consolidate is given in Figure 3.30. Diffraction pattern had shown that the microstructure of the consolidate consists of amorphous matrix, fcc-Al nanocrystals and unknown Al-Sm IM phase. The peak positions of the mentioned unknown IM phase were found to correspond to the IM phase that was characterized in the as-milled state of the $Al_{88}Sm_7Fe_5Ni_3$ amorphous/nanocrystalline powders. Due to thermal excitement, IM phase crystals were found to grow in size, as its Bragg reflections became more intense and narrow. To verify the existence of the amorphous phase in the microstructure, an isochronal DSC run was performed on the warm pressed consolidate. As it can be seen from Figure 3.31, the warm pressed $Al_{88}Sm_7Fe_5Ni_3$ amorphous/nanocrystalline consolidate had shown the same thermal events that the as-milled powders had shown. In Section 3.1, these thermal events were determined to as fcc-Al nanocrystallization and unknown IM phase crystallization. As these phase transformations were known to be crystalline phase precipitations from the amorphous matrix, it was concluded that the amorphous phase had still retained after the warm pressing procedure.

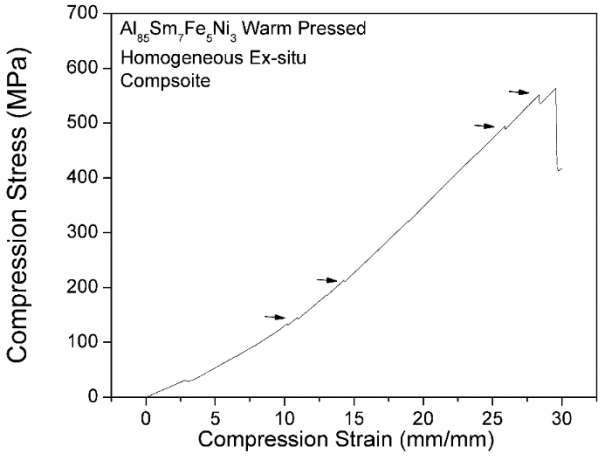

Figure 3.32: Compression test result of the warm press consolidated $Al_{88}Sm_7Fe_5Ni_3$ amorphous/nanocrystalline alloy.

Compression test result of the warm pressed $Al_{88}Sm_7Fe_5Ni_3$ amorphous/nanocrystalline consolidate is given in Figure 3.32. The compression strength of the material was found as 550 MPa. Compared to its cold pressed and sintered counterpart, warm pressed consolidate had shown a 100 MPa increase in compression strength. However, warm pressed consolidate sample had failed after passing the elastic regime, similar to cold pressed and sintered sample, without showing any ductility. One eye catching feature of the given stress-strain curve is the presence of sudden load drop events on the elastic regime, indicated by arrows on Figure 3.32. These sudden load drops are called as "pop-in" events[203,209] and they are known to be the manifestations of shear band formation in the amorphous/nanocrystalline structure[67,204]. The obtained compression test results indicate that the shear bands are frequently formed in the elastic regime to accommodate the applied strain, however, sudden failure after passing by the yield strength implies that nucleation rate of shear bands were not high enough for material to deform plastically beyond yielding, hence leading to brittle fracture. Figure 3.33 presents the post-mortem SEM images of the compression test sample. SEM analysis on the fractured sample had revealed that the crack that lead to the failure of the sample was initiated and propagated between the lesser sintered grains of powders in the consolidate. Investigations made on the fracture surface of the compression sample

had revealed the presence of shear bands on the surface of the sintered powders that had accommodated deformation in the elastic regime, which manifested itself as pop-in events on the stress-strain curve (Figure 3.33.(b)).

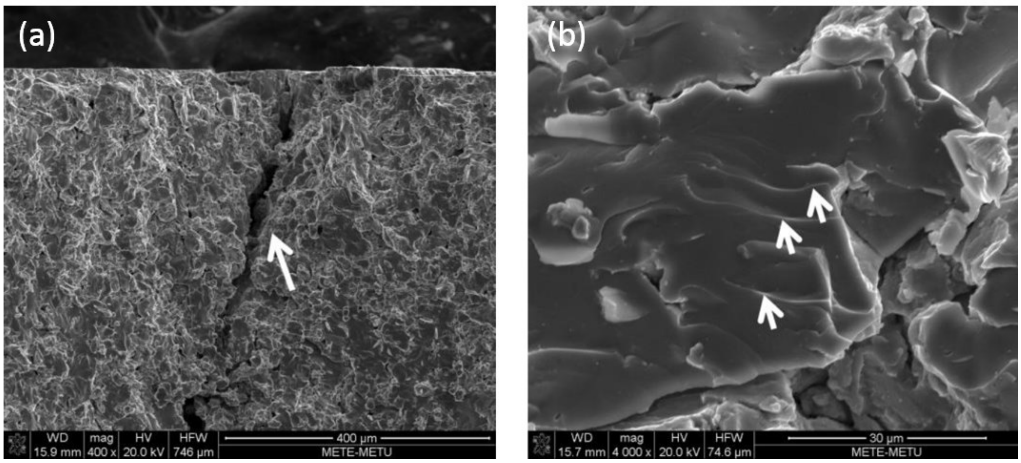

Figure 3.33: SEM images of **(a)** crack propagation and **(b)** shear bands on the grains in the compression test sample of the warm press consolidated $Al_{88}Sm_7Fe_5Ni_3$ amorphous/nanocrystalline alloy. Arrows in Figure **(b)** indicates the shear bands on a grain.

As stated before, the main objective of the study presented in this section is to investigate the effect of ex-situ composite formation on the microstructure and mechanical properties of $Al_{88}Sm_7Fe_5Ni_3$ amorphous/nanocrystalline alloy. The inspiration was drawn from the usage of pure Al powders in warm pressing of crystalline Al alloys, which acts as a binder and increases the density of warm pressed parts[210]. In the initial trial, $Al_{88}Sm_7Fe_5Ni_3$ amorphous/nanocrystalline powders were homogeneously mixed with pure Al powders of 30% w.t., with respect to synthesized powders weight. XRD pattern collected from the warm pressed amorphous/nanocrystalline alloy with pure Al addition is given in Figure 3.34. In the presented diffraction pattern, reflections from amorphous/nanocrystalline phases were highly suppressed by the crystalline reflections from the pure Al powders, due enormous scattering capability difference between amorphous and/or nanocrystalline phases and powders of high crystallinity[211]. Nevertheless, presence of pre and side

peaks, and diffuse amorphous hump can be clearly observed together with the crystalline reflections of pure Al.

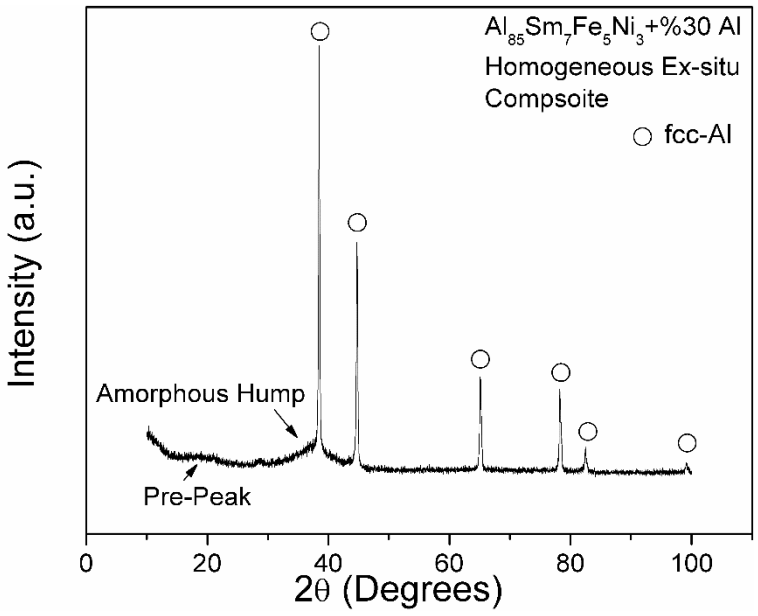

Figure 3.34: XRD pattern of warm pressed $Al_{88}Sm_7Fe_5Ni_3$ amorphous/nanocrystalline with 30% pure Al added consolidate.

The density of the $Al_{88}Sm_7Fe_5Ni_3$ amorphous/nanocrystalline powders were mixed with pure Al powders of 30% w.t. consolidate was determined as 3.4 g/cm^3, corresponding to 97% compaction. When the obtained compaction value for the ex-situ composite consolidate is compared with warm pressed, and cold pressed and sintered $Al_{88}Sm_7Fe_5Ni_3$ amorphous/nanocrystalline consolidates (which were 92% and 97%), it can be said that addition of pure Al to synthesized amorphous/nanocrystalline enhances its ability to consolidate under warm pressing conditions. Hence, one can conclude that the pure Al addition to $Al_{88}Sm_7Fe_5Ni_3$ amorphous/nanocrystalline powders acts positively on the compaction of the powders.

Mechanical behavior of the warm pressed ex-situ composite with 30% pure Al was determined with compression test, and given in Figure 3.35. Compressive strength of the warm pressed consolidate was determined as 450 MPa. It should be noted that, a glimpse of ductility was observed for the first time in the compression of ex-situ consolidate. Fracture analysis of the ex-situ consolidate is given in Figure 3.36. As the

figure reveals, fracture of the ex-situ consolidate had occurred through the crack propagation on the boundaries of the sintered amorphous/nanocrystalline grain, similar to the fracture behavior of cold pressed & sintered and warm pressed consolidates. In the given SEM image, light shaded areas corresponds to pure Al grains, whereas dark shades regions correspond to amorphous/nanocrystalline grains. Careful investigation of the warm pressed ex-situ consolidate has revealed different sintering behavior on each component of the composite structure. It was observed that the pure Al bearing regions had formed good metallurgical bonds between the powders, as nearly no porosity was observed in these regions. Further, as compared to pure Al regions, $Al_{88}Sm_7Fe_5Ni_3$ amorphous/nanocrystalline regions had shown relatively poor metallurgical bonding, albeit the consolidate of concern had shown the best attained sintering that had been seen throughout the study, with respect to previously given results.

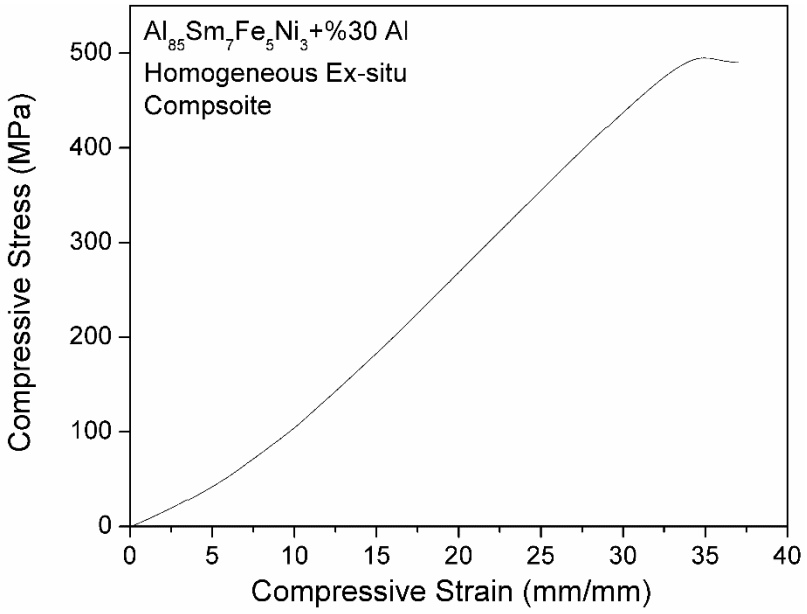

Figure 3.35: Compression test result of the warm pressed $Al_{88}Sm_7Fe_5Ni_3$ amorphous/nanocrystalline with 30% pure Al added consolidate.

The reason behind the improved sintering of the $Al_{88}Sm_7Fe_5Ni_3$ amorphous/ nanocrystalline powders had revealed itself on Figure 3.36.(b): as mentioned before, pure Al addition was expected to act as a binder between the synthesized amorphous/

nanocrystalline powders, and the SEM investigation had revealed that they actually did act like a binder between the amorphous/nanocrystalline powders by filling the porosities left between the powders, increasing the compaction. As stated before, usage of pure elemental powders of aluminum and copper are widely used additives to ease the sintering of low alloy aluminum alloys[210]. The mechanism for enhancement of sintering operates as pure elemental additives wet the low alloy powders and aid the metallurgical bonding that is taking place in sintering. Analogously, the synthesized amorphous/nanocrystalline powder bears high amount of aluminum (i.e. 85% a.t.), and as seen from the SEM images, pure Al powders seem to wet amorphous/nanocrystal powder grains and enhanced the sintering ability of the whole ex-situ composite.

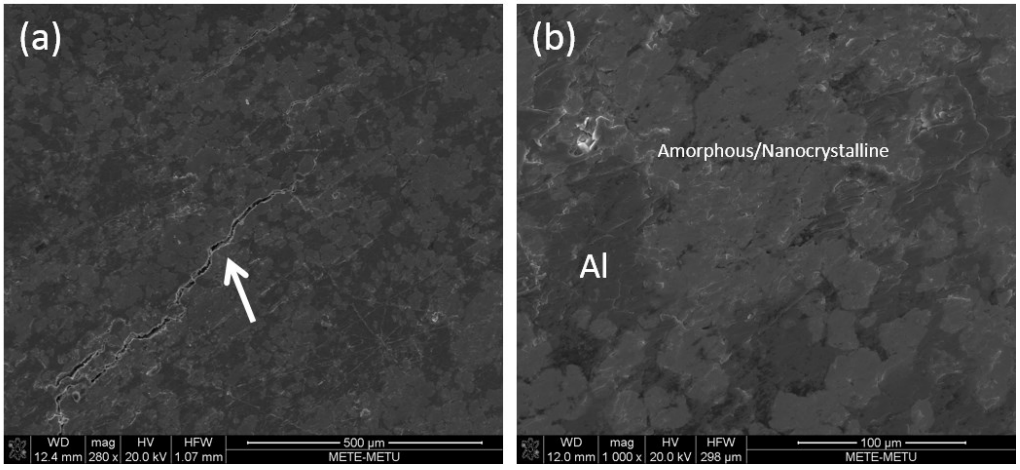

Figure 3.36: SEM images taken from the surface of the warm pressed $Al_{88}Sm_7Fe_5Ni_3$ amorphous/nanocrystalline with 30% pure Al added consolidate, after compression test.

Engineering-wise, an ideally designed structural material should require to have a hard surface and a softer inner core, to bear the load. To simulate this kind of structure, a layer ex-situ composite was designed with synthesized amorphous/nanocrystalline alloy layers on the top and bottom and pure Al layer sandwiched in between them. For this reason, 3 grams of pure Al powder was sandwiched between one gram of amorphous/nanocrystalline powder layer at the top and bottom of it, and consolidated with warm pressing (Figure 3.37.(a)). The produced layered ex-situ composite had a measured density of 2.9 g/cm^3. The surface investigation, together with elemental EDS

mapping of the layered ex-situ composite was done with SEM and given in Figure 3.37.(b). As it can be seen from the figure, the warm pressed layered ex-situ composite had shown very low number of porosities, and formation of good metallurgical bonds were observed, due aforementioned reasons.

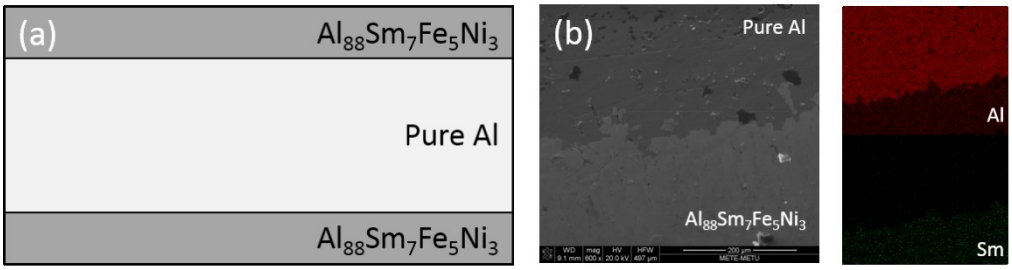

Figure 3.37: (a) Schematic representation of the layered ex-situ composite structure. **(b)** SEM image and elemental maps obtained from the interface region of the warm pressed $Al_{88}Sm_7Fe_5Ni_3$ amorphous/nanocrystalline and pure Al powders'.

As the layered ex-situ composite consisted of quite high amount of pure Al and had unique layered features, commenting on the mechanical behavior of the consolidate with compression test could be misleading. For that reason, to get an insight of the mechanical properties of the layered ex-situ composite structure, hardness tests were performed and given in Table 4.4, together with hardness' of the previously obtained consolidated with warm pressing.

When the measured hardness values of the warm pressed consolidates are evaluated, it can be seen that layered ex-situ composite structure had shown the highest hardness value, as compared to warm pressed amorphous/nanocrystalline and ex-situ composite consolidates. Regarding the facts that the layered ex-situ composite had quite well metallurgical bonding with low number of porosity and the surface of the structure consists of the hard amorphous/nanocrystalline phase, the measured values can be evaluated as plausible. In case of warm pressed amorphous/nanocrystalline consolidate, the obtained hardness values are comparable with the binary melt-spun Al-RE ribbons[82,166]. The lowest measured hardness belongs to ex-situ composite of $Al_{88}Sm_7Fe_5Ni_3$ amorphous/nanocrystalline and homogeneously dispersed pure Al. However, the low hardness value obtained from the ex-situ composite is not an

unexpected result, due to the size of the pure Al regions (Figure 3.36). As hardness measurements only reveals the local property of the investigated sample, there is a quite high chance that measurements could be taken from pure Al populous regions, which would give out lower hardness values.

Table 3.4: Measured hardness values of warm pressed consolidates.

	Warm Pressed $Al_{85}Sm_7Fe_5Ni_3$ Consolidate	**Warm Pressed $Al_{85}Sm_7Fe_5Ni_3$+%30Al Consolidate**	**Warm Pressed Layered Ex-situ Composite**
Hardness (H_V)	231	137	329
Standard Deviation	13	18	10

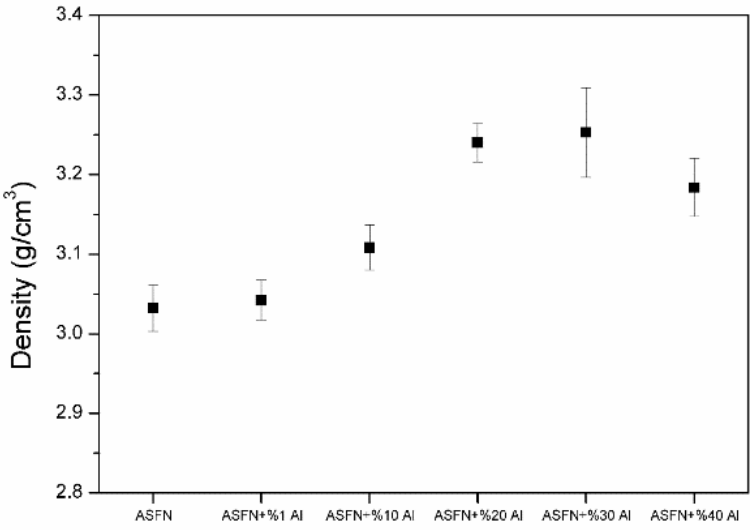

Figure 3.38: Density vs. added pure Al amount plot for warm pressed ex-situ composite consolidates.

The given hardness results had shown that ex-situ composite formation with addition of pure Al had decreased the hardness of the consolidates, however, this path also had shown significant enhancement on the densification and also mechanical behavior of the consolidates. When the results up to this point were considered, the optimum

results were obtained by ex-situ composite formed by $Al_{88}Sm_7Fe_5Ni_3$ amorphous/nanocrystalline and homogeneously dispersion of 30%w.t. pure Al. Thus, in the next step of the study, experiments were made to determine the optimal amount of homogeneously dispersed pure Al in the ex-situ composite consolidate.

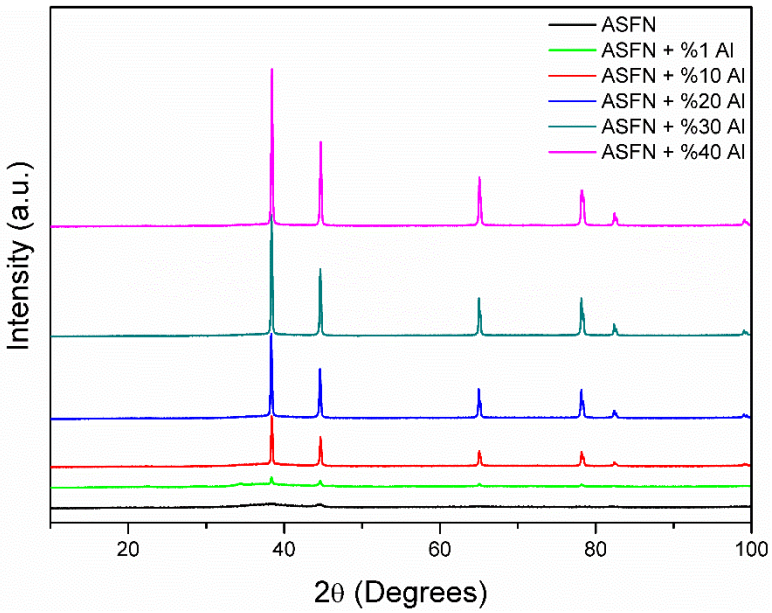

Figure 3.39: XRD patterns of warm pressed ex-situ composite consolidates with varying pure Al amounts.

Ex-situ composite consolidates of $Al_{88}Sm_7Fe_5Ni_3$ amorphous/nanocrystalline and homogeneously dispersed pure Al were produced via warm pressing with varying the amounts of pure Al by 1%, 10%, 20%, 30% and 40% by weight. Pure Al powders were homogeneously dispersed within $Al_{88}Sm_7Fe_5Ni_3$ amorphous/nanocrystalline alloy powders and warm pressed with the aforementioned setup. The measured density of the ex-situ consolidates were given in Figure 3.38, with respect to pure Al amount. It was observed that densification of the sole amorphous/nanocrystalline powders is enhanced with pure Al addition up to 20-30%, and a depression was observed at 40%w.t. pure Al addition. XRD patterns collected from the ex-situ composite consolidates with varying pure Al amounts were given in Figure 3.39. The diffraction patterns show the presence of pure Al reflections, together with pre-peak and amorphous hump of the amorphous phase. Similar to the results given in Figure 3.34,

reflections from the IM phase and side-peak cannot be clearly observed, due to the high scattering power of crystalline pure Al phase, with respect to amorphous phase and IM nanocrystals. Though one can say that with increasing pure Al content, intensities of crystalline pure Al reflections, as expected.

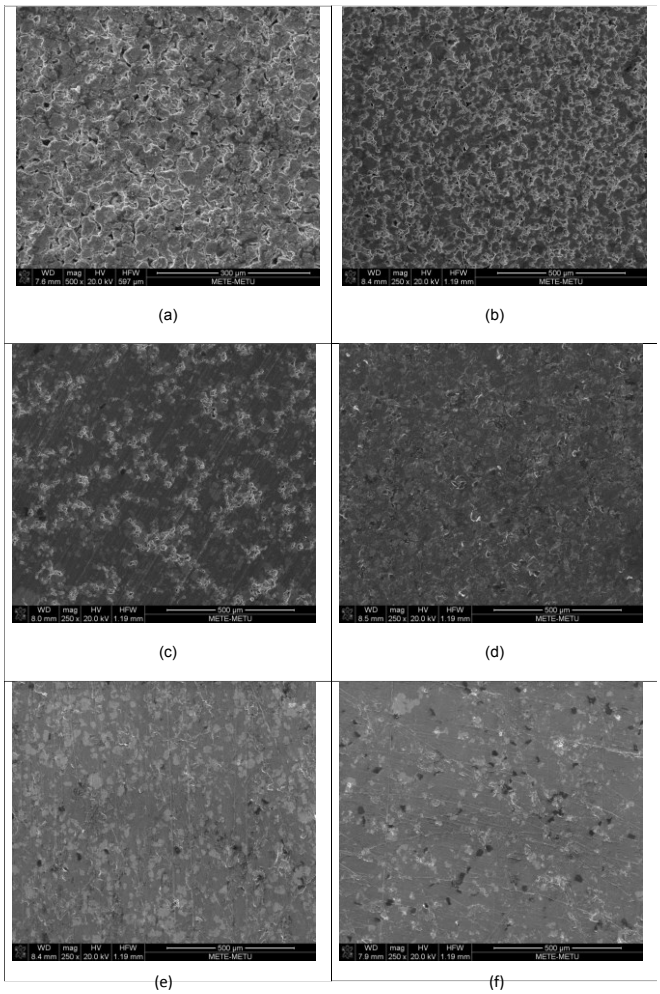

Figure 3.40: SEM images taken from the surface of warm pressed ex-situ composite consolidates with pure Al amounts of **(a)** 0, **(b)** 1%, **(c)** 10%, **(d)** 20%, **(e)** 30% and **(f)** 40%.

Surface of the warm pressed ex-situ composite consolidates with varying amount of pure Al were investigated with SEM and given in Figure 3.40. As the given SEM images clearly show, with increasing pure Al amount, the porosities in between the amorphous/nanocrystalline powders tend to decrease, which in turn increases the

densification of the consolidates. Given SEM images also explain the density depression at 40%w.t. pure Al addition. As it can be seen from Figure 3.40.(f), added pure Al powders reach a critical amount that rather than filling grain boundaries of amorphous/nanocrystalline powders, added pure Al powders had formed large regions of pure Al, thus overpass the densification enhancement and cause deterioration.

Hardness values of the ex-situ composite consolidates were given in Figure 3.41. As expected, with increasing amounts of pure Al dispersed into the amorphous/nanocomposite powders, the hardness of the consolidates decreases. The reason for the fulfillment of the stated expectation is that with increasing added pure Al amount, the chance that performing an indentation from a pure Al region increases; hence, causing collection of low hardness measurement values. Thus, it could be misleading to compare the mechanical behavior of the consolidates by only considering the output obtained from the hardness measurements.

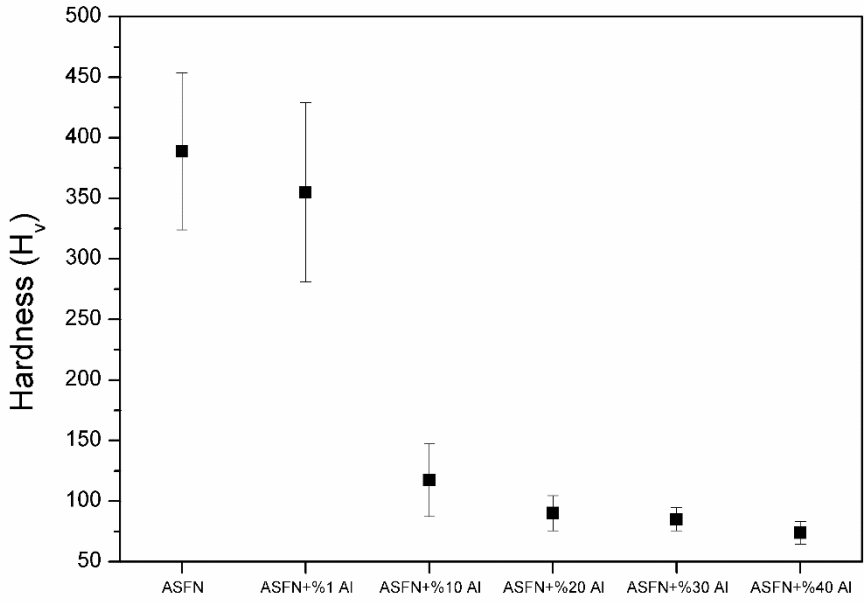

Figure 3.41: Hardness results measured from the surface of warm pressed ex-situ composite consolidates with varying pure Al amounts.

Compression test results of ex-situ composite consolidates of $Al_{88}Sm_7Fe_5Ni_3$ amorphous/nanocrystalline and homogeneously dispersed pure Al were given in Figure 3.42. As the stress-strain plot of the ex-situ composite consolidates reveal, the

mechanical properties of the structure does not vary much with the variation of added pure Al. This result was thought to be an implication of the attribution of amorphous/nanocrystalline regions to be the load carrying phase, in spite of pure Al phase. One thing that should be mentioned is that, as it can be seen from Figure 3.42, consolidates bearing 20% and 30%w.t. pure Al had shown limited plastic deformation, whereas the rest had failed in a brittle manner after passing the yield strength.

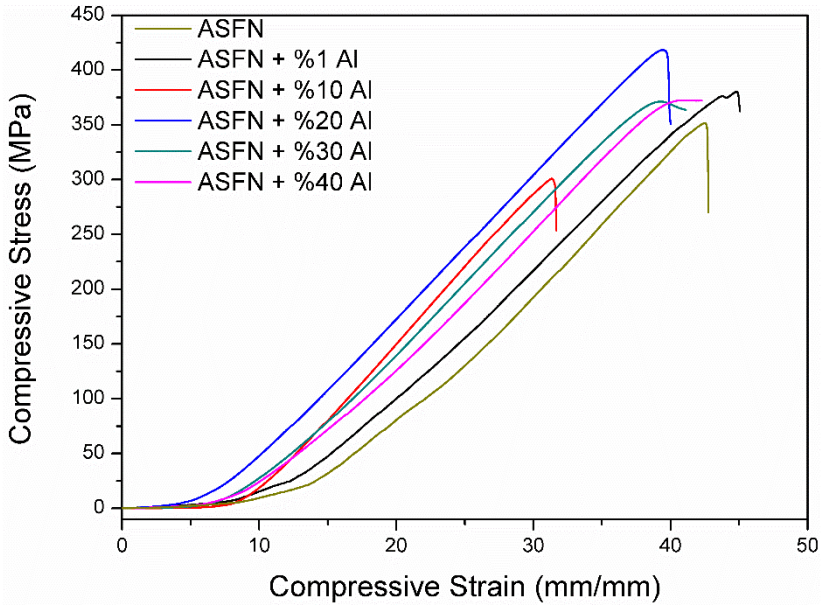

Figure 3.42: Compression test results of warm pressed ex-situ composite consolidates with varying pure Al amounts.

Thus, one can say that addition of a soft binder phase to a hard amorphous/nanocrystal phase to form an ex-situ composite does not alter the mechanical properties drastically. Further, it can be said that the homogeneous dispersion of micron sized pure Al into $Al_{88}Sm_7Fe_5Ni_3$ amorphous/nanocrystalline powders to form an ex-situ composite, only improves the sintering capability of the synthesized alloy, hence, increases the densification, via wetting the powder surfaces and easing the sintering.

3.5 Conclusion

Amorphization behaviors of several Al-based metallic glass forming alloys with mechanical milling or alloying were studied with high energy shaker milling. The

produced powders were either pressed and sintered or warm pressed in order to form bulk amorphous/nanocrystalline consolidates. In the initial trials, mechanical milling technique was used and failed to produce amorphous forms of gas-atomized $Al_{90}Sm_{10}$ and suction casted $Al_{85}Sm_7Fe_5Cu_3$ alloys with extensive milling for 140 and 150 hours, respectively. Secondly, mechanical alloying was adopted as a production route for powder production, and partially amorphous forms of $Al_{88}Sm_7Ni_5$ and $Al_{88}Sm_7Fe_5Ni_3$, with latter having the highest attained amorphous content in the study. Thus, mechanically alloyed $Al_{88}Sm_7Fe_5Ni_3$ powders were chosen as the input material for the consolidation experiments. As-milled state of mechanically alloyed $Al_{88}Sm_7Fe_5Ni_3$ amorphous/nanocrystalline composite powders were characterized using XRD, SEM, DSC, HEXRD and TEM. Overall characterization results had shown that the structure of the powders consists of amorphous phase, and spherical fcc-Al and unknown IM phase. Consolidation behavior of mechanically alloyed $Al_{88}Sm_7Fe_5Ni_3$ amorphous/nanocrystalline composite powders was studied and optimized with isothermal DSC experiments, and later adapted to sintering using a muffle furnace. Finally, consolidation of produced amorphous/nanocrystalline powders and its bulk ex-situ composites with mentioned powders and pure Al powder were produced by warm pressing. The mechanical behavior of these bulk composite structures were investigated with compression and hardness tests with post-mortem SEM studies.

3.6 Acknowledgments

This work partially supported by the Scientific and Technological Research Council of Turkey (TUBITAK) under Grant No. 113M346. The high-energy *in situ* X-ray experiments were performed at the BL04 - MSPD beamline of the ALBA Synchrotron Facility, and financially supported by CALIPSO program. Appreciation is expressed to Inmaculada Peral and Oriol Vallcorba for his valuable help in HEXRD experiments. The author acknowledges Fatih Sıkan for his efforts in density measurement and consolidation experiments, and Ayşe Merve Genç Ünalan and Serkan Yılmaz for their invaluable help in TEM analyses.

CHAPTER 4

CONCLUSION AND FUTURE RECOMMENDATIONS

4.1 Conclusion

In this study, the structure or marginal glass forming Al-RE alloys, and their amorphization through mechanical methods and consolidation into bulk form were studied. In the structural analysis part, building on the findings of previous M.S. student Can Yıldırım, as-produced structures of melt-spun ribbons and magnetron sputtered thin films of $Al_{90}Tb_{10}$ marginal metallic glass alloy was studied, by means of total scattering experiments combined with reverse Monte Carlo modelling. Total scattering experiments were performed in Alba Synchrotron Lightsource's BL-04 MSPD beamline with 30 keV in flat-plate transmission geometry. Experimental total X-ray structure factors and pair distribution functions for both alloys were calculated. In order to obtain the partial PDFs and to represent the atomic structures in 3D real space, RMC modelling of both alloys were made by constraining with obtained experimental total X-ray structure factors. The analyses done on 3D configurations of ribbons and thin films, it was found that structuring in the SRO in both alloys were topologically equivalent, albeit sputtered thin films are more disordered due its higher cooling rate and having vapor parent phase. Thus, it was discussed that topology selection of a certain amorphous alloy is a weak function of cooling rate and how ordered the parent phase is, yet it is rather dictated by the physio-chemical aspects of

bonding. Furthermore, previously reported FEM results by Yıldırım is also presented in the study, which reveals the fact that although both alloys show similar topological preference in the SRO, production route change have actually altered the ordering on the MRO scale, causing the change in the devitrification behavior.

In the second part of the study, production, optimization and characterization of bulk Al-based amorphous or amorphous/nanocrystalline structures were studied. For this reason, mechanical milling and alloying procedures were adopted. Firstly, mechanical milling of gas atomized $Al_{90}Sm_{10}$ and suction casted $Al_{85}Sm_7Fe_5Cu_3$ alloy were performed for extensive milling times over 140 hours, and no signs of amorphization were observed. Then, production route was changed to mechanical alloying and alloys $Al_{88}Sm_7Fe_5$ and $Al_{85}Sm_7Fe_5Ni_3$ were partially amorphized, with latter having the largest attained amorphous content in the study. Thus, mechanically alloyed $Al_{85}Sm_7Fe_5Ni_3$ amorphous/nanocrystalline alloy was chosen for consolidation studies. Consolidation of $Al_{85}Sm_7Fe_5Ni_3$ powders into bulk structures were done with two different methods: pressing and sintering, and warm pressing. It was found that higher applied pressures depressed the porosities and increased the obtained densities of the green compact and the consolidate. Variables such as applied pressure on pressing, sintering time and temperature were optimized for bulk Al-based amorphous/nanocrystalline composite production. Lastly, ex-situ composite formation with mechanically alloyed $Al_{85}Sm_7Fe_5Ni_3$ amorphous/nanocrystalline powders with pure Al powders with warm pressing was studied by means of mechanical properties. It was found that although introduction of pure Al powders had increased the densification, it had very minute or no effect on the mechanical properties of the bulk structure.

4.2 Future Recommendations

Considering the studies in our group and literature, although several studies that can be attributed as breakthroughs have been published in last several years, there is still an obscurity on the subject of amorphous structure in all of the metallic, ionic and covalent systems. Thus, the veil on the amorphous structure still affects the explanation

of arcane phenomena, such as unconventional nucleation kinetics and phase selection hierarchy in Al-RE metallic glasses. In this section, some of the initial results regarding structure of metallic glasses and few future perspectives on the subject will be stated.

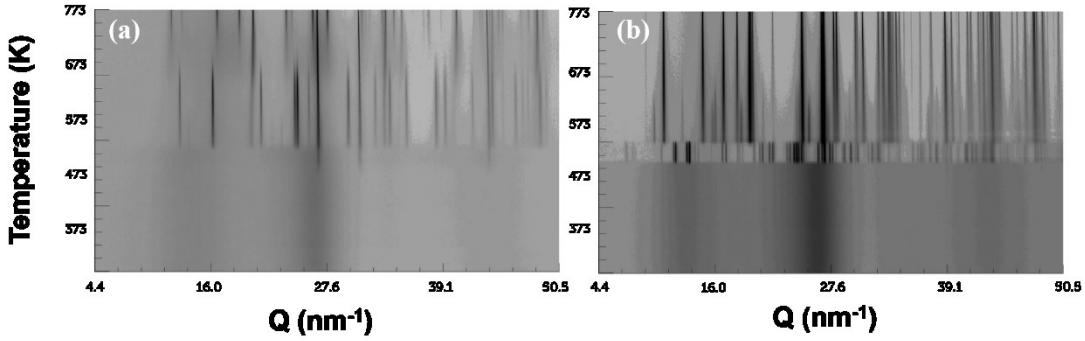

Figure 4.1: 2D surface plot of *in situ* heating HEXRD results of melt-spun **(a)** $Al_{90}Y_5Tb_5$ and **(b)** $Al_{90}Sm_5Tb_5$ metallic glasses.

The effect of rare earth chemistry and its impact on the amorphous structure is still under debate. Although current opinion on metallic amorphous structure, Miracle's ECP model[136,137], has its solid explanation through sole topological resolution, and also comprehensively explains important phenomena such as glass formation range, topology selection and their extensions on the medium-range order, it is still unable to explain various phenomena regarding the chemistry and bonding structure. These unexplained observations are directly attributed to "chemical effects" taking place on the electronic bonding in the structure. Thus, a general study of electronic structure of amorphous alloys with quantum mechanical molecular dynamics could be fruitful, as its results could explain the chemical and topological ordering on MRO scale.

In order to attack the same question experimentally, we are currently studying the effect of RE mixing on amorphous structures and devitrification with melt-spun ribbons $Al_{90}Y_5Tb_5$ and $Al_{90}Sm_5Tb_5$ metallic glass alloys. These glasses have been investigated with *in situ* HEXRD (Alba Synchrotron Lightsource BL-04 MSPD beamline, Spain) and 3D atom probe tomography (3DAP) (CAES, Idaho National Laboratory, USA) and it was observed that substitution of Tb with 5% of Y or Sm has changed the devitrification path. As it can be seen from Figure 4.1, the initial

devitrification product of $Al_{90}Y_5Tb_5$ glass is fcc-Al nanocrystals, which is the case for both $Al_{90}Y_{10}$ and $Al_{90}Tb_{10}$; however, $Al_{90}Sm_5Tb_5$ glass devitrified in a eutectic-like fashion with three or more unidentified intermetallic phases, which is not yet been reported in the literature. **Figure 4.2** shows the initial examination of the 3DAP results of the both alloys, heat treated to their respective initial crystallization temperature. This study can be extended as varying the RE element and constitution and certain chemical deductions could be made, via electronegativities and chemistry and crystal structures of devitrification species.

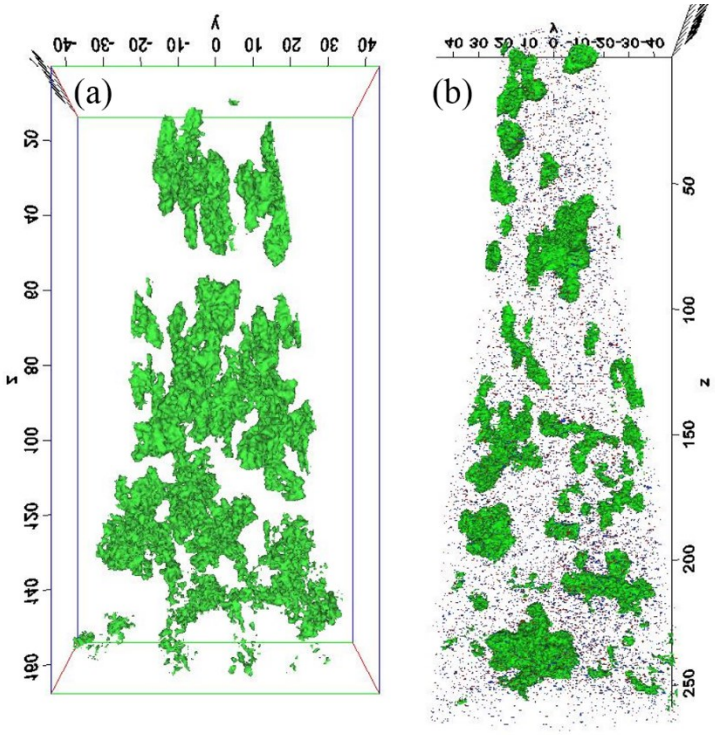

Figure 4.2: 3DAP reconstructions of **(a)** $Al_{90}Y_5Tb_5$ and **(b)** $Al_{90}Sm_5Tb_5$. Green isosurface corresponds to 95% Al concentration. 20% Tb (red) and Sm (green) isosurfaces are also rendered in **(b)**.

In the rapid solidification reports on the literature, discrepancies could be observed on the studies regarding the same metallic glass. The writer attributes these discrepancies to the fact that these is no study on the pure physical metallurgical treatment on the glass formation with respect to processing parameters; i.e. there is no study in the

literature that investigates the amorphous structure with respect to the casting temperature, time that elapses on the molten state (or chemical and structural homogeneity of the melt), quenching rate, etc. Findings of Yıldırım[103] and the calculations made in this study reveals that ordering in short-range is rather defined for alloys of high chemical preference (with negative heat of mixing), yet ordering of the medium-range is clearly processing parameter dependent. The proposed treatment is quite analogous to the effect of temperature and time spent in austenitization on the structure selection in plain steels[201]. Having such an information about the structure selection (mainly on the size and distribution of MRO structures) of amorphous alloys could enable tailoring of their properties with appropriate processing selection.

As stated in the text, and also in the recent publications, the structure development in the medium-range starts in the molten state and continues whilst the material cools down to supercooled liquid state to glass transition. Such observations were made previously for the bulk metallic glass forming alloys but not reported for the marginal glass forming alloys. For that reason, we had proposed and granted with beamtime in Soleil Synchrotron Lightsource, France to perform *in situ* total scattering experiments with levitation melting. In the mentioned study, we would like to collect HEXRD patterns of Al-RE alloys in molten and supercooled liquid state, and PDF analysis will be done with respect to temperature, from molten to supercooled liquid state. Furthermore, sole total scattering experiments will not be sufficient for dynamical analysis of the atomic processes. Thus, collection of dynamical thermodynamical properties such as viscosity could be effective for commenting on the dynamical structure evolution in both SRO and MRO scale for Al-RE glasses.

Similarly, rather than deriving the partial PDFs with an indirect method (i.e. RMC), to acquire information about the local environment of RE atoms, we had proposed and granted with beamtime Alba Synchrotron Lightsource to perform *in situ* X-ray absorption fine structure experiments (XAFS) on Al-RE metallic glasses. In this study, we will perform X-ray absorption experiments on RE LIII absorption edges, both in X-ray absorption near edge structure (XANES) regime to resolve the bonding structure, and also in the extended X-ray absorption fine structure (EXAFS)

experiments to collect data for partial PDF derivation. However, XAFS beamline in Alba is not suitable for *in situ* characterization of metallic glasses, as the dynamic phenomena occurring in these systems have shorter timescales than the temporal accuracy of the acquisition method. For that reason, to perform XANES and EXAFS experiments with optimal temporal resolution, repetition of explained experiments in an energy dispersive XAFS beamline (ID24 of ESRF, I20 of Diamond, DAXS of LNLS, etc.) could be more appropriate.

In a completely different perspective, the concepts of liquid and amorphous structure, amorphization and glass transition should also be treated from philosophical standpoint. The concepts of disorder, medium-range order, topological arrangements are long living questions of philosophers, which made them observe the nature, leading them to a scientific path. However, the philosophical deductions on the nature that are made on the base of logic is still applicable to deduce insights for the natural phenomena, as these ideas are actually generated to explain the processing taking place in the material world. Such an example can be given as Gilles Deleuze's ideas on populational and differential thought[212], which can be used in the interpretation of the amorphous structure. Deleuze states that the individuals and the population formed by each individual are differentiated and become distinct entities; meaning that each individual in a population is a unique entity by means of its properties and qualities, however, the population that is formed by the unique individuals has its own ontological existence as an entity. This is explained as in a population of individuals, certain properties and qualities could show some kind of distribution and the average value of these define ontologically new entity, representing the population. When the structure of metallic glasses is being discussed, the structure of an alloy is represented with the most abundant Voronoi polyhedron that the structure shows. An example can be given through Cu-Zr metallic glass system. The structure of Cu-Zr metallic glasses are generally represented with solute-centered icosahedra, in both Cu-rich and Zr-rich constitutions[67,190]. Further, their solidification, phase selection and mechanical properties are generally discussed and explained with either the solute-centered icosahedra or its respective networks' from the point of view. However, theoretically, it is known that structure of Cu-Zr glasses are not composed only with icosahedra,

several topologically distorted forms of icosahedra and clusters with lower and higher coordination are also present. Nevertheless, structure-property relationship-wise, it is logical to discuss the phenomena through icosahedral topology, as it and its derivatives are the most abundant topology in the clusteral population. A Deleusian explanation of this enigma can be done by attributing different ontological status of each cluster arrangement and the most abundant cluster arrangement with the stated ideas above. Hence, modern philosophy can enable scientist to understand and interpret the observations made with a different perspective. Also, having a philosophical approach towards the liquid and amorphous structure might enlighten different thought ways to the researchers and to the human-kind, as well.

REFERENCES

(1) Klement, W.; Willens, R. H.; Duwez, P. Non-crystalline Structure in Solidified Gold–Silicon Alloys. *Nature* **1960**, *187* (4740), 869–870 DOI: 10.1038/187869b0.

(2) Chen, H. .; Turnbull, D. Formation, stability and structure of palladium-silicon based alloy glasses. *Acta Metall.* **1969**, *17* (8), 1021–1031 DOI: 10.1016/0001-6160(69)90048-0.

(3) Chen, H. . Thermodynamic considerations on the formation and stability of metallic glasses. *Scr. Metall.* **1974**, *22* (12), 1505–1511 DOI: 10.1016/0001-6160(74)90112-6.

(4) Kui, H. W.; Greer, A. L.; Turnbull, D. Formation of bulk metallic glass by fluxing. *Appl. Phys. Lett.* **1984**, *45* (6), 615 DOI: 10.1063/1.95330.

(5) Duwez, P. Amorphous Ferromagnetic Phase in Iron-Carbon-Phosphorus Alloys. *J. Appl. Phys.* **1967**, *38* (10), 4096 DOI: 10.1063/1.1709084.

(6) Hasegawa, R.; Ray, R. Iron-boron metallic glasses. *J. Appl. Phys.* **1978**, *49* (7), 4174 DOI: 10.1063/1.325328.

(7) Ray, R.; Giessen, B. C.; Grant, N. J. New non-crystalline phases in splat cooled transition metal alloys. *Scr. Metall.* **1968**, *2* (6), 357–359 DOI: 10.1016/0036-9748(68)90138-5.

(8) Kwon, O. J.; Kim, Y. C.; Kim, K. B.; Lee, Y. K.; Fleury, E. Formation of amorphous phase in the binary Cu−Zr alloy system. *Met. Mater. Int.* **2006**, *12* (3), 207–212 DOI: 10.1007/BF03027532.

(9) Mei-Bo, T.; De-Qian, Z.; Ming-Xiang, P.; Wei-Hua, W. Binary Cu–Zr Bulk Metallic Glasses. *Chinese Phys. Lett.* **2004**, *21* (5), 901–903 DOI: 10.1088/0256-307X/21/5/039.

(10) Shang, B. S.; Li, M. Z.; Yao, Y. G.; Lu, Y. J.; Wang, W. H. Evolution of atomic rearrangements in deformation in metallic glasses. *Phys. Rev. E* **2014**, *90* (4), 042303 DOI: 10.1103/PhysRevE.90.042303.

(11) Fang, X. W.; Wang, C. Z.; Hao, S. G.; Kramer, M. J.; Yao, Y. X.; Mendelev, M. I.; Ding, Z. J.; Napolitano, R. E.; Ho, K. M. Spatially resolved distribution function and the medium-range order in metallic liquid and glass. *Sci. Rep.* **2011**, *1*, 194 DOI: 10.1038/srep00194.

(12) Li, M.; Wang, C. Z.; Hao, S. G.; Kramer, M. J.; Ho, K. M. Structural heterogeneity and medium-range order in Zr_xCu_{100-x} metallic glasses. *Phys. Rev. B* **2009**, *80* (18), 184201 DOI: 10.1103/PhysRevB.80.184201.

(13) Park, K.-W.; Jang, J.; Wakeda, M.; Shibutani, Y.; Lee, J.-C. Atomic packing density and its influence on the properties of Cu–Zr amorphous alloys. *Scr. Mater.* **2007**, *57* (9), 805–808 DOI: 10.1016/j.scriptamat.2007.07.019.

(14) Xu, D.; Lohwongwatana, B.; Duan, G.; Johnson, W. L.; Garland, C. Bulk metallic glass formation in binary Cu-rich alloy series – $Cu_{100-x}Zr_x$ (x=34, 36, 38.2, 40 at.%) and mechanical properties of bulk Cu64Zr36 glass. *Acta Mater.* **2004**, *52* (9), 2621–2624 DOI: 10.1016/j.actamat.2004.02.009.

(15) Wang, W. H.; Lewandowski, J. J.; Greer, A. L. Understanding the Glass-forming Ability of $Cu_{50}Zr_{50}$ Alloys in Terms of a Metastable Eutectic. *J. Mater. Res.* **2011**, *20* (09), 2307–2313 DOI: 10.1557/jmr.2005.0302.

(16) Georgarakis, K.; Yavari, A. R.; Louzguine-Luzgin, D. V.; Antonowicz, J.; Stoica, M.; Li, Y.; Satta, M.; LeMoulec, A.; Vaughan, G.; Inoue, A. Atomic structure of Zr–Cu glassy alloys and detection of deviations from ideal solution behavior with Al addition by x-ray diffraction using synchrotron light in transmission. *Appl. Phys. Lett.* **2009**, *94* (19), 191912 DOI: 10.1063/1.3136428.

(17) Lekka, C. E.; Evangelakis, G. A. Bonding characteristics and strengthening of CuZr fundamental clusters upon small Al additions from density functional theory calculations. *Scr. Mater.* **2009**, *61* (10), 974–977 DOI:

10.1016/j.scriptamat.2009.08.008.

(18) Révész, Á.; Concustell, A.; Varga, L. K.; Suriñach, S.; Baró, M. D. Influence of the wheel speed on the thermal behaviour of $Cu_{60}Zr_{20}Ti_{20}$ alloys. *Mater. Sci. Eng. A* **2004**, *375-377*, 776–780 DOI: 10.1016/j.msea.2003.10.151.

(19) Peker, a; Johnson, W. L. A highly processable metallic glass: $Zr_{41.2}Ti_{13.8}Cu_{12.5}Ni_{10.0}Be_{22.5}$. *Appl. Phys. Lett.* **1993**, *63* (October), 2342–2344 DOI: 10.1063/1.110520.

(20) Liquidmetal Technologies http://liquidmetal.com/.

(21) Inoue, A. Amorphous, nanoquasicrystalline and nanocrystalline alloys in Al-based systems. *Prog. Mater. Sci.* **1998**, *43* (5), 365–520 DOI: 10.1016/S0079-6425(98)00005-X.

(22) Inoue, A.; Kitamura, A.; Masumoto, T. The effect of aluminium on mechanical properties and thermal stability of (Fe, Co, Ni)-Al-B ternary amorphous alloys. *J. Mater. Sci.* **1981**, *16* (7), 1895–1908 DOI: 10.1007/BF00540638.

(23) Inoue, A.; Yamamoto, M.; Kimura, H. M.; Masumoto, T. Ductile aluminium-base amorphous alloys with two separate phases. *J. Mater. Sci. Lett.* **1987**, *6* (2), 194–196 DOI: 10.1007/BF01728983.

(24) Inoue, A.; Ohtera, K.; Masumoto, T. New Amorphous Al-Y, Al-La and Al-Ce Alloys Prepared by Melt Spinning. *Japanese Journal of Applied Physics*. 1988, pp L736–L739.

(25) Inoue, A.; Ohtera, K.; Tao, Z.; Masumoto, T. New Amorphous Al-Ln (Ln=Pr, Nd, Sm or Gd) Alloys Prepared by Melt Spinning. *Japanese Journal of Applied Physics*. 1988, pp L1583–L1586.

(26) Inoue, A.; Zhang, T.; Kita, K.; Masumoto, T. Mechanical Strengths, Thermal Stability and Electrical Resistivity of Aluminum-Rare Earth Metal Binary Amorphous Alloys. *Mater. Trans. JIM* **1989**, *30* (11), 870–877 DOI: 10.2320/matertrans1989.30.870.

(27) Inoue, A.; Ohtera, K.; Tsai, A.-P.; Masumoto, T. Aluminum-Based Amorphous Alloys with Tensile Strength above 980 MPa (100 kg/mm^2). *Jpn. J. Appl. Phys.* **1988**, *27* (Part 2, No. 4), L479–L482.

(28) Inoue, A.; Ohtera, K.; Tsai, A.-P.; Masumoto, T. New Amorphous Alloys with Good Ductility in Al-Y-M and Al-La-M (M=Fe, Co, Ni or Cu) Systems. *Japanese Journal of Applied Physics*. 1988, pp L280–L282.

(29) Inoue, A.; Ohtera, K.; Kita, K.; Masumoto, T. New Amorphous Alloys with Good Ductility in Al-Ce-M (M=Nb, Fe, Co, Ni or Cu) Systems. *Jpn. J. Appl. Phys.* **1988**, *27* (Part 2, No. 10), L1796–L1799 DOI: 10.1143/JJAP.27.L1796.

(30) He, Y.; Poon, S. J.; Shiflet, G. J. Synthesis and Properties of Metallic Glasses That Contain Aluminum. *Sci.* **1988**, *241* (4873), 1640–1642 DOI: 10.1126/science.241.4873.1640.

(31) Shiflet, G. J.; He, Y.; Poon, S. J. Mechanical properties of a new class of metallic glasses based on aluminum. *J. Appl. Phys.* **1988**, *64* (12), 6863 DOI: 10.1063/1.341978.

(32) Shiflet, G. J.; He, Y.; Poon, S. J. Mechanical properties of aluminum-rich AlFeGd metallic glass. *Scr. Metall.* **1988**, *22* (10), 1661–1664 DOI: 10.1016/S0036-9748(88)80261-8.

(33) Li, X. P.; Yan, M.; Imai, H.; Kondoh, K.; Wang, J. Q.; Schaffer, G. B.; Qian, M. Fabrication of 10 mm diameter fully dense $Al_{86}Ni_6Y_{4.5}Co_2La_{1.5}$ bulk metallic glass with high fracture strength. *Mater. Sci. Eng. A* **2013**, *568*, 155–159 DOI: 10.1016/j.msea.2013.01.041.

(34) Kotan, G.; Tan, E.; Kalay, Y. E.; Gür, C. H. Homogenization of ECAPed Al 2024 alloy through age-hardening. *Mater. Sci. Eng. A* **2013**, *559* (0921), 601–606 DOI: 10.1016/j.msea.2012.08.148.

(35) Busch, R.; Schroers, J.; Wang, W. H. Thermodynamics and Kinetics of Bulk Metallic Glass. *MRS Bull.* **2011**, *32* (08), 620–623 DOI: 10.1557/mrs2007.122.

(36) Suryanarayana, C.; Inoue, A. *Bulk Metallic Glasses*; CRC Press: Boca Raton, FL, 2011.

(37) Cahn, R. W.; Hono, K.; Haasen, P. *Physical Metallurgy, Vol. 2*, 4th Editio.; Cahn, R. W., Haasen, P., Eds.; North Holland, 1996.

(38) Kauzmann, W. The Nature of the Glassy State and the Behavior of Liquids at Low Temperatures. *Chem. Rev.* **1948**, *43* (2), 219–256 DOI: 10.1021/cr60135a002.

(39) Perepezko, J. H. Nucleation-controlled reactions and metastable structures. *Prog. Mater. Sci.* **2004**, *49* (3-4), 263–284 DOI: 10.1016/S0079-6425(03)00028-8.

(40) Saunders, N.; Miodownik, A. P. Thermodynamic aspects of amorphous phase formation. *Journal of Materials Research*. 1986, pp 38–46.

(41) Inoue, A. Stabilization of metallic supercooled liquid and bulk amorphous alloys. *Acta Mater.* **2000**, *48* (1), 279–306 DOI: 10.1016/S1359-6454(99)00300-6.

(42) Greer, A. L. Confusion by design. *Nature* **1993**, *366* (6453), 303–304 DOI: 10.1038/366303a0.

(43) Busch, R. The thermophysical properties of bulk metallic glass-forming liquids. *JOM*. 2000, pp 39–42.

(44) Verhoeven, J. D. *Fundamentals of Physical Metallurgy*, 1st Editio.; John Wiley & Sons, Inc.: Canada, 1975.

(45) Zhong, L.; Wang, J.; Sheng, H.; Zhang, Z.; Mao, S. X. Formation of monatomic metallic glasses through ultrafast liquid quenching. *Nature* **2014**, *512* (7513), 177–180 DOI: 10.1038/nature13617.

(46) Materials Preparation Center, A.L., US DOE Basic Energy Sciences, Ames, IA, USA http://www.ameslab.gov/mpc (accessed Feb 17, 2013).

(47) Altieri, A. L.; Steen, P. H. Substrate Heating in the Planar-Flow Melt Spinning of Metals. *J. Therm. Sci. Eng. Appl.* **2014**, *6* (4), 041011 DOI: 10.1115/1.4027809.

(48) Pond, R. B. Metallic filaments and method of making same. Google Patents March 4, 1958.

(49) DirectVacuum, Micro Magnetics, Inc.

http://www.directvacuum.com/sputter.asp (accessed Jun 2, 2015).

(50) Windows and Daylighting Division, Lawerence Berkeley National Laboratory https://windows.lbl.gov/materials/chromogenics/hydrides.htm (accessed Jun 2, 2015).

(51) Boettinger, W. J.; Perepezko, J. H. Fundamentals of Solidification at High Rates. In *Rapidly Solidified Alloys: Processes-Structures-Properties-Applications*; Liebermann, H. H., Ed.; CRC Press, 1993; p 21.

(52) *Bulk Metallic Glasses: An Overview*; Miller, M., Liaw, P., Eds.; Springer Science+Business Media, 2008.

(53) *Non-equilibrium Processing of Materials*; Suryanarayana, C., Ed.; Pergamon, 1999.

(54) Suryanarayana, C. Mechanical alloying and milling. *Progress in Materials Science*. 2001, pp 1–184.

(55) Yermakov, A. Y.; Yurchikov, Y. Y.; Barinov, V. A. MAGNETIC PROPERTIES OF AMORPHOUS POWDERS OF Y-Co ALLOYS PRODUCED BY GRINDING. *Physics of Metals and Metallography*. 1981, pp 50–58.

(56) Koch, C. C. Preparation of "'amorphous'" $Ni_{60}Nb_{40}$ by mechanical alloying. *Appl. Phys. Lett.* **1983**, *43* (11), 1017 DOI: 10.1063/1.94213.

(57) Suryanarayana, C.; Ivanov, E.; Boldyrev, V. V. The science and technology of

mechanical alloying. *Mater. Sci. Eng. A* **2001**, *304-306* (1-2), 151–158 DOI: 10.1016/S0921-5093(00)01465-9.

(58) AYDINBEYLI, N.; NURICELIK, O.; GASAN, H.; AYBAR, K. Effect of the heating rate on crystallization behavior of mechanically alloyed $Mg_{50}Ni_{50}$ amorphous alloy. *International Journal of Hydrogen Energy*. 2006, pp 2266–2273.

(59) Tan, Z.; Xue, Y. F.; Wang, L.; Cheng, X. W.; Zhang, L.; Zhang, H. F.; Wang, a M. Alloying evolution and stability of $Al_{65}Cu_{20}Ti_{15}$ during process of amorphisation by high energy ball milling. *Powder Metall.* **2012**, *55* (5), 361–367 DOI: 10.1179/1743290112Y.0000000005.

(60) Alleg, S.; Souilah, S.; Suñol, J. J. Thermal Stability of the Nanostructured Powder Mixtures Prepared by Mechanical Alloying. In *Transformation*; Elkordy, A. A., Ed.; InTech, 2013.

(61) Turnbull, D.; Cohen, M. H. Free-Volume Model of the Amorphous Phase: Glass Transition. *J. Chem. Phys.* **1961**, *34* (1), 120 DOI: 10.1063/1.1731549.

(62) Gibbs, J. H.; DiMarzio, E. A. Nature of the Glass Transition and the Glassy State. *J. Chem. Phys.* **1958**, *28* (3), 373 DOI: 10.1063/1.1744141.

(63) Jiang, W. H.; Atzmon, M. The effect of compression and tension on shear-band structure and nanocrystallization in amorphous $Al_{90}Fe_5Gd_5$: A high-resolution transmission electron microscopy study. *Acta Mater.* **2003**, *51* (14), 4095–4105 DOI: 10.1016/S1359-6454(03)00229-5.

(64) Jiang, W.; Atzmon, M. Mechanically-assisted nanocrystallization and defects in amorphous alloys: A high-resolution transmission electron microscopy study. *Scr. Mater.* **2006**, *54* (3), 333–336 DOI: 10.1016/j.scriptamat.2005.09.052.

(65) Hirotsu, Y.; Nieh, T. G.; Hirata, a; Ohkubo, T.; Tanaka, N. Local atomic ordering and nanoscale phase separation in a Pd-Ni-P bulk metallic glass. *Phys. Rev. B* **2006**, *73* (1), 012205 DOI: 10.1103/PhysRevB.73.012205.

(66) Williams, D. B.; Carter, C. B. *Transmission Electron Microscopy: A Textbook for Materials Science*, Second Edi.; Springer Science+Business Media, 2009; Vol. V1-V4.

(67) Cheng, Y. Q.; Ma, E. Atomic-level structure and structure–property relationship in metallic glasses. *Prog. Mater. Sci.* **2011**, *56* (4), 379–473 DOI: 10.1016/j.pmatsci.2010.12.002.

(68) Voyles, P. Fluctuation Microscopy https://tem.msae.wisc.edu/fluctuation-microscopy/ (accessed Jun 16, 2015).

(69) Egami, T.; Billinge, S. J. . *Underneath the Bragg Peaks - Structural Analysis of Complex Materials*; Pergamon, 2012.

(70) Treacy, M. M. J. When structural noise is the signal: Speckle statistics in fluctuation electron microscopy. *Ultramicroscopy* **2007**, *107* (2-3), 166–171 DOI: 10.1016/j.ultramic.2006.07.001.

(71) Gibson, J.; Treacy, M. Diminished Medium-Range Order Observed in Annealed Amorphous Germanium. *Physical Review Letters*. 1997, pp 1074–1077.

(72) Li, J.; Gu, X.; Hufnagel, T. C. Using Fluctuation Microscopy to Characterize Structural Order in Metallic Glasses. *Microsc. Microanal.* **2003**, *9* (06), 509–515 DOI: 10.1017/S1431927603030459.

(73) Stratton, W. G.; Hamann, J.; Perepezko, J. H.; Voyles, P. M.; Mao, X.; Khare, S. V. Aluminum nanoscale order in amorphous $Al_{92}Sm_8$ measured by fluctuation electron microscopy. *Appl. Phys. Lett.* **2005**, *86* (14), 1–3 DOI: 10.1063/1.1897830.

(74) ESRF Website http://www.esrf.eu/about/synchrotron-science/synchrotron (accessed May 20, 2016).

(75) Willmott, P. *An Introduction to Synchrotron Radiation*; John Wiley & Sons, Ltd: Chichester, UK, 2011.

(76) *Synchrotron Radiation*; Mobilio, S., Boscherini, F., Meneghini, C., Eds.; Springer Berlin Heidelberg: Berlin, Heidelberg, 2015.

(77) *Neutrons and Synchrotron Radiation in Engineering Materials Science*; Reimers, W., Pyzalla, A. R., Schreyer, A. K., Clemens, H., Eds.; Wiley-VCH Verlag GmbH & Co. KGaA: Weinheim, Germany, 2008.

(78) Wikipedia - Insertion Device http://en.wikipedia.org/wiki/Insertion_device (accessed May 20, 2016).

(79) Reimers, W.; Pyzalla, A. R.; Schreyer, A. K.; Clemens, H. *Neutrons and Synchrotron Radiation in Engineering Materials Science: From Fundamentals to Material and Component Characterization*; Wiley-VCH Verlag GmbH & Co. KGaA, 2008.

(80) Antonowicz, J. Phase separation and nanocrystal formation in Al-based metallic glasses. *J. Alloys Compd.* **2007**, *434-435* (SPEC. ISS.), 126–130 DOI: 10.1016/j.jallcom.2006.08.152.

(81) Rontó, V.; Battezzati, L.; Yavari, A. R.; Tonegaru, M.; Lupu, N.; Heunen, G. Crystallization behaviour of $Al_{87}Ni_7La_6$ and $Al_{87}Ni_7Sm_6$ amorphous alloys. *Scr. Mater.* **2004**, *50* (6), 839–843 DOI: 10.1016/j.scriptamat.2003.12.012.

(82) Kalay, Y. E.; Chumbley, L. S.; Anderson, I. E. Crystallization behavior in a highly driven marginal glass forming alloy. *J. Non. Cryst. Solids* **2008**, *354* (26), 3040–3048 DOI: 10.1016/j.jnoncrysol.2007.12.006.

(83) Sheng, H. W.; Liu, H. Z.; Cheng, Y. Q.; Wen, J.; Lee, P. L.; Luo, W. K.; Shastri, S. D.; Ma, E. Polyamorphism in a metallic glass. *Nat. Mater.* **2007**, *6* (3), 192–197 DOI: 10.1038/nmat1839.

(84) Stoica, M.; Das, J.; Bednarčik, J.; Wang, G.; Vaughan, G.; Wang, W. H.; Eckert, J. Mechanical response of metallic glasses: Insights from in-situ high energy X-ray diffraction. *JOM* **2010**, *62* (2), 76–82 DOI: 10.1007/s11837-010-0037-3.

(85) Mattern, N.; Bednarčik, J.; Pauly, S.; Wang, G.; Das, J.; Eckert, J. Structural

evolution of Cu–Zr metallic glasses under tension. *Acta Mater.* **2009**, *57* (14), 4133–4139 DOI: 10.1016/j.actamat.2009.05.011.

(86) Stoica, M.; Das, J.; Bednarcik, J.; Franz, H.; Mattern, N.; Wang, W. H.; Eckert, J. Strain distribution in $Zr_{64.13}Cu_{15.75}Ni_{10.12}Al_{10}$ bulk metallic glass investigated by in situ tensile tests under synchrotron radiation. *J. Appl. Phys.* **2008**, *104* (1), 013522 DOI: 10.1063/1.2952034.

(87) Herklotz, M.; Scheiba, F.; Hinterstein, M.; Nikolowski, K.; Knapp, M.; Dippel, A.-C.; Giebeler, L.; Eckert, J.; Ehrenberg, H. Advances in in situ powder diffraction of battery materials: a case study of the new beamline P02.1 at DESY, Hamburg. *J. Appl. Crystallogr.* **2013**, *46* (4), 1117–1127 DOI: 10.1107/S0021889813013551.

(88) Juhás, P.; Davis, T.; Farrow, C. L.; Billinge, S. J. L. PDFgetX3: A rapid and highly automatable program for processing powder diffraction data into total scattering pair distribution functions. *J. Appl. Crystallogr.* **2013**, *46* (2), 560–566 DOI: 10.1107/S0021889813005190.

(89) Farrow, C. L.; Billinge, S. J. L. Towards a robust ad-hoc data correction approach that yields reliable atomic pair distribution functions from powder diffraction data. **2012**.

(90) Warren, B. E. *X-ray Diffraction*, Reprint Ed.; Dover Publications, 1990; Vol. 1.

(91) Guinier, A. *X-ray Diffraction in Crystals, Imperfect Crystals, and Amorphous Bodies*; Dover Publications, 1994.

(92) Benmore, C. J. A Review of High-Energy X-Ray Diffraction from Glasses and Liquids. *ISRN Mater. Sci.* **2012**, *2012*, 1–19 DOI: 10.5402/2012/852905.

(93) Elliott, S. R. Medium-range structural order in covalent amorphous solids. *Nature* **1991**, *354* (6353), 445–452 DOI: 10.1038/354445a0.

(94) Jiang, Z.-H.; Zhang, Q.-Y. The structure of glass: A phase equilibrium diagram approach. *Prog. Mater. Sci.* **2014**, *61*, 144–215 DOI:

10.1016/j.pmatsci.2013.12.001.

(95) Kalay, Y. E.; Kalay, I.; Hwang, J.; Voyles, P. M.; Kramer, M. J. Local chemical and topological order in Al-Tb and its role in controlling nanocrystal formation. *Acta Mater.* **2012**, *60* (3), 994–1003 DOI: 10.1016/j.actamat.2011.11.008.

(96) Zhang, F.; Sun, Y.; Ye, Z.; Zhang, Y.; Wang, C.-Z.; Mendelev, M. I.; Ott, R. T.; Kramer, M. J.; Ding, Z.-J.; Ho, K. M. Solute–solute correlations responsible for the prepeak in structure factors of undercooled Al-rich liquids: a molecular dynamics study. *J. Phys. Condens. Matter* **2015**, *27* (20), 205701 DOI: 10.1088/0953-8984/27/20/205701.

(97) Han, J. J.; Wang, W. Y.; Liu, X. J.; Wang, C. P.; Hui, X. D.; Liu, Z. K. Effect of solute atoms on glass-forming ability for Fe–Y–B alloy: An ab initio molecular dynamics study. *Acta Mater.* **2014**, *77*, 96–110 DOI: 10.1016/j.actamat.2014.04.070.

(98) Luo, W. K.; Sheng, H. W.; Ma, E. Pair correlation functions and structural building schemes in amorphous alloys. *Appl. Phys. Lett.* **2006**, *89* (13), 8–10 DOI: 10.1063/1.2356473.

(99) McGreevy, R. L. Reverse Monte Carlo modelling. *J.Phys.:Condens. Matter* **2001**, *13* (46), R877–R913 DOI: 10.1088/0953-8984/13/46/201.

(100) Keen, D. A.; McGreevy, R. L. Structural modelling of glasses using reverse Monte Carlo simulation. *Nature*. 1990, pp 423–425.

(101) Wikipedia - Radial Distribution Function

https://en.wikipedia.org/wiki/Radial_distribution_function (accessed May 25, 2016).

(102) Ashby, M.; Greer, A. L. Metallic glasses as structural materials. *Scr. Mater.* **2006**, *54* (3), 321–326 DOI: 10.1016/j.scriptamat.2005.09.051.

(103) Yıldırım, C. Structural and Dynamical Evolution of Nanocrystals, MS Thesis,

Middle East Technical University, 2013.

(104) Sheng, H. W.; Luo, W. K.; Alamgir, F. M.; Bai, J. M.; Ma, E. Atomic packing and short-to-medium-range order in metallic glasses. *Nature* **2006**, *439* (7075), 419–425 DOI: 10.1038/nature04421.

(105) Zeng, Q.; Sheng, H.; Ding, Y.; Wang, L.; Yang, W.; Jiang, J.-Z.; Mao, W. L.; Mao, H.-K. Long-range topological order in metallic glass. *Science (80-.).* **2011**, *332* (6036), 1404–1406 DOI: 10.1126/science.1200324.

(106) Frank, F. C. Supercooling of Liquids. *Proc. R. Soc. A Math. Phys. Eng. Sci.* **1952**, *215* (1120), 43–46 DOI: 10.1098/rspa.1952.0194.

(107) Bernal, J. D. Geometry of the Structure of Monatomic Liquids. *Nature* **1960**, *185* (4706), 68–70 DOI: 10.1038/185068a0.

(108) Gaskell, P. H. A new structural model for amorphous transition metal silicides, borides, phosphides and carbides. *J. Non. Cryst. Solids* **1979**, *32* (1-3), 207–224 DOI: 10.1016/0022-3093(79)90073-5.

(109) Gaskell, P. H. A new structural model for transition metal–metalloid glasses. *Nature* **1978**, *276* (5687), 484–485 DOI: 10.1038/276484a0.

(110) Gaskell, P. H. Similarities in amorphous and crystalline transition metal–metalloid alloy structures. *Nature* **1981**, *289* (5797), 474–476 DOI: 10.1038/289474a0.

(111) Reichert, H.; Klein, O.; Dosch, H.; Denk, M.; Honkimäki, V.; Lippmann, T.; Reiter, G. Observation of five-fold local symmetry in liquid lead. *Nature* **2000**, *408* (6814), 839–841 DOI: 10.1038/35048537.

(112) Spaepen, F. Five-fold symmetry in liquids. *Nature* **2000**, *408* (6814), 781–782 DOI: 10.1038/35048652.

(113) Schenk, T.; Holland-Moritz, D.; Simonet, V.; Bellissent, R.; Herlach, D. M. Icosahedral Short-Range Order in Deeply Undercooled Metallic Melts. *Phys.*

Rev. Lett. **2002**, *89* (7), 075507 DOI: 10.1103/PhysRevLett.89.075507.

(114) Kelton, K. F.; Lee, G. W.; Gangopadhyay, A. K.; Hyers, R. W.; Rathz, T. J.; Rogers, J. R.; Robinson, M. B.; Robinson, D. S. First X-Ray Scattering Studies on Electrostatically Levitated Metallic Liquids: Demonstrated Influence of Local Icosahedral Order on the Nucleation Barrier. *Phys. Rev. Lett.* **2003**, *90* (19), 195504 DOI: 10.1103/PhysRevLett.90.195504.

(115) Yue, G. Q.; Zhang, Y.; Sun, Y.; Shen, B.; Dong, F.; Wang, Z. Y.; Zhang, R. J.; Zheng, Y. X.; Kramer, M. J.; Wang, S. Y.; et al. Local structure order in $Pd_{78}Cu_6Si_{16}$ liquid. *Sci. Rep.* **2015**, *5*, 8277 DOI: 10.1038/srep08277.

(116) Cicco, A. Di; Iesari, F.; De Panfilis, S.; Celino, M.; Giusepponi, S.; Filipponi, A. Local fivefold symmetry in liquid and undercooled Ni probed by x-ray absorption spectroscopy and computer simulations. *Phys. Rev. B* **2014**, *89* (6), 060102 DOI: 10.1103/PhysRevB.89.060102.

(117) Georgarakis, K.; Hennet, L.; Evangelakis, G. A.; Antonowicz, J.; Bokas, G. B.; Honkimaki, V.; Bytchkov, A.; Chen, M. W.; Yavari, A. R. Probing the structure of a liquid metal during vitrification. *Acta Mater.* **2015**, *87*, 174–186 DOI: 10.1016/j.actamat.2015.01.005.

(118) Miracle, D. B.; Louzguine-Luzgin, D. V; Louzguina-Luzgina, L. V; Inoue, A. An assessment of binary metallic glasses: correlations between structure, glass forming ability and stability. *Int. Mater. Rev.* **2010**, *55* (4), 218–256 DOI: 10.1179/095066010X12646898728200.

(119) Hwang, J.; Melgarejo, Z. H.; Kalay, Y. E.; Kalay, I.; Kramer, M. J.; Stone, D. S.; Voyles, P. M. Nanoscale Structure and Structural Relaxation in $Zr_{50}Cu_{45}Al_5$ Bulk Metallic Glass. *Phys. Rev. Lett.* **2012**, *108* (19), 195505 DOI: 10.1103/PhysRevLett.108.195505.

(120) Park, E. S.; Kim, D. H. Phase separation and enhancement of plasticity in Cu-Zr-Al-Y bulk metallic glasses. *Acta Mater.* **2006**, *54* (10), 2597–2604 DOI: 10.1016/j.actamat.2005.12.020.

(121) Kim, K. B.; Das, J.; Baier, F.; Tang, M. B.; Wang, W. H.; Eckert, J. Heterogeneity of a $Cu_{47.5}Zr_{47.5}Al_5$ bulk metallic glass. *Appl. Phys. Lett.* **2006**, *88* (5), 051911 DOI: 10.1063/1.2171472.

(122) Bodapati, A.; Treacy, M. M. J.; Falk, M.; Kieffer, J.; Keblinski, P. Medium range order and the radial distribution function. *J. Non. Cryst. Solids* **2006**, *352* (2), 116–122 DOI: 10.1016/j.jnoncrysol.2005.11.028.

(123) Miracle, D. B. The density and packing fraction of binary metallic glasses. *Acta Mater.* **2013**, *61* (9), 3157–3171 DOI: 10.1016/j.actamat.2013.02.005.

(124) Aykol, M.; Mekhrabov, A. O.; Akdeniz, M. V. Nano-scale phase separation in amorphous Fe–B alloys: Atomic and cluster ordering. *Acta Mater.* **2009**, *57* (1), 171–181 DOI: 10.1016/j.actamat.2008.09.005.

(125) Salmon, P. S.; Martin, R. A.; Mason, P. E.; Cuello, G. J. Topological versus chemical ordering in network glasses at intermediate and extended length scales. *Nature* **2005**, *435* (7038), 75–78 DOI: 10.1038/nature03475.

(126) Elliott, S. R. The origin of the first sharp diffraction peak in the structure factor of covalent glasses and liquids. *J. Phys. Condens. Matter* **1992**, *4* (38), 7661–7678 DOI: 10.1088/0953-8984/4/38/003.

(127) Phillips, J. C. Topology of covalent non-crystalline solids I: Short-range order in chalcogenide alloys. *J. Non. Cryst. Solids* **1979**, *34* (2), 153–181 DOI: 10.1016/0022-3093(79)90033-4.

(128) Vateva, E.; Savova, E. New medium-range order features in Ge-Sb-S glasses. *J. Non. Cryst. Solids* **1995**, *192-193*, 145–148 DOI: 10.1016/0022-3093(95)00435-1.

(129) Kalay, Y. E.; Chumbley, L. S.; Kramer, M. J.; Anderson, I. E. Local structure in marginal glass forming Al-Sm alloy. *Intermetallics* **2010**, *18* (8), 1676–1682 DOI: 10.1016/j.intermet.2010.05.005.

(130) Mauro, N. a.; Blodgett, M.; Johnson, M. L.; Vogt, a. J.; Kelton, K. F. A

structural signature of liquid fragility. *Nat. Commun.* **2014**, *5*, 1–7 DOI: 10.1038/ncomms5616.

(131) Johnson, M. L.; Blodgett, M. E.; Lokshin, K. A.; Mauro, N. A.; Neuefeind, J.; Pueblo, C.; Quirinale, D. G.; Vogt, A. J.; Egami, T.; Goldman, A. I.; et al. Measurements of structural and chemical order in $Zr_{80}Pt_{20}$ and $Zr_{77}Rh_23$ liquids. *Phys. Rev. B* **2016**, *93* (5), 054203 DOI: 10.1103/PhysRevB.93.054203.

(132) Ovun, M.; Kramer, M. J.; Kalay, Y. E. Structural modeling of liquid and amorphous $Al_{91}Tb_9$ by Monte Carlo simulations. *J. Non. Cryst. Solids* **2014**, *405*, 27–32 DOI: 10.1016/j.jnoncrysol.2014.08.037.

(133) Li, M.; Wang, C. Z.; Hao, S. G.; Kramer, M. J.; Ho, K. M. Structural heterogeneity and medium-range order in Zr_xCu_{100-x} metallic glasses. *Phys. Rev. B* **2009**, *80* (18), 184201 DOI: 10.1103/PhysRevB.80.184201.

(134) Hou, Z. Y.; Liu, L. X.; Liu, R. S.; Tian, Z. A.; Wang, J. G. Short-range and medium-range order in rapidly quenched $Al_{50}Mg_{50}$ alloy. *J. Non. Cryst. Solids* **2011**, *357* (5), 1430–1436 DOI: 10.1016/j.jnoncrysol.2010.11.014.

(135) Pan, S.; Feng, S.; Qiao, J.; Dong, B.; Qin, J. The atomic structure of liquid Fe–C alloys. *J. Alloys Compd.* **2015**, *648*, 178–183 DOI: 10.1016/j.jallcom.2015.06.252.

(136) Miracle, D. B. A Structural Model For Metallic Glasses. *Nat. Mater.* **2004**, *3* (10), 697–702 DOI: 10.1038/nmat1219.

(137) Miracle, D. B. The efficient cluster packing model – An atomic structural model for metallic glasses. *Acta Mater.* **2006**, *54* (16), 4317–4336 DOI: 10.1016/j.actamat.2006.06.002.

(138) Miracle, D. B.; Laws, K.; Senkov, O. N.; Wilks, G. B. Partial coordination numbers in binary metallic glasses. *Metall. Mater. Trans. A Phys. Metall. Mater. Sci.* **2012**, *43* (8), 2649–2661 DOI: 10.1007/s11661-011-1002-7.

(139) Miracle, D. B.; Lord, E. A.; Ranganathan, S. Candidate Atomic Cluster

Configurations in Metallic Glass Structures. *Mater. Trans.* **2006**, *47* (7), 1737–1742 DOI: 10.2320/matertrans.47.1737.

(140) Senkov, O. N.; Miracle, D. B. Effect of the atomic size distribution on glass forming ability of amorphous metallic alloys. *Mater. Res. Bull.* **2001**, *36*, 2183–2198.

(141) Miracle, D. B.; Sanders, W. S.; Senkov, O. N. The influence of efficient atomic packing on the constitution of metallic glasses. *Philos. Mag.* **2003**, *83* (20), 2409–2428 DOI: 10.1080/1478643031000098828.

(142) Antonowicz, J.; Louzguine-Luzgin, D. V.; Yavari, A. R.; Georgarakis, K.; Stoica, M.; Vaughan, G.; Matsubara, E.; Inoue, A. Atomic structure of Zr–Cu–Al and Zr–Ni–Al amorphous alloys. *J. Alloys Compd.* **2009**, *471* (1-2), 70–73 DOI: 10.1016/j.jallcom.2008.03.092.

(143) Pusztai, L.; Svab, E. Modelling the structure of $Ni_{65}B_{35}$ metallic glass by reverse Monte Carlo simulation. *J. Phys. Condens. Matter* **1993**, *5* (47), 8815–8828 DOI: 10.1088/0953-8984/5/47/007.

(144) Schultz, L.; Lamparter, P.; Steeb, S. X-Ray and Neutron Diffraction of Amorphous Nickel-Zirconium-Alloys as Prepared in Different Ways. *Zeitschrift für Naturforsch. A* **1991**, *46* (6), 491–498 DOI: 10.1515/zna-1991-0604.

(145) Fan, C.; Liaw, P. K.; Wilson, T. W.; Choo, H.; Gao, Y. F.; Liu, C. T.; Proffen, T.; Richardson, J. W. Pair distribution function study and mechanical behavior of as-cast and structurally relaxed Zr-based bulk metallic glasses. *Appl. Phys. Lett.* **2006**, *89* (23), 231920 DOI: 10.1063/1.2402884.

(146) Takagi, T.; Ohkubo, T.; Hirotsu, Y.; Murty, B. S.; Hono, K.; Shindo, D. Local structure of amorphous $Zr_{70}Pd_{30}$ alloy studied by electron diffraction. *Appl. Phys. Lett.* **2001**, *79* (4), 485 DOI: 10.1063/1.1383055.

(147) Ohkubo, T.; Hirotsu, Y. Electron diffraction and high-resolution electron

microscopy study of an amorphous $Pd_{82}Si_{18}$ alloy with nanoscale phase separation. *Phys. Rev. B* **2003**, *67* (9), 094201 DOI: 10.1103/PhysRevB.67.094201.

(148) LI, G.; BORISENKO, K.; CHEN, Y.; NGUYENMANH, D.; MA, E.; COCKAYNE, D. Local structure variations in $Al_{89}La_6Ni_5$ metallic glass. *Acta Mater.* **2009**, *57* (3), 804–811 DOI: 10.1016/j.actamat.2008.10.036.

(149) Wu, N. C.; Yan, M.; Zuo, L.; Wang, J. Q. Correlation between medium-range order structure and glass-forming ability for Al-based metallic glasses. *Appl. Phys. Lett.* **2014**, *104* (25) DOI: 10.1063/1.4863404.

(150) Kalay, Y. E.; Yeager, C.; Chumbley, L. S.; Kramer, M. J.; Anderson, I. E. Initial crystallization in a nanostructured Al–Sm rare earth alloy. *J. Non. Cryst. Solids* **2010**, *356* (28-30), 1416–1424 DOI: 10.1016/j.jnoncrysol.2010.05.005.

(151) Perepezko, J. H.; Hebert, R. J.; Wu, R. I.; Wilde, G. Primary crystallization in amorphous Al-based alloys. *J. Non. Cryst. Solids* **2003**, *317* (1-2), 52–61 DOI: 10.1016/S0022-3093(02)01983-X.

(152) Sun, Y.; Zhang, F.; Ye, Z.; Fang, X.; Ding, Z.; Wang, C.-Z.; Mendelev, M. I.; Ott, R. T.; Kramer, M. J.; Ho, K. M. Crystalline “Genes” in Metallic Liquids. **2014**.

(153) Fang, X. W.; Wang, C. Z.; Yao, Y. X.; Ding, Z. J.; Ho, K. M. Signature of Al11Sm3 fragments in undercooled Al90Sm10 liquid from ab initio molecular dynamics simulations. *J. Phys. Condens. Matter* **2011**, *23* (23), 235104 DOI: 10.1088/0953-8984/23/23/235104.

(154) Sahu, K. K.; Mauro, N. a.; Longstreth-Spoor, L.; Saha, D.; Nussinov, Z.; Miller, M. K.; Kelton, K. F. Phase separation mediated devitrification of Al88Y7Fe5 glasses. *Acta Mater.* **2010**, *58* (12), 4199–4206 DOI: 10.1016/j.actamat.2010.04.011.

(155) Demirtaş, T. Nanocrystallization in Marginal Glass Forming Alloys, MS

Thesis, Middle East Technical University, 2013.

(156) Yıldırım, C.; Kutsal, M.; Ott, R. T.; Besser, M. F.; Kramer, M. J.; Kalay, Y. E. The Role of Amorphous Precursor in Phase Selection Hierarchy in Marginal Metallic Glasses. *Mater. Des.* **2016**, *Under Revi*.

(157) Evrard, G.; Pusztai, L. Reverse Monte Carlo modelling of the structure of disordered materials with RMC++ : a new implementation of the algorithm in C++. *J. Phys. Condens. Matter* **2005**, *17* (5), S1–S13 DOI: 10.1088/0953-8984/17/5/001.

(158) Chen, H. S.; Waseda, Y. Structure of glassy Zr-Cu and Nb-Ni alloys. *Phys. Status Solidi* **1979**, *51* (2), 593–599 DOI: 10.1002/pssa.2210510235.

(159) Bacewicz, R.; Antonowicz, J. XAFS study of amorphous Al-RE alloys. *Scr. Mater.* **2006**, *54* (6), 1187–1191 DOI: 10.1016/j.scriptamat.2005.11.033.

(160) Zalewski, W.; Antonowicz, J.; Bacewicz, R.; Latuch, J. Local atomic order in Al-based metallic glasses studied using XAFS method. *J. Alloys Compd.* **2009**, *468* (1-2), 40–46 DOI: 10.1016/j.jallcom.2008.01.037.

(161) Singh, S.; Ediger, M. D.; de Pablo, J. J. Ultrastable glasses from in silico vapour deposition. *Nat. Mater* **2013**, *12* (2), 139–144.

(162) Liu, Y. H.; Fujita, T.; Aji, D. P. B.; Matsuura, M.; Chen, M. W. Structural origins of Johari-Goldstein relaxation in a metallic glass. *Nat. Commun.* **2014**, *5* DOI: 10.1038/ncomms4238.

(163) Treacy, M. M. J.; Gibson, J. M.; Fan, L.; Paterson, D. J.; McNulty, I. Fluctuation microscopy: a probe of medium range order. *Reports Prog. Phys.* **2005**, *68* (12), 2899–2944 DOI: 10.1088/0034-4885/68/12/R06.

(164) Stratton, W. G.; Hamann, J.; Perepezko, J. H.; Voyles, P. M. Electron beam induced crystallization of amorphous Al-based alloys in the TEM. *Intermetallics* **2006**, *14* (8-9), 1061–1065 DOI: 10.1016/j.intermet.2006.01.025.

(165) Imhoff, S. D.; Ilavsky, J.; Zhang, F.; Jemian, P.; Evans, P. G.; Perepezko, J. H. Kinetic transition in the growth of Al nanocrystals in Al-Sm alloys. *J. Appl. Phys.* **2012**, *111* (6), 1–9 DOI: 10.1063/1.3697654.

(166) Demirtaş, T.; Kalay, Y. E. Kinetics of fcc-Al nanocrystallization in $Al_{90}Tb_{10}$ metallic glass. *J. Non. Cryst. Solids* **2013**, *378*, 71–78 DOI: 10.1016/j.jnoncrysol.2013.06.020.

(167) Jakse, N.; Pasturel, A. Local order and dynamic properties of liquid and undercooled Cu_xZr_{1-x} alloys by ab initio molecular dynamics. *Phys. Rev. B* **2008**, *78* (21), 214204 DOI: 10.1103/PhysRevB.78.214204.

(168) Ding, J.; Cheng, Y.-Q.; Ma, E. Full icosahedra dominate local order in Cu64Zr34 metallic glass and supercooled liquid. *Acta Mater.* **2014**, *69*, 343–354 DOI: 10.1016/j.actamat.2014.02.005.

(169) Egami, T. The atomic structure of aluminum based metallic glasses and universal criterion for glass formation. *J. Non. Cryst. Solids* **1996**, *205-207*, 575–582 DOI: 10.1016/S0022-3093(96)00277-3.

(170) Spowart, J. .; Miracle, D. .; Mullens, H. . The influence of solute distribution on the high nucleation density of Al crystals in amorphous aluminum alloys. *J. Non. Cryst. Solids* **2004**, *336* (3), 202–211 DOI: 10.1016/j.jnoncrysol.2004.02.011.

(171) Antonowicz, J.; Jezierska, E.; Kedzierski, M.; Yavari, A. R.; Greer, L.; Panine, P.; Sztucki, M. Early stages of phase separation and nanocrystallization in Al-rare earth metallic glasses studied using SAXS/WAXS and HRTEM methods. *Rev. Adv. Mater. Sci.* **2008**, *18* (5), 454–458.

(172) Shi, Y.; Falk, M. L. Structural transformation and localization during simulated nanoindentation of a noncrystalline metal film. *Appl. Phys. Lett.* **2005**, *86* (1), 1–4 DOI: 10.1063/1.1844593.

(173) Henao, J.; Concustell, A.; G.Cano, I.; Dosta, S.; Cinca, N.; Guilemany, J. M.;

Suhonen, T. Novel Al-based metallic glass coatings by Cold Gas Spray. *Mater. Des.* **2016**, *94*, 253–261 DOI: 10.1016/j.matdes.2016.01.040.

(174) Yang, B. J.; Yao, J. H.; Zhang, J.; Yang, H. W.; Wang, J. Q.; Ma, E. Al-rich bulk metallic glasses with plasticity and ultrahigh specific strength. *Scr. Mater.* **2009**, *61* (4), 423–426 DOI: 10.1016/j.scriptamat.2009.04.035.

(175) He, Y.; Shiflet, G. .; Poon, S. . Synthesis and properties of aluminum-based metallic glasses containing rare earths. *J. Alloys Compd.* **1994**, *207-208*, 349–354 DOI: 10.1016/0925-8388(94)90238-0.

(176) Inoue, A.; Kimura, H. Fabrications and mechanical properties of bulk amorphous, nanocrystalline, nanoquasicrystalline alloys in aluminum-based system.*J. Light Met.* **2001**,*1* (1), 31–41 DOI: 10.1016/S1471-5317(00)00004-3.

(177) Kim, T.-S.; Lee, J.-K.; Kim, H.-J.; Bae, J.-C. Consolidation of $Cu_{54}Ni_6Zr_{22}Ti_{18}$ bulk amorphous alloy powders. *Mater. Sci. Eng. A* **2005**, *402* (1-2), 228–233 DOI: 10.1016/j.msea.2005.04.044.

(178) Lee, J. K.; Kim, H. J.; Kim, T. S.; Kim, Y. C.; Bae, J. C. Consolidation behavior of Cu- and Ni-based bulk metallic glass composites. *J. Alloys Compd.* **2007**, *434-435*, 336–339 DOI: 10.1016/j.jallcom.2006.08.304.

(179) Krasnowski, M.; Kulik, T. Nanocrystalline or amorphous matrix $Al_{60}Fe_{15}Ti_{15}(Co/Mg/Zr)_5$-5%B composites produced by consolidation of mechanically alloyed powders - Lightweight materials with high hardness. *Intermetallics* **2012**, *28*, 120–127 DOI: 10.1016/j.intermet.2012.04.011.

(180) Wei, X.; Han, F.; Wang, X.; Wang, X.; Wen, C. Fabrication of Al-based bulk metallic glass by mechanical alloying and vacuum hot consolidation. *J. Alloys Compd.* **2010**, *501* (1), 164–167 DOI: 10.1016/j.jallcom.2010.04.069.

(181) Choi, P. P.; Kim, J. S.; Nguyen, O. T. H.; Kwon, D. H.; Kwon, Y. S.; Kim, J. C. Al-La-Ni-Fe bulk metallic glasses produced by mechanical alloying and spark-plasma sintering. *Mater. Sci. Eng. A* **2007**, *448-451*, 1119–1122 DOI:

10.1016/j.msea.2006.02.264.

(182) Krasnowski, M.; Kulik, T. Crystallisation of Amorphous $Al_{60}Fe_{20}Ti_{15}Ni_5$ Alloy Produced by Mechanical Alloying. *Solid State Phenomena*. 2010, pp 243–246.

(183) Gu, X. .; Ye, F.; Zhou, F.; Lu, K. Pressure effect on crystallization of mechanically alloyed amorphous $Al_{85}Fe_{15}$ alloy. *Materials Science and Engineering: A*. 2000, pp 61–65.

(184) Krasnowski, M.; Kulik, T. Nanocrystalline and amorphous Al-Fe alloys containing 60-85% of Al synthesised by mechanical alloying and phase transformations induced by heating of milling products. *Mater. Chem. Phys.* **2009**, *116* (2-3), 631–637 DOI: 10.1016/j.matchemphys.2009.05.003.

(185) Wilson, T. W.; Choo, H.; Porter, W. D.; Speakman, S. A.; Fan, C.; Liaw, P. K. Amorphization and crystallization processes of the ball-milled Al-Y-Fe-TM alloys (TM = Ni, Co, Cu, and Fe). *J. Non. Cryst. Solids* **2006**, *352* (38-39), 4024–4029 DOI: 10.1016/j.jnoncrysol.2006.07.004.

(186) Dutkiewicz, J.; Lityńska, L.; Maziarz, W.; Kočiško, R.; Molnarová, M.; Kováčová, a. HRTEM and TEM studies of amorphous structures in ZrNiTiCu base alloys obtained by rapid solidification or ball milling. *Micron* **2009**, *40* (1), 1–5 DOI: 10.1016/j.micron.2008.03.009.

(187) Dieter, G.; Bacon, D. *Mechanical Metallurgy. SI Metric Edition*; 1988.

(188) Hertzberg, R. W. Deformation and Fracture Mechanics of Engineering Materials. 1996, p 810.

(189) Gloriant, T.; Danoix, F.; Lefebvre, W.; Greer, a. L. Nanocrystallized $Al_{92}Sm_8$ Amorphous Alloy Investigated by High-Resolution Microscopy and 3D Atom-Probe Analysis. *Adv. Eng. Mater.* **2007**, *9* (3), 151–155 DOI: 10.1002/adem.200600222.

(190) Miracle, D. B.; Senkov, O. N. A geometric model for atomic configurations in amorphous Al alloys. *J. Non. Cryst. Solids* **2003**, *319* (1-2), 174–191 DOI:

10.1016/S0022-3093(02)01917-8.

(191) Jiang, W. H.; Pinkerton, F. E.; Atzmon, M. Deformation-induced nanocrystallization in an Al-based amorphous alloy at a subambient temperature. *Scr. Mater.* **2003**, *48* (8), 1195–1200 DOI: 10.1016/S1359-6462(02)00568-7.

(192) Gao, M. C.; Hackenberg, R. E.; Shiflet, G. J. Deformation-Induced Nanocrystal Precipitation in Al-Base Metallic Glasses. *Materials Transactions*. 2001.

(193) Imhoff, S. D.; Ilavsky, J.; Zhang, F.; Jemian, P.; Evans, P. G.; Perepezko, J. H. Kinetic transition in the growth of Al nanocrystals in Al-Sm alloys. *J. Appl. Phys.* **2012**, *111* (6), 063525 DOI: 10.1063/1.3697654.

(194) Wilde, G.; Boucharat, N.; Hebert, R. J.; Rösner, H.; Tong, W. S.; Perepezko, J. H. Nanocrystallization in Al-rich Metallic Glasses. *Adv. Eng. Mater.* **2003**, *5* (3), 125–130 DOI: 10.1002/adem.200390019.

(195) Gao, M. C.; Guo, F.; Poon, S. J.; Shiflet, G. J. Development of fcc-Al nanocrystals in Al-Ni-Gd metallic glasses during continuous heating DSC scan. *Mater. Sci. Eng. A* **2008**, *485* (1-2), 532–543 DOI: 10.1016/j.msea.2007.08.009.

(196) Perepezko, J. H.; Imhoff, S. D.; Hebert, R. J. Nanostructure development during devitrification and deformation. *J. Alloys Compd.* **2010**, *495* (2), 360–364 DOI: 10.1016/j.jallcom.2009.10.051.

(197) Kissinger, H. E. Reaction Kinetics in Differential Thermal Analysis. *Anal. Chem.* **1957**, *29* (11), 1702–1706 DOI: 10.1021/ac60131a045.

(198) Ozawa, T. A New Method of Analyzing Thermogravimetric Data. *Bull. Chem. Soc. Jpn.* **1965**, *38* (11), 1881–1886 DOI: 10.1246/bcsj.38.1881.

(199) Li, X. P.; Yan, M.; Yang, B. J.; Wang, J. Q.; Schaffer, G. B.; Qian, M. Crystallization behaviour and thermal stability of two aluminium-based metallic glass powder materials. *Mater. Sci. Eng. A* **2011**, *530*, 432–439 DOI: 10.1016/j.msea.2011.09.107.

(200) Kim, D. H.; Kim, W. T.; Park, E. S.; Mattern, N.; Eckert, J. Phase separation in metallic glasses. *Prog. Mater. Sci.* **2013**, *58* (8), 1103–1172 DOI: 10.1016/j.pmatsci.2013.04.002.

(201) Porter, D. A.; Easterling, K. E. *Phase Transformations in Metals and Alloys*, Third Edit.; 2014.

(202) ASTM International. ASTM E9-09 - Standard Test Methods of Compression Testing of Metallic Materials at Room Temperature. **2009**, 1–9 DOI: 10.1520/E0009.

(203) Schuh, C.; Hufnagel, T.; Ramamurty, U. Mechanical behavior of amorphous alloys. *Acta Mater.* **2007**, *55* (12), 4067–4109 DOI: 10.1016/j.actamat.2007.01.052.

(204) Greer, a. L.; Cheng, Y. Q.; Ma, E. Shear bands in metallic glasses. *Mater. Sci. Eng. R Reports* **2013**, *74* (4), 71–132 DOI: 10.1016/j.mser.2013.04.001.

(205) Lee, J. C.; Kim, Y. C.; Ahn, J. P.; Kim, H. S. Enhanced plasticity in a bulk amorphous matrix composite: Macroscopic and microscopic viewpoint studies. *Acta Mater.* **2005**, *53* (1), 129–139 DOI: 10.1016/j.actamat.2004.09.010.

(206) Xu, Y.-K.; Ma, H.; Xu, J.; Ma, E. Mg-based bulk metallic glass composites with plasticity and gigapascal strength. *Acta Mater.* **2005**, *53* (6), 1857–1866 DOI: 10.1016/j.actamat.2004.12.036.

(207) Imhoff, S. D.; Ilavsky, J.; Zhang, F.; Jemian, P.; Evans, P. G.; Perepezko, J. H. Kinetic transition in the growth of Al nanocrystals in Al-Sm alloys. *J. Appl. Phys.* **2012**, *111* (6), 063525 DOI: 10.1063/1.3697654.

(208) Hebert, R. J.; Perepezko, J. H.; Rösner, H.; Wilde, G. Dislocation formation during deformation-induced synthesis of nanocrystals in amorphous and partially crystalline amorphous $Al_{88}Y_7Fe_5$ alloy. *Scr. Mater.* **2006**, *54* (1), 25–29 DOI: 10.1016/j.scriptamat.2005.09.013.

(209) Schuh, C. A.; Nieh, T. G. A nanoindentation study of serrated flow in bulk

metallic glasses. *Acta Mater.* **2003**, *51* (1), 87–99 DOI: 10.1016/S1359-6454(02)00303-8.

(210) Davis, J. R. *Aluminum and Aluminum Alloys*; ASM International, 1993.

(211) Cullity, B. D.; Stock, S. R. *Elements of X-ray diffraction, 3rd edition*; 2001.

(212) DeLanda, M. *Intensive Science and Virtual Philosophy*; Bloomsbury Academic: New York, 2002.